Linking the Continuum and Molecular Scales of Adsorption Modeling for Non-Ionic Small Molecules and Homopolymers

by

Kyle Jeffrey Huston

A dissertation submitted in partial fulfillment
of the requirements for the degree of
Doctor of Philosophy
(Chemical Engineering)
in the University of Michigan
2018

Doctoral Committee:
Professor Ronald G. Larson, Chair
Professor Michael J. Solomon
Associate Professor Angela Violi
Professor Robert M. Ziff

Kyle J. Huston

khuston@umich.edu

ORCID iD: 0000-0003-1737-0027

© Kyle Jeffrey Huston 2018

DEDICATION

To Ana and all my family

ACKNOWLEDGEMENTS

I am indebted to my advisor, Professor Ron Larson, for his guidance over the years, and I am fortunate to have worked under his supervision. Ron is incisive, hard-working, generous with his time, and very kind. I left every meeting invigorated by our discussion. Ron also encouraged attendance at conferences and helped fund them directly or with grant applications.

Thanks also to the committee for the feedback, which has been helpful in preparing the dissertation both before and after the defense. Many thanks to my colleagues and friends in the Larson and Glotzer groups, especially Wenjun Huang and Aly Salehi who I enjoyed many chats with over the years, both about research and trivia. Thank you to Ashley Kiemenn for the research assistance and for tolerating many abortive research directions. Thank you to Professor Eniola-Adefeso for her guidance and assistance. I am also grateful to Bruce Murch and Russell DeVane at Procter & Gamble for the opportunity to intern with the Modeling & Simulation group in the summer of 2015.

I want to thank my family, especially Mom & Dad Huston and Mom & Dad Reynolds for always being there for me. Your words of wisdom and love gave me perspective and comfort when I needed it. Finally, I could not have completed this work without the companionship and support of my girlfriend Ana Rioja, who spent countless hours at my side. Thank you.

TABLE OF CONTENTS

CHAPTER 4

CHAPTER 5

LIST OF APPENDICES

LIST OF FIGURES

LIST OF ABBREVIATIONS

(Symbols, Numerical Order, Alphabetical Order)

°C	Celsius
CG	Coarse-grained
FFS	Forward flux sampling
GAE	Gibbs adsorption equation
MD	Molecular dynamics
NMB	Nikas-Mulqueen-Blankschtein
PEG	Poly(ethylene glycol)
PEO	Poly(ethylene oxide)
PMFs	Potentials of mean force
SPEs	Sorbitan poly(ethoxylates)
WHAM	Weighted histogram analysis method

ABSTRACT

Computational tensiometry and other quantitative adsorption predictions for small molecules and polymers are possible in the foreseeable future, but first, the application of the techniques to surfactant adsorption must be developed, and basic research is needed to identify the set of minimally required features of the molecular model that permits quantitative prediction. We take up the first challenge and apply three methods to three adsorption problems.

In the first approach, we simulate poly(ethylene oxide) (PEO) oligomers and a model Tween 80 (polyoxyethylene sorbitan monooleate) molecule at the water/alkane interface. We use the weighted histogram analysis method (WHAM) to calculate interfacial potentials of mean force (PMFs) for PEG and Tween 80 using the atomistic GROMOS $53a6_{OXY+D}$ and two coarse-grained (CG) MARTINI force fields. Because the force fields have not yet been validated for PEO adsorption to hydrophobic interfaces, we calculate PMFs for alcohol ethoxylates $C_{12}E_2$ and $C_{12}E_8$ and find agreement for the atomistic forcefield with reported semiempirical results, whereas for both CG force fields, PEO adsorbs too weakly to the hydrophobic interface. With the newly validated atomistic force field, we bracket the dilute adsorption free energy for a model Tween 80 molecule at the clean water/squalane interface. We also calculate the pressure–area isotherm and—with molecular thermodynamic theory and a simple transport model—demonstrate the transition from irreversible to reversible adsorption with increasing surface coverage, consistent with past experimental reporting.

In the second approach, we sought to explain experiments that show relaxation of oil/water interfacial tension by adsorption of alkyl ethoxylate surfactants from water is delayed relative to diffusion-controlled adsorption. We examine possible causes of this delay. We argue that a theory implicating transient depletion near an adsorbing interface for suppressing interfacial relaxation is invalid. We find that re-dissolution of the surfactant in the oil droplet cannot explain the apparent interfacial resistance at short times. We also perform WHAM with molecular dynamics simulation and do not find any evidence of an energy barrier or low-diffusivity zone near the interface. Nor do we find evidence from simulation that pre-micellar aggregation slows diffusion enough to cause the observed resistance to interfacial adsorption. We are therefore unable to pinpoint the cause of the resistance, but we suggest that "dead time" associated with the experimental method could be responsible – specifically local depletion of surfactant by the ejected droplet when creating the fresh oil/water interface.

In the third approach, we compute desorption rates for isolated polymers stuck to a solid wall with forward flux sampling (FFS). We interpret computed rates on the basis of a conjecture that a dimensionless desorption time scales with the equilibrium ratio of adsorbed surface amount to bulk concentration. We find that the dimensionless desorption time approaches the expected exponential scaling with the degree of polymerization multiplied by the mean field interaction between the monomer and the wall. However, we also find this strong adsorption scaling only becomes accurate for polymers which adsorb irreversibly on realistic timescales. We also find that excluded volume interactions and bending angle potentials shrink the desorption time and weaken the scaling of desorption time with N. For sufficiently weakly-adsorbing chains, the dimensionless desorption time becomes independent of N, suggesting a diffusion-controlled process overtakes the detachment process in importance.

CHAPTER 1

Introduction

Continuum-scale and molecular-scale modeling of physisorption have been undertaken for over a century. Irving Langmuir described interfacial monolayers of oriented amphiphilic molecules and developed an adsorption equation with chemical group contributions in 1917. Today, computational prediction of physisorption with molecular simulation is an emerging technique, but quantitative accuracy remains a problem. Study of physisorption can benefit from myriad techniques and theories that have been developed to calculate molecular flows and distributions at and near equilibrium. In this work, we take three approaches to three physisorption problems. First, we demonstrate that, in principle, a free energy calculation paired with computational tensiometry can predict the equilibrium interfacial adsorption of surfactant. Second, we show how to predict interfacial migration of small surfactant molecules at an interface using Markovian diffusive dynamics on the position of a surfactant molecule. Third, we predict rates of desorption for neutral homopolymers, which have very non-Markovian dynamics in terms of their center-of-mass position. Prediction of flows and distributions of adsorbing molecules can be used to parameterize mesoscale and continuum models to predict physical phenomena in rheology, drug stability, oil dispersal, and more. Having the complete molecular picture of macro phenomena can also inspire creative ways to manipulate the phenomena into new applications that are productive and pleasing.

1.1 Early modern theory

We recount key developments in thermodynamics that we draw upon for this work. Developments in thermodynamics and molecular theory came quickly starting in the mid-to-late 1800s. The most prominent theoretical advancements were due largely to Rudolf Clausius, James Clerk Maxell, Ludwig Boltzmann, and Josiah Willard Gibbs.[1] Between 1875 and 1878, Gibbs published *On the Equilibrium of Heterogeneous Substances*.[2] Starting on page 380 of the May 1877 issue, Gibbs presents his theory of capillarity and its principal equation, today known as the Gibbs adsorption equation (GAE), which relates changes in equilibrium interfacial tension to changes in the chemical potential of components that occupy the interface with some superficial density. Clayton Radke recently reviewed the GAE and presented it as[3]

$$-d\gamma = s_E^{\gamma} dT + \sum_{i=2}^{c} \Gamma_{iE} d\mu_i$$

where s_E^{γ} is the Gibbs-invariant excess interfacial entropy, Γ_{iE} is the Gibbs-invariant excess interfacial concentration of component i, and γ is the interfacial tension. Γ_{iE} is defined in terms of excess interfacial concentration Γ_{ij} of component i calculated for a Gibbs dividing surface j. The subtleties of this calculation are discussed elsewhere.[3] Briefly, for the purpose of this work, $\Gamma = \Gamma_{iE} \cong \Gamma_{ij}$, and Γ is the surface density of adsorbed species i in molecules per unit area obtained by integrating the excess volumetric concentration $c(z) - c_{\text{bulk}}(z)$ along the interface normal between bounds that continue far enough from the interface on either side to reach homogeneous solution. $c_{\text{bulk}}(z)$ is a step function which switches from the equilibrium bulk concentration of one phase to that of the other phase when passing the Gibbs dividing surface. This Gibbs adsorption equation is the basis for relating the chemical potential of each component μ_i with the interfacial tension γ in molecular thermodynamic theories.

Famously, in the late 1700s, Benjamin Franklin helped draw the attention of natural philosophers to adsorption when he became aware of the spreading of oil on the surface of water, used by sailors and divers to calm waves for millennia.[4] Throughout the 1800s, many experimenters focused their attention on surfaces.[5] Experiments were carried out that suggested that surfaces were sites of heightened reactivity for gas-phase reactions, though there was a dissenting view that instead the surfaces merely were sites of elevated concentration due to condensation which led to increased rats through the law of mass action.[6] Lord Rayleigh and Agnes Pockels carried out the first tensiometry of surfactant films on the surface of water while varying the area available to the films.[7–9] They found that surface tension was independent of the surface area as area decreased, until a point. After that point, further reductions in area rapidly decreased the surface tension. Rayleigh concluded that the oil molecules behaved as a gas until a dense monolayer was formed, at which point the surface tension rapidly decreased as the crowded adsorbed molecules mounted each other until a bilayer had formed.[8]

Irving Langmuir contributed a landmark review in 1917.[8] Known for his vivid articulation of the molecular kinetics underlying light bulbs, vacuum tubes, and other devices at General Electric,[10] Langmuir described the orientation and spreading of amphiphiles, particularly oleic acid, at the surface of water.[8] He also compared Szyszowski's empirical equation

$$\frac{\gamma}{\gamma_0} = 1 - B \log_{10}\left(\frac{c}{A} + 1\right)$$

with the Gibbs adsorption equation (Eqn. 1.1) under constant temperature ($dT = 0$) to obtain his famed equation, known as the Langmuir isotherm,

$$\mathit{\Gamma} = \mathit{\Gamma}_\infty \frac{c}{c + A}$$

where the maximum adsorbed amount $\mathit{\Gamma}_\infty = \frac{B\gamma_0}{\ln(10)\, RT}$ in terms of Szyzowski's parameters. Furthermore, Langmuir showed that in the dilute limit, the surface pressure $\mathit{\Pi} = \gamma_0 - \gamma$ behaved as a 2D ideal gas according to $\mathit{\Pi}^{\mathrm{id}} A = nRT$ where n is number of moles adsorbed to the surface, and A is the surface area. He also introduced the first molecular thermodynamic theory for physisorption of homologous series with an equation:

$$\frac{\mathit{\Gamma}}{c} = K e^{\lambda/RT}$$

where λ is the decrease in energy which occurs upon adsorption, and λ increases linearly with the number of contributing groups. Langmuir demonstrated this for homologous series with increasing numbers of -CH_2- groups in particular. It was since shown that the Langmuir isotherm arose by dynamic equilibrium of an adsorption rate and desorption rate which depend on the adsorbed amount $\mathit{\Gamma}$. In general, this is expressed as,

$$\frac{\partial \mathit{\Gamma}}{\partial t} = k_{\mathrm{ads}}(\mathit{\Gamma})c - k_{\mathrm{des}}(\mathit{\Gamma})\mathit{\Gamma}$$

and in particular for the Langmuir isotherm, $k_{\mathrm{ads}} = \alpha\left(1 - \frac{\mathit{\Gamma}}{\mathit{\Gamma}_\infty}\right)$ and $k_{\mathrm{des}} = \frac{\beta}{\mathit{\Gamma}_\infty}$ leads to the Langmuir isotherm such that $A = \frac{\beta}{\alpha}$ at equilibrium.

1.2 More developments pre-molecular simulation

Langmuir's review represented significant advances in the theory of physisorption. A few years later, Alexander Frumkin introduced an adsorption isotherm which is also still used in its original form and in a generalized form today. The following decades saw rapid advances in chemical reaction kinetics, contributed to and reviewed by Hinshelwood.[6] Around the same time, Onsager[11] and Kirkwood[12] developed the *potential of mean force* concept, at least in English – Onsager dates the idea back to Einstein[13] and Smoluchowski.[14] By omitting certain parameters from the phase integral for a thermodynamic ensemble, they obtained the marginal probability distribution over the omitted parameters. The omission of x from the phase integral can be represented by an ensemble average of the Dirac delta which is 1 when the reduced coordinate $X - x$ and 0 everywhere else:

$$\rho_X(x)dx = \langle \delta(X - x) \rangle = \frac{Z_X(x)}{Z}$$

We can introduce the free energy profile $F_X(x)$ which by definition is related to $\rho_X(x)$ by,

$$F_X(x) = -k_B T \ln \rho_X(x) + \text{Const.}$$

Differentiating with respect to x leads us to

$$\frac{\partial F_X(x)}{\partial x} = -k_B T \frac{1}{Z_X(x)} \frac{\partial Z_X(x)}{\partial x}$$

And assuming we have defined X so that it is orthogonal to the remaining degrees of freedom, i.e. $\{q_i\}_{3N-1} \perp X$, we have,

$$\frac{\partial Z_X(x)}{\partial x} = \int_{\{q_i\}_{3N-1} \perp X} \left[-\frac{1}{k_B T} \frac{\partial U}{\partial x} \right] e^{-U/k_B T} \, d\{q_i\}_{\{q_i\}_{3N-1} \perp X}$$

This leads to a simple result:

$$-\frac{\partial F_X(x)}{\partial x} = \langle -\partial U / \partial x \rangle$$

The ensemble-averaged gradient of potential energy is the mean force on x. In this case, the free energy F_X equals the potential of mean force because we defined X so that the remaining degrees of freedom were orthogonal, and we could bring $\frac{\partial}{\partial x}$ into the integral. Conceptually, the integral is the summation of differential phase elements, where each differential phase element is quantified by the product of the integrand $\left[-\frac{1}{k_B T}\frac{\partial U}{\partial x}\right]$ with the differential phase element's volume. The integrated phase elements all satisfy $X(\{q_i\}_{3N-1}) = x$. If the volume of every phase element is constant with respect to changes in x, then the derivative of each phase element passes to the integrand. If we represent the general potential of mean force with $w_X(x)$, then we have:

$$-\langle \nabla_x U_i \rangle = -\nabla_x w_X(x) \;\;\Leftrightarrow\;\; -\nabla_x F_X(x) = k_B T \nabla_x \ln c(x)$$

where the double-headed arrow ⇔ represents an equality that holds, for example, when x is a linear function of Cartesian atomic coordinates, such as the center of mass of a molecule. The *potential of mean force* and *free energy profile* are now widespread concepts in molecular simulation and molecular kinetics. [15]

The next landmark for us comes from Ward and Tordai.[16] Ward and Tordai (1946) published the first analytical theory for adsorption of surfactants to a surface that didn't assume surfactants were permanently fixed to the interface. It included back-diffusion whereby surfactant that had adsorbed could redissolve into solution and diffuse back into the bulk. Many previous researchers, including Langmuir, when seeking to model dynamic adsorption and/or tensiometry, had assumed that adsorbed surfactant would not desorb, which gave accurate results only at very short times.[16] The Ward-Tordai problem can be stated with a governing equation, initial condition, and boundary condition on a planar surface contacting a semi-infinite slab of fluid.

Governing equation	$\frac{\partial c}{\partial t} = D\frac{\partial^2 c}{\partial x^2}$
Initial condition	$c(x, t = 0) = c_s(t)$
Boundary condition	$\frac{\partial \Gamma}{\partial t} = \left.\frac{\partial c}{\partial x}\right\|_{x=0}$

The problem setup was surely understood by earlier researchers, but Ward and Tordai were the first to compute $\Gamma(t)$ without making further simplifying assumptions. Their namesake equation follows:

$$\Gamma(t) = 2\left(\frac{D}{\pi}\right)^{1/2}\left[c_0\sqrt{t} - \int_0^{\sqrt{t}} c_s(t-\tau)\, d\sqrt{\tau}\right]$$

Perhaps due to the convolution integral, Ward and Tordai's equation proved challenging enough to use, both before and after the proliferation of computers, that many researchers instead used short-time asymptotic solutions which have since been shown to be unreliable in a wide range of conditions.[17] The Ward-Tordai problem can also be generalized to more than one Cartesian dimension, and decades later, researchers published extensions to the Ward-Tordai analysis. In 1978, Reinhard Miller and George Kretzschmar proposed a variant of the Ward-Tordai method to account for mixed diffusion-kinetic controlled adsorption, for which an activation barrier to adsorption needs to be crossed. And in 1982, Karol Mysels extended the Ward-Tordai equation to deal with spherical interfaces and diffusion boundary layers generated by convection.[18]

At the same time as Ward and Tordai published their equation, the first electronic computer, the ENIAC, was developed and deployed, and one of the first uses by John von Neumann, Stan Ulam, and others was Monte Carlo calculations to model neutron diffusion.[19] Nicholas Metropolis, the Rosenbluths, and the Tellers applied the Monte Carlo method to calculate equations of state for hard particles and Lennard-Jones particles,[20] and the Rosenbluths carried out the first Monte Carlo study of polymer configurations in 1955.[21] The first molecular dynamics computations with an electronic computer were carried out by Alder and Wainwright in 1957, though it would be decades before classical mechanical simulation of surfactants with atomistic detail was carried out.[22]

Although we focus on adsorption of nonionic small molecules and polymers in this work, it is worth mentioning that the first modern thermodynamic theory of ionic surfactant adsorption was published by J.T. Davies in 1958. It accounts for the Gouy-Chapman double layer that formed adjacent to the charged surfactant-laden interface.[23] Although in this work Davies erroneously stated that the adsorption rate would be unaffected by the potential barrier, the equilibrium adsorption isotherm is sound. In 1994, MacLeod and Radke solved the Ward-Tordai problem for an ionic surfactant with and without the presence of background electrolyte, using the Nernst-Planck and Poisson equations with a Frumkin isotherm boundary condition.[24]

1.3 More sophisticated molecular thermodynamic theories and molecular simulation of surfactant

A sizeable portion of the literature on molecular thermodynamic models of surfactant have come from the Blankschtein group. The approach is reminiscent of Irving Langmuir's group contributions to the adsorption energy from 1917, but it is more sophisticated and extensive, and it accounts for micellization. Neglecting micellization and assuming an ideal solution, the interfacial equilibrium relation for the adsorption coefficient h, where h is the ratio of adsorbed surface density Γ to equilibrium dissolved concentration c_s,can be written as the following.[25]

$$h = h_0 \exp\left[-\frac{1}{k_B T}\int_{\Gamma=0}^{\Gamma} \frac{1}{\Gamma}\frac{d}{d\Gamma}\left(\Pi(\Gamma) - \Pi^{id}(\Gamma)\right) d\Gamma\right]$$

In the dilute limit, the adsorption coefficient h becomes $h_0 = \frac{1}{ac_T}\exp\left[-\frac{\Delta\mu^o}{k_B T}\right]$, where ac_T is an area per molecule multiplied by the total molar concentration. In fact, the choice of ac_T is arbitrary, because it serves simply to give h_0 the correct physical dimension of length. Any scaling of this reference length can be compensated by shifting the value of $\Delta\mu^{o}$. The quantity $\Delta\mu^{o}$ is defined as the difference of two reference chemical potentials.

$$\Delta\mu^{o} = \mu^{\sigma,0} - \mu^{b,0}$$

where the reference chemical potentials fit into expressions of the chemical potential in terms of surface quantities,

$$\mu^{\sigma} = \mu^{\sigma,0} + k_B T \ln(\Gamma a) + \int_{\Gamma=0}^{\Gamma} \frac{1}{\Gamma}\frac{d}{d\Gamma}\left(\Pi(\Gamma) - \Pi^{id}(\Gamma)\right) d\Gamma$$

and bulk quantities (assuming ideal solution).

$$\mu^{b} = \mu^{b,0} + k_B T \ln c_S / c_T$$

Blankschtein and others have applied such models with more sophisticated treatment of micellization and analytical surface equations of state $\Pi(\Gamma)$ to fit equilibrium adsorption data. In Chapter 3, we apply a form of this model as an interfacial equilibrium condition to study irreversibly adsorbed surfactant in the presence of a convection-driven boundary layer.

Beginning with Karplus and others from the mid-1970s onward, biomolecular simulation has grown into a vast effort to parameterize molecular potentials (force fields) for computer simulation. Many of today's most widely used force fields were motivated by the study of protein folding and catalysis, lipid bilayers, and other biomolecular phenomena. These force fields include CHARMM,[26] Gromos,[27] Amber,[28] and to a lesser extent OPLS.[29–31] Such force fields are optimized for physiological temperature and pressure. As such, they are also well-suited for simulation of non-biomolecular systems at ambient conditions. In this work, we validate and utilize the Gromos 53a6$_{\mathrm{OXY+D}}$ force field in particular.[32]

1.4 Background to three problems

With these developments in view, there was a clear opportunity to attempt quantitative prediction of physisorption using the modern molecular potentials that have been refined for biomolecular simulation. However, methods needed to be developed and demonstrated first. We have taken three general approaches to investigating three problems with molecular simulation. In the first problem – irreversible adsorption in a continuous-flow microtensiometer – we calculate and analyze the equilibrium interfacial distribution of surfactant. In the second problem – an apparent kinetic barrier to adsorption in a pendant drop tensiometer – we pair the equilibrium interfacial distribution and diffusivity with the diffusive dynamics models pioneered by Smoluchowski. Finally, in the third problem – desopriton rate of homopolymers from solid surface into dilute solution – we are prevented from using Markovian diffusive dynamics due to the significant memory effects of the polymer, due to slow configurational relaxation. In this case, we use forward flux sampling, which permits calculation of the rate of rare events without the Markovian assumption required for the diffusive model.

1.4.1 Irreversible adsorption in a continuous-flow microtensiometer

Matthew Reichert and Lynn Walker measured dynamic interfacial tension between squalane, a lightly-branched alkane, and aqueous surfactant solution with a microtensiometer in the presence. The surfactant they studied was Tween 80®, which is a polydisperse mixture of polyethoxylated sorbitan oleate. The polyethoxylated sorbitan makes up the hydrophilic group, and the oleate tail(s) comprise the hydrophobic group(s). They found that Tween 80® adsorbed irreversibly to the liquid-liquid interface under flow, and they proposed that some kind of rearrangement and entanglement of the ethoxylated headgroups was responsible. The irreversible adsorption was mysterious, because continuous-flow tensiometry with desorption was a relatively new and rare experiment. One of the most comprehensive review articles on the subject of adsorption dynamics skips over the subject of irreversible adsorption.[33] Thus, we deemed the phenomenon worthy of investigation.

We investigated with simple continuum transport modeling and free energy calculation of the interfacial equilibrium between adsorbed Tween 80® and free Tween 80® in solution. The broad polydispersity of Tween 80® is difficult to represent in any modestly-sized simulation box, so we simulated the stoichiometric-average molecule and used thermodynamic insight from the results to predict how variant structures would behave in the commercial mixture.

1.4.2 Apparent kinetic barrier to adsorption in a pendant drop tensiometer

We next investigated a dynamic tensiometry study on alkyl ethlxyoates in the C_iE_8 series at a silicone oil/water interface. The authors reported a kinetic barrier to adsorption in excess of the diffusive barrier. Such barriers are modeled with an adsorption rate equation in the form of Equation 5. After having simulated Tween 80® at an oil/water interface, including at high surface coverage, the presence of an energy barrier to adsorption of C_iE_8 surfactants seemed dubious. While one would expect a steric barrier to adsorption of an additional surfactant at an already crowded interface, preliminary simulations of such a process seemed to refute the presence of an energy barrier. To investigate further, we utilized free energy calculations again, this time with the aim of incorporating the results in a Smoluchowski diffusion equation to represent the surfactant diffusion dynamics in a mean field.

1.4.3 Desorption rate of homopolymers from solid surface into dilute solution

Finally, we were impressed by the work of Skaug et al., in which they analyzed trajectories from total internal reflection fluorescence microscopy of fluorescently labeled, isolated polyethoxylate chains on tetramethylsiloxane-coated silica in water. Skaug et al. showed clearly the bulk-mediated diffusion of adsorbed polymers, whereby polymers appear to undergo anomalous surface diffusion with random, long jumps, when in fact they desorb from the surface, migrate through the bulk fluid in which they have a much greater diffusivity, and re-adsorb. Skaug et al. observed that the mean desorption time scaled as a power law with molecular weight N. They proposed a mechanism of adsorbed polymer segments desorbing sequentially and irreversibly, which seemed unrealistic. We viewed this as an opportunity to apply a third molecular modeling paradigm, *rare event sampling*. The polymer chains would clearly be too complex to treat as a discrete particle diffusing in a mean field potential. But with forward flux sampling, by coaxing the polymers to advance along a reaction coordinate toward desorption, we could measure the rate of desorption.

The remainder of the dissertation is organized into four chapters. In chapters two through four we present the results of the work on the three problems summarized above. The chapters are edited reproductions of three published manuscripts. We have relocated the supporting information accompanying the published articles to the appendices in revised form. In the final chapter, we draw overarching conclusions and remark on future research directions in this area.

1.5 References

(1) Kondepudi, D.; Prigogine, I. *Modern Thermodynamics: From Heat Engines to Dissipative Structures*; John Wiley & Sons, 2014.

(2) Gibbs, J. W. On the Equilibrium of Heterogeneous Substances. *Trans. Conn. Acad. Arts Sci.* **1877**, 380–520.

(3) Radke, C. J. Gibbs Adsorption Equation for Planar Fluid–fluid Interfaces: Invariant Formalism. *Adv. Colloid Interface Sci.* **2015**, *222*, 600–614.

(4) Wang, D.-N.; Stieglitz, H.; Marden, J.; Tamm, L. K. Benjamin Franklin, Philadelphia's Favorite Son, Was a Membrane Biophysicist. *Biophys. J.* **2013**, *104* (2), 287–291.

(5) Bone, W. A.; D, P.; Sc, D.; S, F. R.; Wheeler, R. V.; Sc, B. I. The Combination of Hydrogen and Oxygen in Contact with Hot Surfaces. *Phil Trans R Soc Lond A* **1906**, *206* (402–412), 1–67.

(6) Hinshelwood, C. N. *The Kinetics Of Chemical Change In Gaseous Systems*; Oxford At The Clarendon Press, 1929.

(7) Derrick, M. E. Agnes Pockels, 1862-1935. *J. Chem. Educ.* **1982**, *59* (12), 1030.

(8) Langmuir, I. The Constitution and Fundamental Properties of Solids and Liquids. II. Liquids. *J. Am. Chem. Soc.* **1917**, *39* (9), 1848–1906.

(9) Rayleigh. Surface Tension. *Nature* **1891**, *43* (1115), 437.

(10) Wise, G. Ionists in Industry: Physical Chemistry at General Electric, 1900-1915. *Isis* **1983**, *74* (1), 7–21.

(11) Onsager, L. Theories of Concentrated Electrolytes. *Chem. Rev.* **1933**, *13* (1), 73–89.

(12) Kirkwood, J. G. Statistical Mechanics of Fluid Mixtures. *J. Chem. Phys.* **1935**, *3* (5), 300–313.

(13) Einstein, A. Über Die von Der Molekularkinetischen Theorie Der Wärme Geforderte Bewegung von in Ruhenden Flüssigkeiten Suspendierten Teilchen. *Ann. Phys.* **1905**, *322* (8), 549–560.

(14) von Smoluchowski, M. Zur Kinetischen Theorie Der Brownschen Molekularbewegung Und Der Suspensionen. *Ann. Phys.* **1906**, *326* (14), 756–780.

(15) *Free Energy Calculations*; Chipot, C., Pohorille, A., Eds.; Castleman, A. W., Toennies, J. P., Yamanouchi, K., Zinth, W., Series Eds.; Springer Series in CHEMICAL PHYSICS; Springer Berlin Heidelberg: Berlin, Heidelberg, 2007; Vol. 86.

(16) Ward, A. F. H.; Tordai, L. Time-Dependence of Boundary Tensions of Solutions I. The Role of Diffusion in Time-Effects. *J. Chem. Phys.* **1946**, *14* (7), 453–461.

(17) Casandra, A.; Ismadji, S.; Noskov, B. A.; Liggieri, L.; Lin, S.-Y. A Study on the Method of Short-Time Approximation – Criteria for Applicability. *Int. J. Heat Mass Transf.* **2015**, *90*, 752–760.

(18) Mysels, K. Diffusion-Controlled Adsorption Kinetics. General Solution and Some Applications. *J. Phys. Chem.* **1982**, *86* (23), 4648–4651.

(19) Metropolis, N. The Beginning of the Monte Carlo Method. *Los Alamos Science*. 1987, pp 125–130.

(20) Metropolis, N.; Rosenbluth, A. W.; Rosenbluth, M. N.; Teller, A. H.; Teller, E. Equation of State Calculations by Fast Computing Machines. *J. Chem. Phys.* **1953**, *21* (6), 1087–1092.

(21) Rosenbluth, M. N.; Rosenbluth, A. W. Monte Carlo Calculation of the Average Extension of Molecular Chains. *J. Chem. Phys.* **1955**, *23* (2), 356–359.

(22) Alder, B. J.; Wainwright, T. E. Phase Transition for a Hard Sphere System. *J. Chem. Phys.* **1957**, *27* (5), 1208–1209.

(23) Davies, J. T. Adsorption of Long-Chain Ions. I. *Proc. R. Soc. Lond. Ser. Math. Phys. Sci.* **1958**, *245* (1242), 417–428.

(24) MacLeod, C. A.; Radke, C. J. Charge Effects in the Transient Adsorption of Ionic Surfactants at Fluid Interfaces. *Langmuir* **1994**, *10* (10), 3555–3566.

(25) Nikas, Y. J.; Puvvada, S.; Blankschtein, D. Surface Tensions of Aqueous Nonionic Surfactant Mixtures. *Langmuir* **1992**, *8* (11), 2680–2689.

(26) Pastor, R. W.; MacKerell, A. D. Development of the CHARMM Force Field for Lipids. *J. Phys. Chem. Lett.* **2011**, *2* (13), 1526–1532.

(27) Oostenbrink, C.; Villa, A.; Mark, A. E.; Van Gunsteren, W. F. A Biomolecular Force Field Based on the Free Enthalpy of Hydration and Solvation: The GROMOS Force-Field Parameter Sets 53A5 and 53A6. *J. Comput. Chem.* **2004**, *25* (13), 1656–1676.

(28) Dickson, C. J.; Madej, B. D.; Skjevik, Å. A.; Betz, R. M.; Teigen, K.; Gould, I. R.; Walker, R. C. Lipid14: The Amber Lipid Force Field. *J. Chem. Theory Comput.* **2014**, *10* (2), 865–879.

(29) Jorgensen, W. L.; Laird, E. R.; Nguyen, T. B.; Tirado-Rives, J. Monte Carlo Simulations of Pure Liquid Substituted Benzenes with OPLS Potential Functions. *J. Comput. Chem.* **1993**, *14* (2), 206–215.

(30) Jorgensen, W. L.; Maxwell, D. S.; Tirado-Rives, J. Development and Testing of the OPLS All-Atom Force Field on Conformational Energetics and Properties of Organic Liquids. *J. Am. Chem. Soc.* **1996**, *118* (45), 11225–11236.

(31) Jorgensen, W. L.; Tirado-Rives, J. The OPLS [Optimized Potentials for Liquid Simulations] Potential Functions for Proteins, Energy Minimizations for Crystals of Cyclic Peptides and Crambin. *J. Am. Chem. Soc.* **1988**, *110* (6), 1657–1666.

(32) Fuchs, P. F. J.; Hansen, H. S.; Hünenberger, P. H.; Horta, B. A. C. A GROMOS Parameter Set for Vicinal Diether Functions: Properties of Polyethyleneoxide and Polyethyleneglycol. *J. Chem. Theory Comput.* **2012**, *8* (10), 3943–3963.

(33) Chang, C.-H.; Franses, E. I. Adsorption Dynamics of Surfactants at the Air/Water Interface: A Critical Review of Mathematical Models, Data, and Mechanisms. *Colloids Surf. Physicochem. Eng. Asp.* **1995**, *100*, 1–45.

CHAPTER 2

Reversible and irreversible adsorption energetics of poly(ethylene glycol) and sorbitan poly(ethoxylate) at a water/alkane interface

* Reprinted with permission from Huston, K. J., & Larson, R. G. (2015). Reversible and irreversible adsorption energetics of poly(ethylene glycol) and sorbitan poly(ethoxylate) at a water/alkane interface. *Langmuir*. https://doi.org/10.1021/acs.langmuir.5b00398. Copyright © 2015 American Chemical Society.

Chapter 2 describes the work published in 2013 (Figure 2-1). We simulated poly(ethylene glycol) (PEG) oligomers and model Tween 80 (polyoxyethylene sorbitan monooleate) molecules at water/alkane interfaces. Using the weighted histogram analysis method (WHAM), including an extension of WHAM to two reaction coordinates to remove hysteresis, we calculated interfacial potentials of mean force (PMFs) for PEG and Tween 80 using three forcefields: the atomistic GROMOS 53a6OXY+D and two coarse-grained (CG) MARTINI forcefields. Because the forcefields have not yet been validated for PEO adsorption to hydrophobic interfaces, we calculated PMFs for alcohol ethoxylates $C_{12}E_2$ and $C_{12}E_8$ and find that they agree with semi-empirical results by Mulqueen and Blankschtein [Langmuir 18, 2 (2002)] for the GROMOS 53a6OXY+D forcefield, whereas for both MARTINI forcefields PEO adsorbs too weakly to a clean hydrophobic interface. One MARTINI forcefield incorrectly shows depletion rather than adsorption to a clean hydrophobic interface. We found that the adsorption free energy for PEG oligomers at a clean, planar water/alkane interface is around 1.3 kBT per monomer for the atomistic forcefield, but is less than half of this for the two CG forcefields. With the newly validated GROMOS 53a6OXY+D forcefield, we bracketed the dilute adsorption free energy for a model Tween 80 molecule at the clean water/squalane interface. We also calculated the pressure-area isotherm. We exploit these data with the Nikas-Mulqueen-Blankschtein (NMB) theory and a simple transport model to demonstrate a transition from irreversible to reversible adsorption with increasing surface coverage, consistent with experimental results of Reichert and Walker [Langmuir 29, 6 (2013)].

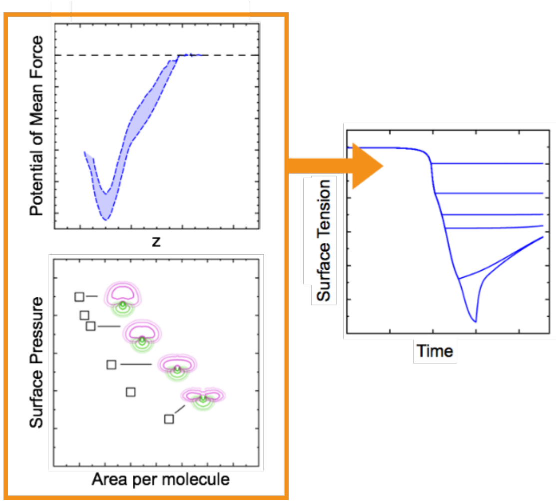

Figure 2-1. Graphical overview of study.

2.1 Motivation

Poly(ethoxylates) are a major subset of nonionic surfactants. Three sorbitan poly(ethoxylates) (SPEs) with fatty acid esters — Tween 80, Tween 85, and Span 80 — were deployed as components of Corexit oil dispersant in response to the Deepwater Horizon incident.[1] The active ingredients in Corexit have been investigated with regard to phase behavior[2], emulsion stability[3], and dispersant effectiveness[4,5]. But their adsorption energetics are not well understood, and adsorption dynamics were only recently studied. Adsorption dynamics are potentially important for tip-streaming in oil droplet breakup.[6] Using continuous-flow tensiometry, Reichert and Walker[7] examined the transient adsorption and desorption of Tween 80 at the water/squalane interface and demonstrated two adsorption regimes: irreversible adsorption and partially reversible adsorption, separated by a critical surface tension. Irreversible adsorption occurred above a critical surface tension of 32 mN/m, where surface coverage was relatively sparse. Once surface loading became high enough to drop the surface tension below this critical value, partial desorption occurred with rinsing, but rinsing never brought the surface tension above 32 mN/m, suggesting, again, that below a surface density corresponding to this surface tension, adsorption was essentially irreversible.

To understand these experimental results, we exploit atomistic molecular dynamics (MD) simulation using the Nikas-Mulqueen-Blankschtein (NMB) theory10 to predict the bulk-interface equilibrium of a model Tween 80 molecule. Using the NMB approach, the dilute adsorption free energy and the pressure-area isotherm together yield the bulk-interface equilibrium. Equipped with this equilibrium relation and a simple transport model, we predict the diffusion-controlled sorption dynamics, reproduce a transition from irreversible to reversible adsorption, and analyze the phenomenon.

Before we can trust a forcefield to accurately predict surfactant adsorption, we must validate it. Quantitative validation of a forcefield for PEG/PEO adsorption has not been reported previously, so a portion of this work is also dedicated to that purpose.

2.2 Tween 80 model

Tween 80 is a complex mixture, and its components are not defined well enough to simulate in totality, even if the computational power were available for such a task.[8] Sorbitan poly(ethoxylates) – a major component of Tween 80 – can vary in

- Number and type of hydrophobic tails
- Number of EO units
- Distribution of EO units among the head chains

- Stereochemistry

Sorbitan has four alcohol groups that can be ethoxylated. Ethoxylation of linear alcohols has been modeled by kinetics with a slow initiation step and faster propagation step.[9,10] It may thus be likely to find incompletely ethoxylated – and even unethoxylated – alcohols on sorbitan, so the molecular structure can vary widely. Our group previously studied the influence of some Tween 80 structural variations on interfacial tension and molecular conformation. Here, we adopt the stoichiometrically "average" structure as our characteristic Tween 80 molecule, with four equal-length ethoxylate groups shown in Figure 2-2.

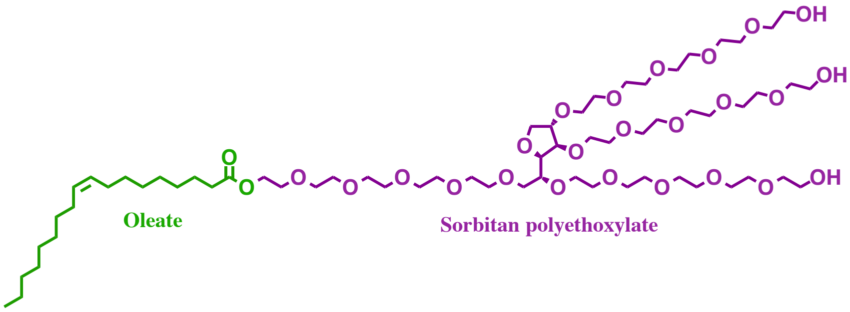

Figure 2-2. Stoichiometric mean structure of Tween 80. The oleate tail is colored green, and the ethoxylated headgroup is colored purple. This color scheme is used throughout the work.

For MD simulation of Tween 80, we primarily use the GROMOS 53a6OXY+D (united-atom, i.e., atomistic with implicit nonpolar hydrogen)[11] forcefield. We also examine MARTINI coarse-grained forcefields using one set of PEO parameters by Lee et al.[12] and another by Rossi et al. [13]. The models are detailed in the Supporting Information.

2.3 Forcefield considerations

Before we attempt to calculate adsorption free energies, we consider whether the GROMOS 53a6OXY+D-based forcefield of Tang et al.[14] will realize correct thermodynamics for Tween 80 adsorption to a hydrocarbon/water interface. Tween 80 consists of furan, PEG, and fatty acid ester tail(s). The tail and PEG dwarf the furan, so we omit the furan from consideration. Then we predict two major contributions to the adsorption free energy of Tween 80 due to

- Transfer of the hydrophobic tail from oil into water
- Desorption of PEG chains from the hydrophobic surface

Accurate transfer of the hydrophobic tail from oil into water is expected from GROMOS 53a6OXY+D due to its parameterization (more discussion in SI – Appendix A). Desorption of PEG chains from the hydrophobic surface has less certain accuracy. Modern PEG/PEO forcefields are tuned to predict bulk-phase behavior, such as pure liquid densities, conformer populations, Rg scaling with chain length, and oil-water transfer free energies.[11,15] However, these metrics don't test the affinity for hydrophobic interfaces which experiments have demonstrated.[16,17,18] To validate PEG forcefields for adsorption strength, we will compare with dilute-limit adsorption free energy parameters from Mulqueen and Blankschtein.[11] Mulqueen and Blankschtein fitted experimental adsorption isotherms for ethoxylated alcohols (CnEm surfactants) including $C_{12}E_2$ and $C_{12}E_8$. Because $C_{12}E_8$ has 6 more ethylene oxide (EO) units than $C_{12}E_2$, its enhanced surface activity measures the surface activity of EO. We can therefore exploit the difference in the dilute adsorption free energies of $C_{12}E_2$ and $C_{12}E_8$ to assess the accuracy of PEG adsorption strength in a forcefield. This validation helps to assure the accuracy of PMFs for ethoxylated surfactants, including Tween 80.

2.4 Previous simulations

Among published studies with molecular simulation of surfactants, few predict surfactant bulk-interface equilibrium, and none predict dynamic tensiometry. Most are restricted to either the bulk (e.g. micelle structure, phase behavior) or the interface (e.g. pressure-area isotherms). Our group previously simulated Tween 80 isomers, measuring surface tension at a fixed area per molecule. We found that the distribution of EO groups among the four PEG chains within the head controls the conformational flexibility of the head, which in turn affects interfacial tension in a crowded monolayer.[14] Many simulation-derived pressure-area isotherms have been reported for other surfactants, especially lipid monolayers and bilayers.[19,20,21,22] However, these have generally not been exploited for prediction of bulk-phase activity.

We are only aware of two instances in the literature where bulk-interface equilibrium of surfactants was predicted, both by Howes and Radke.[23,24] Howes and Radke calculated the adsorption isotherms of Lennard-Jones surfactants by explicit, unbiased simulation. This is, however, only possible for highly coarse-grained surfactants which do not adsorb so strongly that the bulk concentration becomes difficult to measure. For example, Wang and Larson simulated sodium dodecyl sulfate using the coarse-grained implicit-solvent Dry Martini forcefield. Despite its performance advantages[25], they found that the concentration of surfactant was not “detactable” in the range below interface saturation, so they could not predict bulk-interface equilibrium.

We are not aware of any published use of enhanced sampling techniques to predict bulk-interface equilibrium of surfactants. Nor are we aware of a prior publication in which bulk-interface equilibrium is predicted exclusively with data from atomistic simulations. We do both in this study.

2.5 Methods

2.5.1 Forcefields

For our atomistic simulations, we employ a Tween 80 model we used previously[14], based on the united-atom (implicit nonpolar hydrogen) GROMOS 53a6OXY+D forcefield. For our coarse-grained (CG) simulations, we employ two different CG Tween 80 models. Both CG models follow the Amani et al.[26] scheme of putting angle constraints on three PEG beads to represent the rigid furan ring, and both use the 4-bead oleate of Schäfer, Marrink, et al.[27] The two CG models differ by their PEG parameters – those from Lee et al.[12] versus Rossi et al.[13] The models are discussed in more detail in the Supporting Information.

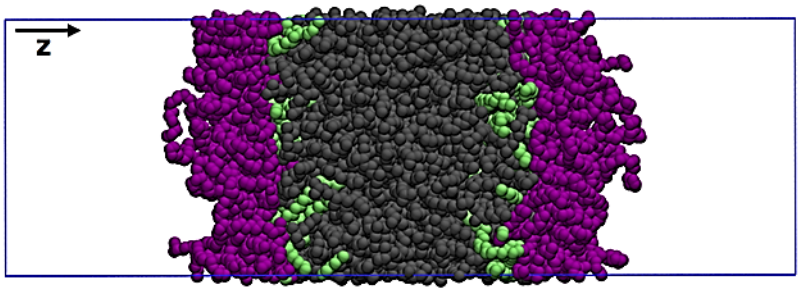

Figure 2-3. Simulation box of size 6×6×18 nm^3 with 25 Tween 80 molecules on each side for measurement of interfacial tension and structure of a 1.44 nm^2/molecule monolayer. The periodic boundary is outlined in blue, squalane molecules are gray, Tween 80 tails are green, and Tween 80 heads are purple. Water molecules are present, but not drawn. The arrow points in the z direction, normal to the interface. Figure is best viewed in color.

2.5.2 Simulation setup for interfacial tension and monolayer structure

For measurements of interfacial tension and monolayer structure at varying surface coverage, the periodic box was initially sized 6×6×18 nm^3. Surfactant molecules were arrayed onto two rectangular lattices with tails facing each other. A space of 6 nm was left between the lattices and filled with squalane (a 30-carbon lightly-branched alkane) or another model oil (dodecane for PEG; hexadecane for $C_{12}E_2$ and $C_{12}E_8$), and the space outside was filled with water. Figure 2-3 shows the box with 25 surfactant molecules on each side (water not drawn), to simulate an interfacial monolayer with 1.44 nm^2/molecule. We minimized energy with the steepest-descent algorithm, followed by a 20 ns run at fixed NAPZT, where A indicates that we held constant the dimensions of the box tangential to the interface, and PZ indicates that we held constant the normal stress at 1 bar. For this initial 20 ns run, we chose the Berendsen barostat[28] to equilibrate rapidly. We then ran for at least 200 ns at fixed NAPZT using the Parrinello-Rahman barostat[29] at 1 bar. At all stages, we fixed the temperature at 300 K using the stochastic velocity rescale thermostat of Bussi, Donadio, and Parrinello.[30]

2.5.3 Simulation setup for 1D-biased umbrella sampling

We measured interfacial potentials of mean force (PMFs) along an adsorption coordinate Z, where Z is the distance (projected along the z-axis) between the test surfactant's center of mass and a reference point in the oil slab. Any reference point suffices, so long as it is fixed relative to the interface. We used the oil slab's center of mass as our reference point.

For poly(ethylene oxide) oligomers and the linear alcohol ethoxylates, we found that a 1D harmonic bias on the surfactant's center of mass (Z) provided good conformational sampling. In these 1D-biased simulations, a test surfactant was placed at one interfaces of a clean 6 nm oil cube, surrounded by water in a periodic box sized 6×6×18 nm^3. After energy minimization and a z-pressure equilibration with a Berendsen barostat for 20 ns, the test surfactant was pulled to the midplane of the oil slab at the rate 250 pm/ns. It was then pulled out of the oil into the water at the same rate. From this pulling trajectory, we took initial configurations for a set of partially overlapping windows along the adsorption coordinate. For each window in the set, we simulated the test molecule with harmonic restraints at a 0.12 nm interval, with spring constant k = 1000 kJ mol^{-1} nm^{-2}. Each window ran for some duration depending on the species: >100 ns for Tween 80, 40 ns for the alkyl ethoxylates, 20 ns for PEG/PEO. After sampling these windows, the PMF was constructed using the weighted histogram analysis method[31] (WHAM) as implemented by Grossfield.[32] We vertically shifted the resulting PMF to be zero in bulk water so that

$$W_Z(z) = -k_B T \ln \left[\frac{\rho_Z(z)}{\rho_Z^w} \right] \qquad (1)$$

where W_Z is the 1D interfacial potential of mean force on the surfactant molecule, $\rho_Z(z)$ is the unbiased probability density of finding the molecule at z, and ρ_Z^w is the constant probability density of finding the molecule in bulk water.

2.5.4 2D-biased umbrella sampling

As stated previously, 1D-biased simulation sufficed for measuring PEG oligomer, $C_{12}E_2$, and $C_{12}E_8$ PMFs. However, in 1D-biased simulations of Tween 80, as the surfactant moved from oil into bulk water, the tail was comparably stable either *extended* toward the oil or *retracted* into the water, and the barrier between these microstates was not easily crossed with unaided molecular dynamics. Symptomatically, the generated PMF would depend on the initial pulling direction (whether the surfactant was approaching or departing the hydrocarbon slab), giving rise to hysteresis. To overcome this, we used a 2D-biased umbrella sampling technique that introduced a second harmonic bias on the surfactant tail's center of mass Y. The method and analysis is detailed in the Supporting Information.

2.6 Adsorption free energy and adsorption coefficient

We consider a two-phase, oil-water system with a single nonionic surfactant component that is insoluble in the oil. Following the Nikas-Mulqueen-Blankschtein[33,34] formalism, we write the surfactant chemical potential at the interface (μ_s^σ) and in aqueous bulk (μ_s^w) at sub-CMC concentrations in Eqns. 2 and 3, respectively:

$$\mu_s^\sigma = \mu_s^{\sigma,0} + k_B T \ln \Gamma_s + \int_\infty^a \frac{\partial\left(\Pi(a') - \Pi^{\mathrm{id}}(a')\right)}{\partial a'} a' da' \tag{2}$$

In Eqn. 2, Γ_s is the surface coverage of adsorbed surfactant, a is the area per adsorbed surfactant molecule ($a = 1/\Gamma_s$), $\Pi(a')$ is the surface pressure for an interfacial monolayer with area per molecule a', and $\Pi^{\mathrm{id}}(a')$ is the ideal surface pressure ($\Pi^{\mathrm{id}} = \frac{k_B T}{a'}$). The integral, which we call the marginal excess pressure-area work (MEPAW) accounts for the change in the surface chemical potential due to crowding surfactants at the interface. It has been translated from its original extensive variables to intensive a (see SI for derivation – Appendix A).

$$\mu_s^w = \mu_s^{w,0} + k_B T \ln \frac{c_s^w}{c_w^w} \tag{3}$$

In Eqn. 3, c_s^w is the concentration of surfactant in the aqueous phase, and c_w^w is the concentration of water in the aqueous phase. The quantities $\mu_s^{w,0}$ and $\mu_s^{\sigma,0}$ are standard-state chemical potentials. We define a dilute adsorption free energy $\Delta\mu^{\sigma/w,0} \equiv \mu_s^{\sigma,0} - \mu_s^{w,0} + k_B T \ln c_w^w$ similar to that of Nikas, Puvvada, and Blankschtein, which they call simply the "adsorption free energy".[33] The dilute adsorption free energy $\Delta\mu^{\sigma/w,0}$controls the bulk-interface equilibrium in the dilute limit through a form of Henry's law:

$$\Delta\mu^{\sigma/w,0} = -k_B T \ln \lim_{c_s^w \to 0} \frac{\Gamma_s}{c_s^w} \tag{4}$$

Note that $\Delta\mu^{\sigma/w,0}$ has a unit-dependent shift because the adsorption coefficient Γ_s/c_s^w has a unit of length. To avoid carrying the auxiliary unit dependence, we instead report a surfactant's affinity for the clean interface in terms of the dilute adsorption coefficient $h_p^{\sigma/w,0}$:

$$h_p^{\sigma/w,0} \equiv \lim_{c_s^w \to 0} \frac{\Gamma_s}{c_s^w} = e^{-\frac{\Delta\mu^{\sigma/w,0}}{k_B T}} \tag{5}$$

We also define a quantity $\Delta\mu^{\sigma/w^{\mathrm{id}}}$, the ideal-bulk adsorption free energy:

$$\Delta\mu^{\sigma/w^{\mathrm{id}}} = \Delta\mu^{\sigma/w,0} + \int_{\infty}^{a} \frac{\partial\left(\Pi(a') - \Pi^{\mathrm{id}}(a')\right)}{\partial a'} a' da' \tag{6}$$

The ideal-bulk adsorption free energy $\Delta\mu^{\sigma/w^{\mathrm{id}}}$ controls the bulk-interface equilibrium of outside the dilute limit, but still below the CMC.

$$\frac{\Gamma_s}{c_s^w} = e^{-\frac{\Delta\mu^{\sigma/w^{\mathrm{id}}}}{k_B T}} \qquad \text{where } c_s^w \ll \text{CMC} \tag{7}$$

Crucially, note that whereas $\Delta\mu^{\sigma/w,0}$ is constant, $\Delta\mu^{\sigma/w^{\mathrm{id}}}$ increases with decreasing a, and $\Delta\mu^{\sigma/w^{\mathrm{id}}}$ tends to $\Delta\mu^{\sigma/w,0}$ as a tends to infinity. For detailed derivation and further discussion of Eqns. 2-7, refer to the Supporting Information.

2.7 Adsorption coefficient as normalized Gibbs surface excess

In the previous section, we defined the dilute adsorption free energy $\Delta\mu^{\sigma/w,0}$, which is related to the dilute adsorption coefficient by Eqns. 4 and 5. Given an interfacial potential of mean force (PMF), we can calculate the adsorption coefficient using

$$h_p \equiv \frac{\Gamma_s}{c_s^w} = \int_{-\infty}^{z_i} \left(e^{-\beta W_Z(z)} - \frac{c_s^o}{c_s^w}\right) dz + \int_{z_i}^{\infty} \left(e^{-\beta W_Z(z)} - 1\right) dz \tag{8}$$

where $z = z_i$ is the location of a Gibbs dividing surface, $W_Z(z)$ is the PMF defined in Eqn. 1, and $c_{s,o}$ is the concentration of surfactant in bulk oil. For our purposes, the subdomain $z > z_i$ is aqueous, and the subdomain $z < z_i$ is oil in which the surfactant is approximately insoluble. In practice, the integral is numerically evaluated over a finite range. The integral is insensitive to the bounds of this range so long as they bracket the interface, because at the interface $e^{-\beta W_Z(z)} \gg 1 \gg \frac{c_s^o}{c_s^w}$. For the same reason, precise positioning of the Gibbs dividing surface is unnecessary, and c_s^o/c_s^w is approximately zero. If we measure the PMF for an isolated surfactant, then we can calculate the dilute adsorption coefficient h_p^0 using Eqn. 8, and we can calculate the dilute adsorption free energy $\Delta\mu^{\sigma/w,0}$ in turn using Eqn. 4.

2.8 Surface pressure

As mentioned before, the marginal excess pressure-area work (MEPAW) gives the increase in adsorption free energy upon crowding surfactant at the interface. To calculate MEPAW, we need the surfactant's pressure-area isotherm, which we interpolate from simulation-derived pressure-area data. Surface pressure Π is the negative deviation in interfacial tension γ from the clean interfacial tension γ_0. That is, $\Pi = \gamma_0 - \gamma$. To obtain γ from simulations, we analyzed at least 200 ns of data using the g_energy utility, which calculates the instantaneous surface tension from components of the stress tensor given a simulation box with two interfaces:[35]

$$\gamma(t) = \frac{L_z(t)}{2}\left(P_{zz}(t) - \frac{P_{xx}(t) + P_{yy}(t)}{2}\right) \tag{9}$$

Simulations that span a range of surface coverage (Γ_s) including the clean interface ($\Gamma_s = 0$) yield a range of surface tensions (γ) including the clean interfacial tension (γ_0). We can then readily obtain pressure-area data. To estimate the pressure-area isotherm $\Pi(a)$ for MEPAW calculation, we fitted an interpolating piecewise function to the pressure-area data. At low area/high coverage, we used a sum of exponentials; and at high area/low coverage, we switched to a 2D vdW-like equation of state with an excluded-area term (see Eqn. S4 in SI):

$$\Pi = \begin{cases} p_0 + \sum_{i=1}^{n} p_i e^{-q_i(a-a_0)} & \text{for } a < a_{\text{switch}} \\ \dfrac{k_B T}{a - A} & \text{for } a > a_{\text{switch}} \end{cases} \tag{10}$$

where A, $\{p_i\}$, $\{q_i\}$, and a_0 are fitting constants. a_{switch} is chosen as the maximum a in the pressure-area data. The interpolation is imperfect, as evidenced the discontinuity at $a = 12$ nm in Fig. 2-8a. There is opportunity for improvement, but it suffices for this work, given the large uncertainty imposed by hysteresis in the atomistic Tween 80 PMF. From the fitted $\Pi(a)$ isotherm, the MEPAW can be calculated as the integral in Eqns. 2 and 6. For details about fitting, computation, and error analysis of the piecewise isotherm and associated MEPAW, see the SI in Appendix A.

2.9 Transport model and simulated tensiometry

We simulated continuous-flow tensiometry with a pseudo-steady thin film diffusion model for a single surfactant component. The pseudo-steady assumption is justified because amount of surfactant adsorbed before establishing the concentration profile should be small relative to the total adsorbed amount at equilibrium. The equation for thin-film diffusion is

$$\frac{\partial \Gamma_s}{\partial t} = D \frac{c_s^{w,\text{bulk}} - c_s^{w,\text{surface}}}{\delta} \tag{11}$$

where Γ_s is the surface coverage of surfactant, $c_s^{w,\text{bulk}}$ is the aqueous concentration of surfactant, $c_s^{w,\text{surface}}$ is the aqueous sub-surface concentration, D_s is the surfactant diffusion coefficient, and δ is the concentration boundary layer thickness. Alvarez et al.[36] have noted that for continuous-flow tensiometry experiments with sufficiently low flow rates, the transport may be modeled as diffusion over Stokes flow around a spherical droplet.[37] In this case, the concentration boundary layer thickness δ is set by the Péclet number Pe and capillary bubble radius b. Because Marangoni stress arising from flow-driven gradients in surfactant coverage counteracts the hydrodynamic stress, a surfactant-coated fluid-fluid interface can behave as a rigid surface. The boundary layer thickness for a rigid surface under such conditions is approximately

$$\delta_R \approx \left(\frac{4}{3\mathrm{Pe}}\right)^{\frac{1}{3}} b \tag{12}$$

In this work, we assume transport is diffusion-controlled, such that coverage Γ_s and aqueous sub-surface concentration $c_s^{w,\mathrm{surface}}$ of surfactant are in local equilibrium. Because we compare with sub-CMC tensiometry data[7], the ideal-bulk assumption is justified, so we can calculate the $c_s^{w,\mathrm{surface}}$ at each time step using Eqn. 7. With $c_s^{w,\mathrm{bulk}}$ fixed, the flux in Eqn. 11 was evaluated to update Γ with a timestep dt. This was performed iteratively for the duration of the simulated tensiometry. At a pre-determined time, $c_s^{w,\mathrm{bulk}}$ was switched from its initial value to zero, to model the rinsing step in the Reichert and Walker experiments. In order to plot surface tension, the surface pressure was subtracted from the experimental interfacial tension of the water-squalane interface – 52.5 mN/m.[38]

2.10 Software and data

Our MD simulation engine was Gromacs 4.6.1.[39] We relied upon the analysis tools packaged with Gromacs and the MDAnalysis Python module.[40] We calculated PMFs with Alan Grossfield's implementation of WHAM.[32] SI section S.3.2 describes calculation of the intramolecular density contours. Simulation topology files, trajectories, and data plotted in figures have been uploaded to https://data.gulfresearchinitiative.org/data/R1.x141.064:0066/.

2.11 Results and discussion

2.11.1 Validation of GROMOS 53a6$_{OXY+D}$ forcefield for PEG adsorption strength by literature comparison of $C_{12}E_2$ and $C_{12}E_8$ dilute adsorption free energies

Using Eqn. 8, and the PMFs in Figure 2-4, we calculated dilute adsorption coefficients $h_p^{\sigma/w,0}$ for $C_{12}E_2$ and $C_{12}E_8$ using the MARTINI Lee et al. and GROMOS 53a6OXY+D forcefields. Alternately, we could have reported dilute adsorption free energies $\Delta\mu^{\sigma/w,0}$ via Eqn. 4, but these have a unit-dependent shift. Instead, we compare the difference between dilute adsorption free energies for $C_{12}E_8$ and $C_{12}E_2$, $\Delta\Delta\mu^{\sigma/w,0}$. This comparison eliminates the unit-dependent shift, and we can make a direct comparison with Mulqueen and Blankschtein.[34]

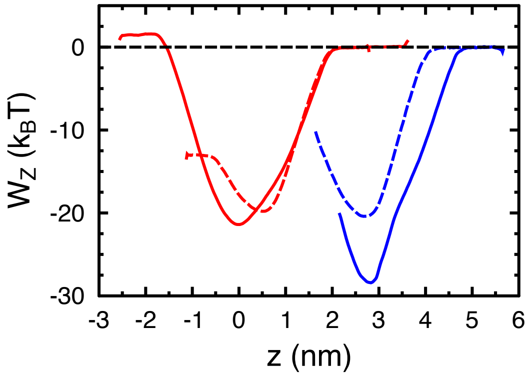

		$h_p^{\sigma/w,0}$(nm)	$\Delta\Delta\mu^{\sigma/w,0}$
MARTINI, Lee et al.	$C_{12}E_2$	$(1.6\pm0.3)\times10^8$	-1.6±0.3
	$C_{12}E_8$	$(7.9\pm1.7)\times10^8$	
GROMOS 53a6$_{OXY+D}$	$C_{12}E_2$	$(3.1\pm1.6)\times10^8$	-7.5±0.7
	$C_{12}E_8$	$(5.6\pm3.1)\times10^{11}$	
Mulqueen and Blankschtein	$C_{12}E_2$	-	-7.8
	$C_{12}E_8$	-	

Figure 2-4. PMFs of $C_{12}E_2$ (dashed) and $C_{12}E_8$ (solid) at the hexadecane/water interface. PMF minima occur near the hexadecane/water interface; to the left is hexadecane, and to the right is water. Arbitrary shifts in z have been applied for clarity. The interface is near $z = 0$ for the Lee et al. forcefield and near $z = 2.5$ for the GROMOS forcefield. Dilute adsorption coefficients $h_p^{\sigma/w,0}$ were computed from the PMFs and are tabulated at the right. $\Delta\Delta\mu^{\sigma/w,0}$ in k_BT for the two forcefields and from Mulqueen and Blankschtein are also shown.

The dilute adsorption coefficient $h_p^{\sigma/w,0}$ for $C_{12}E_2$ is similar for the GROMOS 53a6OXY+D and Lee et al. forcefields. However, the six additional EO units in $C_{12}E_8$ enhances adsorption much more for the 53a6OXY+D forcefield than for the Lee et al. forcefield. According to Mulqueen and Blankschtein, the change $\Delta\Delta\mu^{\sigma/w,0}$ upon adding six EO units is -7.8 kBT.[34] From GROMOS 53a6OXY+D simulation, we get $\Delta\Delta\mu^{\sigma/w,0} =$ -7.5±0.7 kBT (95% C.I.). This close agreement validates the GROMOS 53a6OXY+D model's accuracy at hydrophobic interfaces. The MARTINI forcefield of Lee et al. fails this test with $\Delta\Delta\mu^{\sigma/w,0}$ = -1.6±0.3 kBT, so its accuracy for PEG/PEO adsorption is suspect, especially at low surface coverage. In the next section, we see that adsorption of PEG/PEO oligomers is much weaker for the Lee et al. forcefield than for GROMOS 53a6OXY+D.

2.11.2 Existing MARTINI CG forcefields for PEG/PEO significantly underestimate adsorption strength

In Figure 2-5, we plot interfacial PMFs for hydroxyl-terminal PEG chains for the atomistic GROMOS 53a6OXY+D forcefield and methyl-terminal PEG chains for the coarse-grained MARTINI forcefields by Lee et al. and Rossi et al.[12,13] Note that end-beads have been developed for the MARTINI forcefields to model hydroxyl-terminal chains as well.[41,13] We tested the hydroxyl-terminal versions of the CG models, and observed similar trends with overall weaker adsorption (see SI).

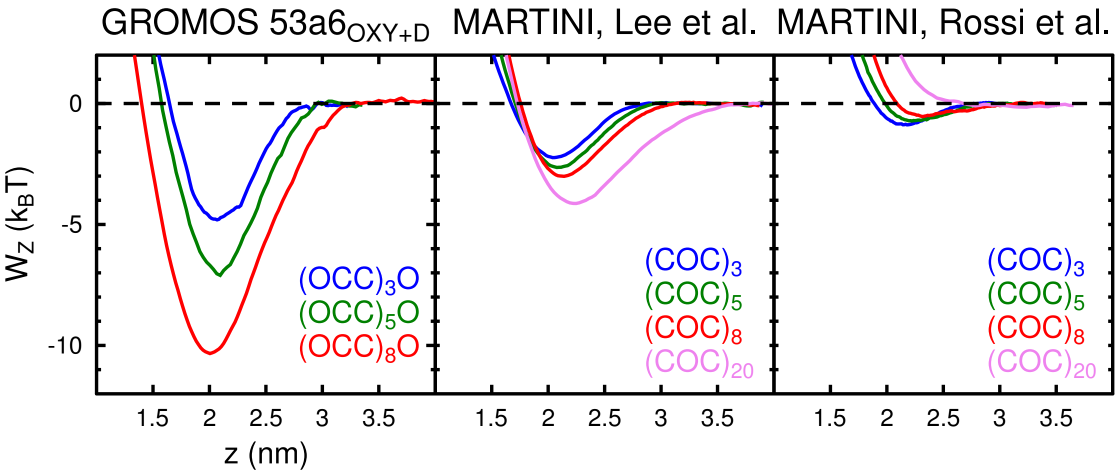

Figure 2-5. PMFs of PEG oligomers at the water/dodecane interface plotted against adsorption coordinate z, the molecule's center of mass relative to a fixed point in the oil. The interface is near z = 2 nm in each case; dodecane is to the left, and water is to the right. (COC)n denotes a methyl-terminal chain, and (OCC)nO denotes hydroxyl-terminal chain.

The forcefield of Rossi et al. exhibits a qualitative failure, with vanishing adsorption and the onset of depletion for sufficiently long chains. The affinity of its monomers to hydrophobic surfaces is clearly too weak. On the other hand, GROMOS 53a6OXY+D and Lee et al. both show deepening potential minima and hence increasingly strong adsorption for chains of increasing length. The PMF minimum depends roughly linearly on PEG chain length for G53a6OXY+D in the range tested, around -1.1 kBT per monomer, comparable to the -1.3±0.2 kBT per monomer observed from the CnEm comparison. For Lee et al., the free energy change per monomer is significantly smaller.

Based on these results, the PEG/PEO forcefield of Rossi et al. could definitely be ruled out as accurately modeling adsorption to hydrophobic surfaces, because long chains show depletion rather than adsorption. The forcefield of Lee et al. gives chains that adsorb, but as shown in the previous section, the adsorption is again much weaker than for GROMOS 53a6OXY+D.

2.11.3 Tween 80 interfacial potentials of mean force

Finally, we measured PMFs for Tween 80 with each forcefield. We used 2D-biased sampling to calculate the PMFs (as described in Methods) for the two MARTINI forcefields, drawn as solid lines in Figure 2-6. The 2D-biased sampling was too expensive for the atomistic Tween 80, so we contented ourselves with the hysteretic 1D-biased PMFs that bracket the correct PMF (see SI for more discussion). These are drawn as dashed lines in Fig. 2-6.

The Lee et al. and Rossi et al. forcefields differ only in their parameters for PEG. As expected from the PMFs for PEG oligomers, the Lee et al. Tween 80 has a deeper PMF and strong adsorption. Likewise, the GROMOS 53a6OXY+D gives a PMF that is much deeper than its coarse-grained counterparts. The differences between all three Tween 80 PMFs are due primarily to the surface affinity of PEG. To confirm this, we compared oleic acid PMFs for MARTINI and GROMOS 53a6, and observed nearly identical PMF differences between the aqueous plateau and the interfacial minimum (see SI).

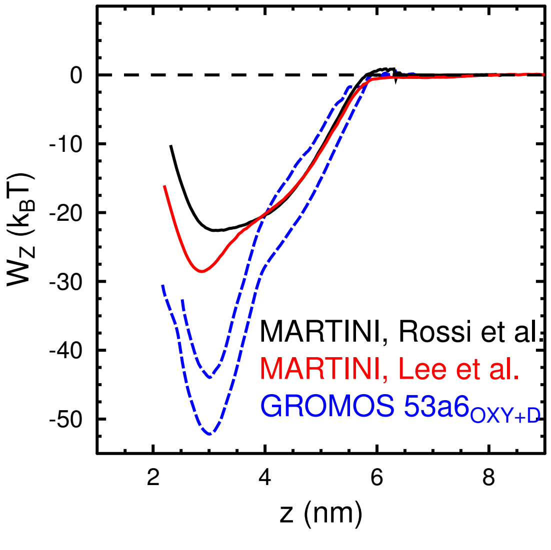

Figure 2-6. PMFs of Tween 80 at the water/squalane interface (black: Martini, Rossi et al.; red: Martini, Lee et al.; blue: GROMOS 53a6OXY+D) For GROMOS 53a6OXY+D, the two dashed blue lines are hysteretic PMFs generated for inward (upper line) and outward (lower line) pulling. The PMFs for the two MARTINI forcefields were generated with 2D-biased sampling. The local maximum in the black curve is an artifact of the partial 2D sampling technique.

We calculated Tween 80 dilute adsorption free energies $\Delta\mu^{\sigma/w,0}$ in descending order of -22.0, -27.3, -41.9, and -50.3 kBT using the Rossi et al., Lee et al., GROMOS (inward pulling), and GROMOS (outward pulling) PMFs, respectively.

2.11.4 Crowding at interface: conformational changes, interfacial pressure, and surface chemical potential

At low surface coverage, we observe tight binding of the PEG-containing headgroup to the interface between oil and water (see Figure 2-7). The bound PEG chains tend to orient their oxygen atoms toward the aqueous phase (data not shown), in qualitative agreement with spectroscopy by Kim et al.[42] As the interface becomes more crowded, the water/oil interface becomes fully occupied, and headgroups are pushed away from the interface. At the same time, lateral pressure increases, which reduces surface tension.

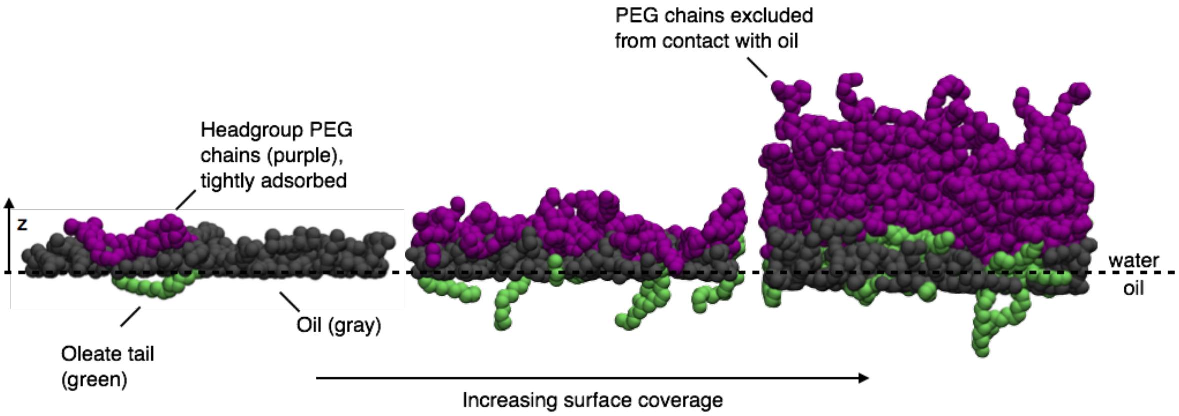

Figure 2-7. When Tween 80 adsorbs at a bare interface (left), PEG binds to the water/oil interface. As the interface becomes saturated (right), the headgroups are displaced into the water. Atomistic (GROMOS 53a6OXY+D) simulation is pictured, oil molecules below the interfacial region are not pictured, and water is not shown, for clarity.

Figure 2-8a plots pressure-area data (black diamonds) and the interpolated pressure-area isotherm (solid line) against the interfacial area per Tween molecule. Alongside this data we plot intramolecular density contours. The number densities of headgroup and tail atoms are mapped in cylindrical coordinates relative to a centroid atom - the ester carbon in this case. Figure 2-8b plots the marginal pressure-area work (MEPAW) calculated from the pressure-area isotherm in Figure 2-8a.

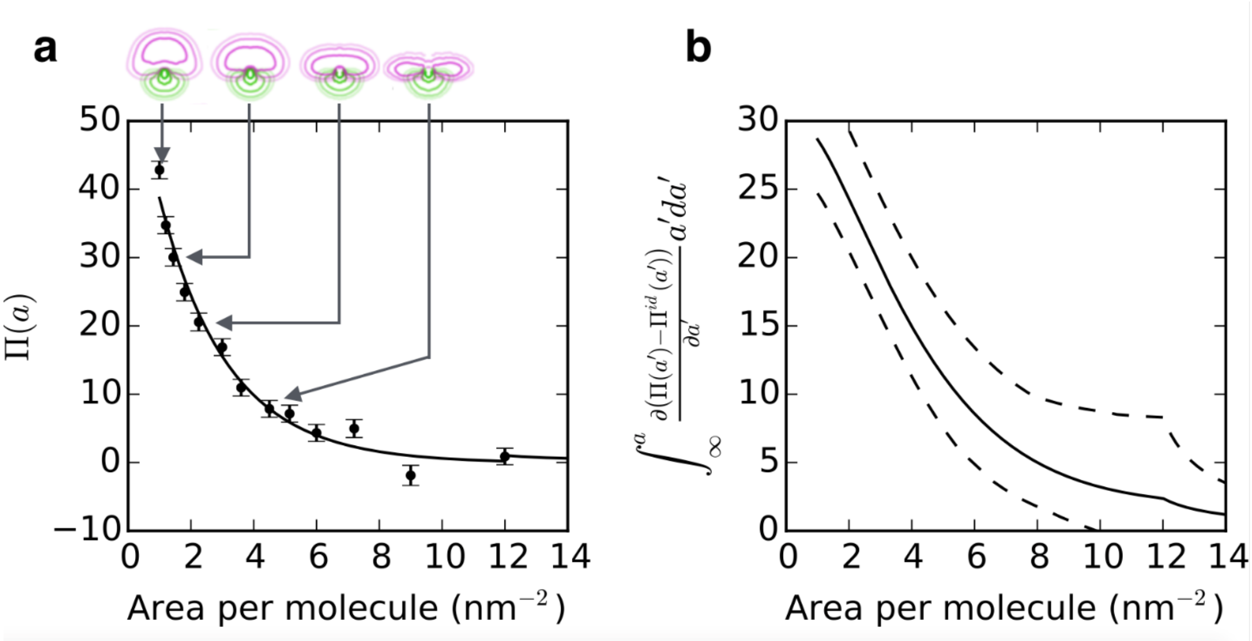

Figure 2-8a. Pressure-area data (black diamonds) and interpolated pressure-area isotherm (black line) alongside intramolecular density contour plots (purple: headgroup density contours, green: tail density contours) in cylindrical coordinates with the z-axis pointed up (view is parallel to interface). 2-8b. MEPAW computed using the integral in Eqns. 2 and 6 and the pressure-area isotherm in 7a. Dashed lines mark the 95% confidence interval.

We note that the isotherm in Figure 2-8a corresponds to a 2D interaction potential much softer than the 2D van der Waals equation; SPEs with bulky headgroups at a crowded interface do not behave like hard disks in general.

2.11.5 Transition from irreversible to reversible adsorption

Using the simulated tensiometry technique described in Methods, we plotted interfacial tension versus time in Figure 2-9 using the weaker of the dilute adsorption free energies for GROMOS 53a6OXY+D Tween 80 ($-42\ k_BT$). If we instead used $-50\ k_BT$, adsorption appeared irreversible through the entire 1-hour duration. Bulk concentration $c_s^{w,\mathrm{bulk}}$ is initially set to 0.5 µM at time zero, and it is switched back to 0 µM at various times for rinsing, to mimic the experiment of Reichert and Walker.[7] Rinsing starts at the points where the interfacial tension profile departs from the adsorption curve. At high interfacial tensions, rinsing causes the tension profile to flatten (irreversible adsorption), whereas it rises (reversible adsorption) at lower tension.

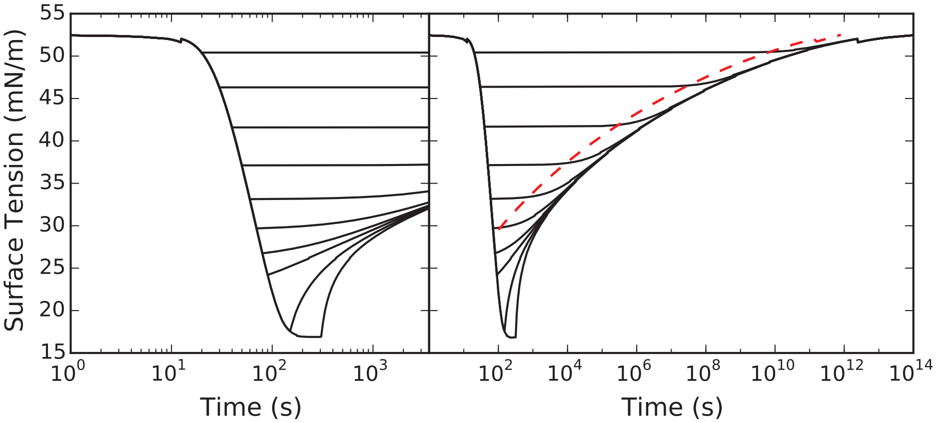

Figure 2-9. Interfacial tension versus time with bulk concentration $c_s^{w,bulk}$ set to 0.5 μM at time zero, and switched back to 0 μM at various times for rinsing. The dashed line shows the time $\tau = 0.01\frac{h_p\delta}{D}$ for 1% desorption at a fixed rate of diffusion-controlled desorption.

During diffusion-controlled rinsing, the bulk concentration $c_s^{w,\text{bulk}}$ is zero, and the sub-surface concentration $c_s^{w,\text{surface}}$ is a one-to-one function of the interfacial tension γ due to local equilibrium with the interface. The transport model also assumes a pseudo-steady thin-film concentration profile, which is valid if the equilibrium depletion depth is much larger than the concentration boundary layer. In this case, the desorption rate is also a one-to-one function of γ. So at a given γ in rinsing, we have a desorption rate which we can write in terms of $c_s^{w,\text{surface}}$ or the planar depletion depth $h_p = \Gamma_s / c_s^{w,\text{surface}}$.

$$\frac{\partial \Gamma_s}{\partial t} = -D\frac{c_s^{w,\text{surface}}}{\delta} = -D\frac{\Gamma_s}{h_p\delta} \tag{13}$$

We are interested in the time required to perceive desorption. Though the choice is somewhat arbitrary, we assume that a 1% removal of adsorbed surfactant is roughly the minimum amount of desorption that can be percieved. So we seek the time τ required at a fixed desorption rate $-\frac{\partial \Gamma_s}{\partial t}$ to remove 1% of the adsorbed surfactant.

$$-\frac{\partial \Gamma_s}{\partial t}\tau = 0.01\,\Gamma_s \tag{14}$$

Eqns. 13 and 14 yield a characteristic time required to perceive desorption in diffusion-controlled rinsing, $\tau = 0.01\frac{h_p\delta}{D}$. As expected, when τ is plotted as a dashed line along the range of interfacial tensions in Figure 2-9, it marks the time at which surface tension bends away from an apparently constant value. We can also see that the "critical surface tension" separating irreversible and reversible adsorption first appears where the dashed line intersects the initial adsorption curve.

Comparison reveals that our simulated tension falls off more quickly (by a factor of 10 or so) than Reichert and Walker observed. This could be due to a kinetic barrier to adsorption as the interface fills up with surfactant. Our model assumes instantaneous equilibrium at the interface, so it has no kinetic barriers to adsorption or desorption. Another prominent difference is that our model transitions from irreversible to fully-reversible adsorption; we have no partially-reversible adsorption. In other words, when our surface tension recovers upon rinsing, it does not stop short of the critical value as observed by Reichert and Walker. Importantly, our model is based on a single representative component of Tween 80, whereas Tween 80 is really a complex mixture of surfactant components, with varying dilute adsorption free energies. In experiments with real Tween 80, the interface may become enriched with stronger-adsorbing components over time that desorb more slowly, causing adsorption during the experiment to be only partially reversible.

2.12 Conclusion

Our simulations show conformational changes as surface coverage of sorbitan polyethoxylates (SPEs) increases; the ethoxylated heads bind tightly to the hydrophobic interface at low surface coverage, but as the interface becomes crowded, the head groups are displaced away from the interface and into the water. The binding of PEG head groups is driven by a binding free energy of around 1.3 $k_B T$ per EO monomer for the atomistic GROMOS 53a6OXY+D forcefield, and less than half of this for the MARTINI CG forcefield of Lee et al. We can rule out the Rossi et al. forcefield for simulation of PEG-containing molecules at hydrophobic interfaces, because it predicts vanishing adsorption for PEG/PEO oligomers of increasing length, contrary to experimental observations. We found that GROMOS 53a6OXY+D gives a dilute adsorption free energy difference between $C_{12}E_8$ and $C_{12}E_2$ of -7.5 ± 0.7 kBT (95% C.I.), in good agreement with the 7.8 kBT from Mulqueen and Blankschtein. For the MARTINI forcefield of Lee et al., we found only a 1.5 ± 0.3 kBT change or 0.27 ± 0.05 kBT per monomer. Both MARTINI forcefields dramatically underestimate the affinity of PEG/PEO for clean hydrophobic surfaces. Hydrogen bonding between adsorbed PEG and water seems to play a role in its surface activity, given hydrophobic orientation observed in our simulations (data not shown) and measured by spectroscopy.[42] Because water in the MARTINI model is an isotropic Lennard-Jones particle incapable of hydrogen bonding, the physics driving MARTINI PEG/PEO to adsorb is very different. It would be of interest to modelers to know whether MARTINI PEG/PEO can be tuned for correct adsorption at hydrophobic interfaces.

Based on the GROMOS 53a6OXY+D Tween 80 PMFs and pressure/area isotherm, a simple thin-film transport model showed the transition from irreversible to reversible adsorption as observed by Reichert and Walker in tensiometry experiments. In the model, however, the recovered surface tension upon rinsing did not have the variability of experiment. This may be due to enrichment of the interface with strongly-adsorbing components of the complex Tween 80 mixture. The modeled rate of adsorption was also too fast, which suggests may be missing a kinetic barrier to adsorption as the interface loads with surfactant.

Although the irreversible-to-reversible transition is simple in nature, we are not aware of this explanation being given previously. In continuous-flow tensiometry by Svitova, Wetherbee, and Radke, a similar phenomenon was observed in ethoxy nonylphenol (NP9) and was attributed to presence of insoluble components in NP9. However, the sub-surface concentration is not necessarily limited by the solubility of the adsorbed components, but could be limited by a large adsorption coefficient. We have shown here that molecular variability is not required for partial irreversibility of adsorption.

The method we used can be generalized to multiple surfactants. For c surfactant components, the PMF must be measured for each component, and the c-dimensional pressure-area-composition isotherm $\Pi(a, x_1, \dots, x_{c-1})$ must be known. The computational expense of mapping Π would grow exponentially with c, limiting the technique to a small number of surfactant components. But even limited to a few surfactant components, future work may explore the influence of molecular variability on bulk-interface equilibrium and dynamic sorption.

2.13 Acknowledgements

This research was made possible in part by a grant from BP/The Gulf of Mexico Research Initiative. For atomistic simulation, we used the Extreme Science and Engineering Discovery Environment (XSEDE), which is supported by National Science Foundation grant number ACI-1053575. Additional simulations were supported through computational resources and services provided by Advanced Research Computing at the University of Michigan, Ann Arbor. We thank Lynn Walker, Shelley Anna, and Stephanie Kirby for helpful discussion of their microtensiometer and tensiometry data. We also thank Vishnu Shresht and Daniel Blankschtein for encouraging conversation on the Nikas-Mulqueen-Blankschtein theory.

2.14 References

(1) National Research Council. *Oil Spill Dispersants: Efficacy and Effects*; The National Academies Press, 2005.

(2) Pilpel, N.; Rabbani, M. E. Formation of Liquid Crystals in Sunflower Oil in Water Emulsions. *J. Colloid Interface Sci.* **1987**, *119* (2), 550–558.

(3) Boyd, J.; Parkinson, C.; Sherman, P. Factors Affecting Emulsion Stability, and the HLB Concept. *J. Colloid Interface Sci.* **1972**, *41* (2), 359–370.

(4) Brochu, C.; Pelletier, E.; Caron, G.; Desnoyers, J. E. Dispersion of Crude Oil in Seawater: The Role of Synthetic Surfactants. *Oil Chem. Pollut.* **1986**, *3* (4), 257–279.

(5) Riehm, D. A.; McCormick, A. V. The Role of Dispersants' Dynamic Interfacial Tension in Effective Crude Oil Spill Dispersion. *Mar. Pollut. Bull.* **2014**, *84* (1–2), 155–163.

(6) Anna, S. L.; Mayer, H. C. Microscale Tipstreaming in a Microfluidic Flow Focusing Device. *Phys. Fluids 1994-Present* **2006**, *18* (12), 121512.

(7) Reichert, M. D.; Walker, L. M. Interfacial Tension Dynamics, Interfacial Mechanics, and Response to Rapid Dilution of Bulk Surfactant of a Model Oil–Water-Dispersant System. *Langmuir* **2013**, *29* (6), 1857–1867.

(8) Ayorinde, F. O.; Gelain, S. V.; Johnson, J. H.; Wan, L. W. Analysis of Some Commercial Polysorbate Formulations Using Matrix-Assisted Laser Desorption/ionization Time-of-Flight Mass Spectrometry. *Rapid Commun. Mass Spectrom.* **2000**, *14* (22), 2116–2124.

(9) Farkas, L.; Morgós, J.; Sallay, P.; Rusznák, I.; Bartha, B.; Veress, G. Determination of Molar Mass Distribution of Alkyl Polyethylene Glycol Ethers. *J. Am. Oil Chem. Soc.* **1981**, *58* (5), 650–655.

(10) Johnson Jr., A. E.; Geissler, P. R.; Talley, L. D. Determination of Relative Ethoxylation Rate Constants from Supercritical Fluid Chromatographic Analysis of Ethoxylated Alcohols. *J. Am. Oil Chem. Soc.* **1990**, *67* (2), 123–131.

(11) Fuchs, P. F. J.; Hansen, H. S.; Hünenberger, P. H.; Horta, B. A. C. A GROMOS Parameter Set for Vicinal Diether Functions: Properties of Polyethyleneoxide and Polyethyleneglycol. *J. Chem. Theory Comput.* **2012**, *8* (10), 3943–3963.

(12) Lee, H.; de Vries, A. H.; Marrink, S.-J.; Pastor, R. W. A Coarse-Grained Model for Polyethylene Oxide and Polyethylene Glycol: Conformation and Hydrodynamics. *J. Phys. Chem. B* **2009**, *113* (40), 13186–13194.

(13) Rossi, G.; Fuchs, P. F. J.; Barnoud, J.; Monticelli, L. A Coarse-Grained MARTINI Model of Polyethylene Glycol and of Polyoxyethylene Alkyl Ether Surfactants. *J. Phys. Chem. B* **2012**, *116* (49), 14353–14362.

(14) Tang, X.; Huston, K. J.; Larson, R. G. Molecular Dynamics Simulations of Structure–Property Relationships of Tween 80 Surfactants in Water and at Interfaces. *J. Phys. Chem. B* **2014**, *118* (45), 12907–12918.

(15) Lee, H.; Venable, R. M.; MacKerell Jr., A. D.; Pastor, R. W. Molecular Dynamics Studies of Polyethylene Oxide and Polyethylene Glycol: Hydrodynamic Radius and Shape Anisotropy. *Biophys. J.* **2008**, *95* (4), 1590–1599.

(16) Israelachvili, J. The Different Faces of Poly(ethylene Glycol). *Proc. Natl. Acad. Sci.* **1997**, *94* (16), 8378–8379.

(17) Won, Y.-Y.; Davis, H. T.; Bates, F. S.; Agamalian, M.; Wignall, G. D. Segment Distribution of the Micellar Brushes of Poly(ethylene Oxide) via Small-Angle Neutron Scattering. *J. Phys. Chem. B* **2000**, *104* (30), 7134–7143.

(18) Skaug, M. J.; Mabry, J. N.; Schwartz, D. K. Single-Molecule Tracking of Polymer Surface Diffusion. *J. Am. Chem. Soc.* **2014**, *136* (4), 1327–1332.

(19) Duncan, S. L.; Larson, R. G. Comparing Experimental and Simulated Pressure-Area Isotherms for DPPC. *Biophys. J.* **2008**, *94* (8), 2965–2986.

(20) Adhangale, P. S.; Gaver, D. P. Equation of State for a Coarse-Grained DPPC Monolayer at the Air/water Interface. *Mol. Phys.* **2006**, *104* (19), 3011–3019.

(21) Klauda, J. B.; Wu, X.; Pastor, R. W.; Brooks, B. R. Long-Range Lennard-Jones and Electrostatic Interactions in Interfaces: Application of the Isotropic Periodic Sum Method. *J. Phys. Chem. B* **2007**, *111* (17), 4393–4400.

(22) Kaznessis, Y. N.; Kim, S.; Larson, R. G. Simulations of Zwitterionic and Anionic Phospholipid Monolayers. *Biophys. J.* **2002**, *82* (4), 1731–1742.

(23) Howes, A. J.; Radke, C. J. Monte Carlo Simulations of Lennard-Jones Nonionic Surfactant Adsorption at the Liquid/Vapor Interface. *Langmuir* **2007**, *23* (4), 1835–1844.

(24) Howes, A. J.; Radke, C. J. Monte Carlo Simulation of Mixed Lennard-Jones Nonionic Surfactant Adsorption at the Liquid/Vapor Interface. *Langmuir* **2007**, *23* (23), 11580–11586.

(25) Wang, S.; Larson, R. G. Coarse-Grained Molecular Dynamics Simulation of Self-Assembly and Surface Adsorption of Ionic Surfactants Using an Implicit Water Model. *Langmuir* **2015**, *31* (4), 1262–1271.

(26) Amani, A.; York, P.; Waard, H. de; Anwar, J. Molecular Dynamics Simulation of a Polysorbate 80 Micelle in Water. *Soft Matter* **2011**, *7* (6), 2900–2908.

(27) Schäfer, L. V.; Jong, D. H. de; Holt, A.; Rzepiela, A. J.; Vries, A. H. de; Poolman, B.; Killian, J. A.; Marrink, S. J. Lipid Packing Drives the Segregation of Transmembrane Helices into Disordered
Lipid Domains in Model Membranes. *Proc. Natl. Acad. Sci.* **2011**, *108* (4), 1343–1348.

(28) Berendsen, H. J. C.; Postma, J. P. M.; van Gunsteren, W. F.; DiNola, A.; Haak, J. R. Molecular Dynamics with Coupling to an External Bath. *J. Chem. Phys.* **1984**, *81* (8), 3684–3690.

(29) Parrinello, M.; Rahman, A. Polymorphic Transitions in Single Crystals: A New Molecular Dynamics Method. *J. Appl. Phys.* **1981**, *52* (12), 7182–7190.

(30) Bussi, G.; Donadio, D.; Parrinello, M. Canonical Sampling through Velocity Rescaling. *J. Chem.Phys.* **2007**, *126* (1), 014101.

(31) Kumar, S.; Rosenberg, J. M.; Bouzida, D.; Swendsen, R. H.; Kollman, P. A. The Weighted Histogram Analysis Method for Free-Energy Calculations on Biomolecules. I. The Method. *J. Comput. Chem.* **1992**, *13* (8), 1011–1021.

(32) Grossfield, A. *WHAM: The Weighted Histogram Analysis Method*, version 2.0.9; http://membrane.urmc.rochester.edu/content/wham (accessed August 2014).

(33) Nikas, Y. J.; Puvvada, S.; Blankschtein, D. Surface Tensions of Aqueous Nonionic Surfactant Mixtures. *Langmuir* **1992**, *8* (11), 2680–2689.

(34) Mulqueen, M.; Blankschtein, D. Theoretical and Experimental Investigation of the Equilibrium Oil−Water Interfacial Tensions of Solutions Containing Surfactant Mixtures. *Langmuir* **2002**, *18* (2), 365–376.

(35) Frenkel, D.; Smit, B. *Understanding Molecular Simulation: From Algorithms to Applications*; Academic Press, 2001.

(36) Alvarez, N. J.; Vogus, D. R.; Walker, L. M.; Anna, S. L. Using Bulk Convection in a

Microtensiometer to Approach Kinetic-Limited Surfactant Dynamics at Fluid–fluid Interfaces. *J. Colloid Interface Sci.* **2012**, *372* (W), 183–191.

(37) Levich, V. G. *Physicochemical Hydrodynamics;* Prentice-Hall: Englewood Cliffs, N.J., 1962.

(38) Kirby, S. M.; Anna, S. L.; Walker, L. M. Sequential Adsorption of an Irreversibly Adsorbed Nonionic Surfactant and an Anionic Surfactant at an Oil/Aqueous Interface. *Langmuir* **2015**, *31*
(14), 4063–4071.

(39) Pronk, S.; Páll, S.; Schulz, R.; Larsson, P.; Bjelkmar, P.; Apostolov, R.; Shirts, M. R.; Smith, J. C.; Kasson, P. M.; Spoel, D. van der; et al. GROMACS 4.5: A High-Throughput and Highly Parallel Open Source Molecular Simulation Toolkit. *Bioinformatics* **2013**, 29 (7), 845-854.

(40) Michaud-Agrawal, N.; Denning, E. J.; Woolf, T. B.; Beckstein, O. MDAnalysis: A Toolkit for the Analysis of Molecular Dynamics Simulations. *J. Comput. Chem.* **2011**, *32* (10), 2319–2327.

(41) Velinova, M.; Sengupta, D.; Tadjer, A. V.; Marrink, S.-J. Sphere-to-Rod Transitions of Nonionic Surfactant Micelles in Aqueous Solution Modeled by Molecular Dynamics Simulations. *Langmuir* **2011**, *27* (23), 14071–14077.

(42) Kim, J.; Opdahl, A.; Chou, K. C.; Somorjai, G. A. Hydrophobic-Interaction-Induced Alignment of Polymers at the Solid/Liquid Interface Studied by Infrared−Visible Sum Frequency Generation. *Langmuir* **2003**, *19* (23), 9551–9553.

CHAPTER 3

Search for the sources of an apparent interfacial resistance to mass transfer of CnEm surfactants to the water/oil interface

3.1 Introduction

Resistance to surfactant adsorption and relaxation of surface tension influences the wetting of pesticide sprays[1], spreading and penetration of inks[2], paint leveling, and stability of pharmaceutical emulsions and foams.[3] Kinetic rates of surfactant adsorption and desorption influence surface viscosity, and surfactants in high concentration can reduce surface elasticity if they are available to immediately fill openings in dilated films.[4] Adsorption dynamics of surfactants and rheology modifiers can also control viscoelasticity of latexes and other particle suspensions.[5]

Dynamic adsorption is often studied by exposing a freshly formed interface to dissolved surfactants. When a fresh interface forms between two solutions, assuming no residual surfactant carries over from a parent interface, the initial composition of the interface matches the bulk fluid composition. The solvent itself undergoes a surface tension relaxation – for example, the surface of water takes 10-4 to 10-3 seconds to relax.[6] This relaxation may involve, for example, the formation of a double layer of hydroxide and hydronium through migration and autolysis.[7,8] Surfactant has its own timescale for surface relaxation – it must diffuse to the surface and in some cases overcome an energetic barrier before adsorbing, particularly for ionic surfactants whose charge builds an electric potential at the surface as it adsorbs. Fewer non-ionic surfactants have exhibited apparent interfacial resistance to adsorb in excess of the diffusive resistance, and for them the existence of the interfacial resistance has been more controversial; examples include linear alcohols at a water/air surface[9–11] and alkyl ethoxylates at a water/air surface.[12–16] Felodipine, a non-ionic drug, has been reported to exhibit resistance to adsorption during the surface integration step of crystal growth.[17] We focus in this work on two studies of alkyl ethoxylates, one at a water/silicone oil interface[18] and the other at a water/mineral oil interface.[19]

3.1.1 Surfactant adsorption modeling fundamentals

Adsorption of surfactants is usually modeled by dividing transport into three spatial zones: (1) bulk fluid, which is the initial reservoir of surfactant bounded by (2) the subsurface with surfactant concentration c_s, which is a thin layer of fluid (a few surfactant molecular widths thick) in contact with (3) the surface or interface where the surfactant builds a monolayer of surface concentration Γ.[20–22] In cases where there is a mass transfer boundary layer, the bulk fluid contains a sub-zone of varying concentration, from the imposed far-field concentration to that in the subsurface. In diffusion-controlled adsorption, the subsurface is in equilibrium with the surface, whereas in kinetically-limited adsorption, there is an adsorption rate equation for surfactant transfer between surface and subsurface. For ionic surfactants, the electric potential barrier may be accounted for as a drift force in the diffusion model coupled with the Poisson equation.[23] For non-ionic surfactants, to our knowledge the only approach to modeling kinetics is fitting constants in an adsorption rate equation to experimental measurements of surface tension versus time after exposure to surfactant. Such fits give apparent adsorption and desorption rate constants, and therefore are taken as measurements of interfacial resistance to mass transfer, but give no molecular explanation for the magnitudes of such resistances. Here we seek a more detailed source of these apparent resistances, using molecular dynamics simulations, the Weighted Histogram Analysis Method (WHAM) to obtain potentials of mean force, and the Smoluchowski diffusion equation to analyze the adsorption rate constant.

For the alkyl ethoxylates we study here, we consider the rate process of surfactant transfer from subsurface to surface to be a non-inertial diffusive process, with memoryless drift arising from the interfacial potential of mean force on the distance between the surfactant's center of mass position z and the interface. No slow variable needs to be considered for this process besides z. Our evidence that z is a sufficient collective variable is the absence of hysteresis between potentials of mean force measured using WHAM after pulling the simulated surfactant in both directions to arrive at the sampled states. If there were another slow variable, we would expect to see hysteresis between the two results. In addition, we validated the interfacial potential of mean force for description of the adsorption kinetics by running direct simulations of spontaneous adsorptions. This procedure is described more in the Results and Discussion section.

For non-ionic surfactants that form an interfacial monolayer, equilibrium deviations from the bulk composition are only evident at proximities to the interface of at most a few molecular widths. This narrow region is taken to be a geometric surface in adsorption rate equations. In the Supporting Information (SI), we connect the desorption and adsorption rate coefficients k_{des} and k_{ads} from the adsorption rate equation to the free energy profile and diffusivity profile of the surfactant around the interface. In brief, we calculate the mean first passage time for surfactant escape from the interfacial potential well and the stationary drift velocity of surfactant into an adsorbing sink at the bottom of the potential well. The first-passage time calculation of k_{des} has been performed before for surfactants,[5,24] but we believe the calculation of k_{ads} is novel in surfactant applications and described for the first time here.

Assuming no reaction of free monomers, i.e. no formation of aggregate or micellar components, the rate of accumulation of surfactant in the interfacial monolayer is given by:

$$r = \frac{\partial \Gamma}{\partial t} = k_{\mathrm{ads}}(\Gamma) c_s - k_{\mathrm{des}}(\Gamma)\Gamma \qquad (1)$$

The net rate of adsorption is the difference between the rates of adsorption and of desorption, where the adsorption rate is given by the product of the subsurface concentration c_s and a Γ-dependent adsorption rate coefficient k_{ads}, and desorption is given by the product of Γ and a Γ-dependent desorption rate coefficient k_{des}.

3.1.2 Adsorption experiments

Many experimental methods have been developed to track time-dependent surface tension relaxation: maximum bubble pressure, oscillating jet, growing drop, inclined plate, drop pressure, drop volume, pendant drop, and plate or ring tensiometry.[1,25,26] Each of these methods has an initial "dead time" associated with the flow needed to create a fresh surface. The longer the startup flow takes to create the surface, the longer the surface will age before accurate measurements can be made. Initial convection can persist for seconds or more before dissipating, so some methods impose a constant, forced convection to eliminate the transient flow and reduce dead time. Such methods include the maximum bubble pressure method and the oscillating jet method which have dead times of around a millisecond.[1] The common pendant drop/bubble methods have dead times of [2-4] seconds.[1]

Researchers have studied dynamic adsorption of alkyl ethoxylate surfactants to the air/water surface and come to contradictory conclusions. Eastoe et al. (1997) inferred an adsorption barrier in addition to the diffusive barrier for $C_{12}E_5$ and numerous other C_iE_j surfactants to the air/water surface.[12] However, they performed their analysis with asymptotic solutions that have been widely used, but whose validity has been called into question.[27] Other researchers avoided the asymptotic solutions. For example, Lin, et al. (1996) used Langmuir, Frumkin, and generalized Frumkin equations of state and a Ward-Tordai equation scaled to account for an energy barrier to conclude that adsorption of $C_{12}E_8$ to the air/water surface was not diffusion-controlled adsorption (DCA) but had another kinetic interfacial resistance limiting adsorption.[13] However, they also reported unusually high diffusion coefficients. Miller, Aksenenko, and Fainerman (2017) concluded that $C_{14}E_8$ adsorption to the water-air surface is consistent with DCA when they employed their 5-parameter reorientation-with-compressibility model.[16] Mulqueen, Stebe, and Blankschtein (2001) concluded that adsorption of $C_{12}E_5$ and $C_{10}E_8$ from water onto the air/water surface was consistent with DCA for the range of concentrations they studied.[14] These researchers except Eastoe et al. used a pendant bubble experimental setup and solved the Ward-Tordai equation (either planar or with spherical correction) for adsorption from a semi-infinite medium of uniform initial concentration. Most convincingly, Alvarez, Walker, and Anna showed using a microtensiometer that their model fits of adsorption data followed expected scaling laws to make the case for DCA of $C_{12}E_8$ to the air/water surface.[15] Thus, the weight of evidence points toward no non-diffusional interfacial resistance for $C_{12}E_8$ adsorption to the air/water surface. On the other hand, the same group, namely Alvarez et al., found a distinct interfacial resistance to mass transfer to the oil/water interface.

As alluded to above, Alvarez, Lee, Walker, and Anna (2011) used a pendant droplet setup to model the silicone oil/water interface.[18] By fitting the tension response with the generalized Frumkin rate equation, they did not detect an interfacial resistance for $C_{10}E_8$, i.e. the diffusive resistance alone explained the response, but they did detect an apparent interfacial resistance for $C_{12}E_8$ and an even larger resistance for $C_{14}E_8$ adsorption to the silicone oil/water interface. Guo

(2012) reported an interfacial resistance for $C_{12}E_8$ adsorption to the mineral oil/water interface using the same apparatus.[19] The molecular origin of this resistance has not been explained and is the main focus of the present work.

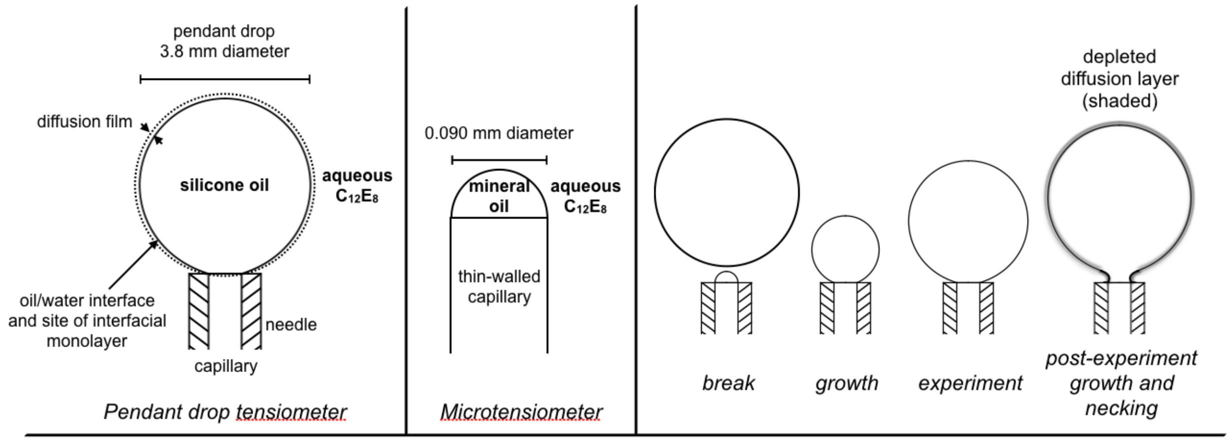

Figure 3-1: At left is a schematic of an oil droplet growing from a capillary sheathed within a needle, as in the pendant drop tensiometer described in Alvarez et al.[18] At center is a schematic of a hemispherical oil droplet protruding from the tip of a thin-walled capillary as described by Guo.[19] At right are steps for preparing a new pendant drop experiment after ejecting an old drop. In the first step, a fluid neck has broken and a drop is ejected while a small amount of fluid remains and grows as it is supplied by the capillary. Flow stops when the droplet reaches a target radius, and the experiment begins. After the experiment, the saturated droplet needs to be ejected. Fluid is pumped into the droplet, and the growing interface is unsaturated once again.

3.1.3 Detailed experimental description

This study focuses on data generated by Alvarez et al. [18] and of Guo.[18,19] Alvarez et al. used a pendant drop tensiometer to measure dynamic surface tension (DST) for $C_{12}E_8$ adsorbing to the water/silicone oil interface.[18,28] Guo used a microtensiometer to measure DST for $C_{12}E_8$ adsorbing to a water/mineral oil interface.[15,19] Schematics of each apparatus appear in Figure 3-1. The silicone oil had an interfacial tension with water of 40 mN/m, and the mineral oil had an interfacial tension with water of 52 mN/m. During each experiment, the fluid is quiescent, and surfactant diffuses from aqueous solution onto the surface of the oil drop. The "diffusion layer," which is the surfactant-denuded zone bounding the interface, grows in thickness as the surfactant that it originally contained is lost to the interface, until the interface is nearly saturated with adsorbed molecules (see Figure 3-2). The thickness of the diffusion film is thus time-dependent and also depends on the surfactant concentration. A lower surfactant concentration in solution will require the diffusion film to grow farther into solution as the interface fills itself. As the interface fills with surfactant, the interfacial tension drops and is recorded over time. Resulting data appears in Figure 3-2.

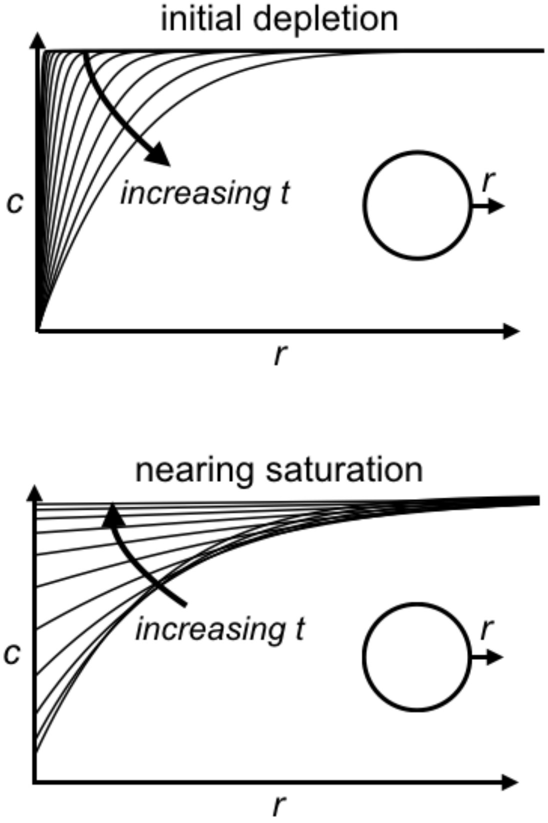

Figure 3-2: Illustrations of the concentration profiles in solution; (top): in the initial stage of adsorption, when the solution is depleted of surfactant, and (bottom): in the latter stage of adsorption, as the interface nears saturation, and the depleted film stops growing and surfactant from the bulk diffuses into it.

In the work of Alvarez et al., to grow the oil drop before experiments, the silicone oil flowed into a pendant drop through a capillary with inner diameter of 0.76 cm, sheathed in a 1.65 mm-diameter J-shaped needle, and the oil flow rate was kept below 850 μL/min to minimize unwanted convection. When the droplet reached a radius of 1.9 mm, the experiment began, and a camera recorded the backlit droplet's shape over time. This video could later be analyzed to measure surface tension over time. Alvarez et al. also reported a density and viscosity for silicone oil of 0.960 g/cm^3 and 48 cP.

In the work of Guo, the microtensiometer device had a capillary of inner diameter 0.090 mm, resulting in an especially small Bond number and a nearly spherical droplet with a radius close to that of the capillary. In contrast to the classic pendant droplet shape shown at left in Figure 3-1, the microtensiometer droplet resembles a hemispherical cap protruding from the capillary. Guo used NF-grade light mineral oil, which has a density between 0.818 and 0.880 g/cm^3 and can have a kinematic viscosity between 0.030 and 0.344 cm^2/s.[29]

In each case, the DST exhibited an apparent interfacial resistance to mass transfer of the surfactant to the interface, due to discrepancy with the predictions of diffusion-controlled transfer using an adsorption isotherm fitted to equilibrium data. Besides $C_{12}E_8$, Alvarez et al. also reported the DST for $C_{10}E_8$ and $C_{14}E_8$ in the same paper and showed that while $C_{14}E_8$ also showed an apparent interfacial energy barrier, $C_{10}E_8$ did not.

A pendant droplet experiment begins either by growing a new droplet from an interface on the capillary tip long after any previous droplet had been ejected, or by growing the new droplet as a previous droplet, already saturated with surfactant, is ejected. In the setup of Alvarez et al., the inflation of an interface from the cross-sectional area of the capillary to the interfacial area of the fully formed pendant drop involves a 25-fold increase in interfacial area. The alternative is to grow the new droplet immediately after ejecting an older droplet. We now consider this initial droplet formation process in more detail.

Before starting a new experiment, a pendant drop from a previous experiment might be ejected, which requires flow from the capillary to provide mass and/or momentum. Necking occurs when buoyant and inertial forces become stronger than the surface tension at the capillary tip, and the droplet pulls away from the capillary. The pendant drop divides into the ejected drop and a nascent, residual drop. Presumably some surfactant is left behind on the residual drop, but following the pendant drop breakup analysis of Scheele and Meister, and using the material and equipment properties described by Alvarez et al., we estimate the ejected drop surface area to be 0.068 cm^3, and that only around 1% of the drop volume is left behind.[30] A correlation by Humphrey gives an estimate of 0.048 cm^3 for the ejected droplet volume without providing an estimate for the residual droplet size.[31] The pendant drop radius is 1.9 mm, giving a volume of 0.029 cm^3. If we take these estimates at face value, the number of surfactant molecules per unit area could drop to between 50% and 75% of the experimental value before the droplet breaks away. This creation of new surface area on the ejected droplet could potentially scavenge surfactant from the surrounding fluid which might deplete its local concentration, thereby influencing the following experiment on the new pendant drop. The term diffusion layer, referred to above, is generally used to describe the layer of solution in which component concentrations are altered from their values in bulk solution by the presence of the interface.[21,32]

The post-experimental depletion of the used droplet's diffusion layer is only a concern if this diffusion layer ends up forming part of the new droplet's diffusion layer. These diffusion layers are thin, however. For reference, the depletion length of $C_{12}E_8$ at high concentration is around 0.02 mm. That is, 0.02 mm of fluid would have to be depleted of surfactant to fill up the interface. The characteristic length scale for 2 seconds of $C_{12}E_8$ diffusion in water is about 0.04 mm. The depleted diffusion layer around the neck and on the residual droplet attached to the capillary would be thinned significantly by convection when the droplet grows to its full experimental size. A 25x increase in surface area should be accompanied by a 25x thinning of the depleted layer, which would likely make it unnoticeable. To see significant effects from the depleted layer, the large depleted area around the ejected droplet would have to be transported somehow to the surface of the new droplet. Would the depletion layer roll off the ejected droplet and be left behind to interact with the growing new droplet? A liquid/liquid interface like silicone oil/water or mineral oil/water would normally be mobile, and as the ejected droplet rises, its interface would be pulled by viscous drag from the surrounding water toward the end closest to the capillary, which would help to shed the depleted layer onto the new droplet. However, the ejected droplet's surfactant coating would exert Marangoni stress to resist the buoyant flow-driven concentration of adsorbed surfactant at the end of the droplet nearest the capillary, which would make the surface act more rigid. If the depleted layer nonetheless transfers to the new droplet, an explanation would also be needed for why this appears to have an effect only on the oil-in-water experiments and not on the air-in-water experiment. One possibility is that the air/water density difference is much larger than the silicone oil/water density difference and the mineral oil/water density. The larger density difference implies a greater buoyant force and perhaps smaller time available for transfer of the depleted layer to the new droplet. We note that after the creation of such a depletion layer, the nascent droplet would need about 2 seconds to grow to full size, and during this time the depletion layer could be replenished by adjacent layers of un-depleted surfactant. It is unclear how this would affect any appearance of a resistance to interfacial mass transfer.

In the microtensiometer used by Guo, prior to an experiment, the old hemispherical cap of fluid is ejected by a brief pressure spike. This ejection could also create unsaturated interfacial area which creates a diffusion layer of surfactant for the new, fresh interface, in a similar way to that described above.

The mass transfer leading up to the start of a pendant drop experiment immediately following a drop ejection is complex, and may require detailed modeling of the fluid mechanics and mass transfer to know whether any depletion zone created by the new surface area on the ejected droplet interacts with the surface created on the newly created pendant droplet.

The key assumptions under which the diffusion-adsorption transport model is valid are:

1. The surfactant is a single, pure component, and there are no other surface active species that have a significant effect on interfacial tension that changes over the course of the experiment.
2. There is no micellization.
3. The diffusion is Fickian. This includes all the requisite assumptions for Fick's law, including dilute solution $c_S \ll c_T$, an ideal solution, and equimolar counterdiffusion or constant total molar concentration c_T.
4. The pendant droplet is treated as a sphere, which it nearly is due to the low Bond number.
5. The concentration of surfactant in the external fluid is uniform, especially in the diffusion layer adjacent to the interface of the droplet at the instant it is fully formed.
6. If the experiment is performed immediately after an aged droplet is ejected, then transport to the new droplet is unaffected by the previous ejection process. There is neither convection to accelerate transport, nor depletion of surfactant in the diffusion layer to slow transport.

3.1.4 Possible causes of resistance to adsorption

With the above description of the experiments in view and the assumptions used to model the resulting time dependence of interfacial tension, there are several possible causes for a delay in reducing surface tension beyond that due to diffusion to the interface: (1) surfactant dissolving into the oil phase after having diffused to the interface from the water, (2) an energetic barrier to adsorption from the subphase, (3) slowed diffusion due to surfactant aggregation and micellization at higher concentrations, (4) a mobile-to-rigid interfacial transition that occurs as surfactant accumulates, increasing the boundary layer thickness, (5) a transient concentration non-uniformity near the interface, and (6) coexistence of distinct surface phases with different densities. We consider these potential causes in more detail:

- Cause 1 could explain an apparent resistance at the water/oil interface. Alvarez et al. considered this possibility but ruled it out, arguing the dissolution of surfactant into silicone oil was too slow to produce a significant effect.18 Nonetheless, we will check whether re-dissolution of adsorbed surfactant generates a time-dependent interfacial tension that mimics that produced by an energy barrier.
- Cause 2 seems plausible and is widely accepted for ionic surfactants, which induce an electrostatic potential barrier that surfactants must climb before reaching the stabilizing interface. It is possible that non-ionic surfactant molecules, when crowded onto an interface, induce a steric barrier which is difficult for others to cross. We can examine this possibility with molecular simulation by computing the free energy profile and phenomenological adsorption rate for crowded interfaces. We can also compute the local diffusivity for surfactant molecules within a few nanometers of the interface to check for a decrease of several orders of magnitude, which would be needed to explain a resistance or apparent “barrier” to adsorption.
- Cause 3 might be ruled out, because micellization doesn’t occur when the equilibrium surface tension is still sensitive to bulk surfactant concentration. However, pre-micellar

aggregation could in principle slow the diffusion of surfactant. By measuring surfactant self-associativity and using a conservative estimate for diffusivity of aggregates, we will calculate whether this could be significant.

- Cause 4 is an interesting possibility for continuous-flow tensiometers. For Péclet numbers of 10 and 1000, the ratio of rigid interfacial boundary layer (BL) width to mobile interfacial BL width is 1.6 and 3.5, respectively. This increase in BL width would decrease the characteristic rate of diffusion by 2.6x and 12.3x, respectively. However, in pendant drop experiments by Alvarez et al. described above, there is no continuous flow to interact with any surface tension gradient, so the mobility of the interface doesn't matter. We therefore rule out this cause.
- Cause 5 is invoked by a little-cited theory of dynamic surface tension which considers the effect of depleted surfactant concentration near an adsorbing surface before the equilibrium concentration distribution is achieved.[6,9,10,26,33,34] To the best of our knowledge, the preceding citations are the entirety of the theory's appearance in the literature. The cause is referred to as, for example: "nonuniformity … in a [relaxing] surface zone" 6, "nonequilibrium surface layer" [9,10], "non-equilibrium adsorption layers"26, "nonuniformity of the bulk concentration distribution" [34], and "temporary concentration deficiencies due to diffusional concentration gradients" [1]. Although the mechanism appeared initially promising to explain the apparent energy barriers, we believe it is a fictitious phenomenon predicted by invalid analysis. Briefly, one derivation of the theory invokes surface tension as the interfacial-area derivative of free energy but fails to account for the deformation of the concentration field implied by a non-equilibrium change of interfacial area. The other derivation accounts for mixing as

part of surface-excess free energy but misses the negating contribution from a surface-excess entropy term. We note the theory still allows for concentration nonuniformity to influence dynamic surface tension of ionic surfactants, whose activity coefficient may depend on the distance to the interface, but not for non-ionic surfactants as studied in this paper. The flaw of each derivation is shown in detail in S.5 of the Supporting Information. Thus, we don't believe transient concentration non-uniformity is causing the apparent interfacial resistance.

- Cause 6 implies that at least two distinct surface phases exist – for example, a gaseous state and a liquid state. The liquid state has a greater surface density of surfactants than the average surface density, but the coexisting gaseous state buffers these liquid islands from interacting. This suppresses the increase of the surface pressure until the percolation of the surface gas is overcome by the surface liquid phase. The existence of distinct surface phases is known to occur at the water-air surface, where tail-tail interactions between surfactants are energetically favorable relative to tail-oil interactions.[35] However, it is unlikely the hydrophobic tails lead to surface aggregation in the presence of the hydrophobic solvent, and we have observed no such surface aggregation in molecular simulation. We therefore rule this out for the system we study.

Thus, we immediately rule out Causes 4-6 as implausible sources of apparent interfacial resistance, at least for alkyl ethoxylate adsorption to the water/oil interface under the conditions described.[18,19] Below, we present the methods we use to test the validity of the remaining candidate apparent resistances, from Causes 1-3, and then give the results of these tests. Such validation, in addition to addressing the issue of apparent interfacial resistance, also helps sharpen the focus of molecular simulation and can improve theories of interfacial adsorption.

3.2 Methods

3.2.1 Transport modeling for dynamic surface tension

We used centered finite differences to evaluate the time derivatives of concentration appearing in Fick's second law $\frac{\partial c}{\partial t} = \nabla \cdot (D \nabla c)$. We also evaluated the time derivative of adsorbed surfactant using the generalized Frumkin rate equation:[18]

$$\frac{\partial \Gamma}{\partial t} = \beta c_s \Gamma_{\max}\left(1 - \frac{\Gamma}{\Gamma_{\max}}\right) - \alpha \Gamma \exp\left(\kappa \left(\frac{\Gamma}{\Gamma_{\max}}\right)^n\right) \tag{2}$$

We integrated these equations using explicit Euler time integration with a dynamically adjusted time step. The pendant droplet tensiometer is modeled by a sphere with rotational symmetry. The outer phase (water) began with uniform initial concentration equal to c_{bulk}, and the inner phase (oil) and interface began empty. To model re-dissolution of surfactant into oil after adsorbing from the water, we set the ratio of interface-oil forward/reverse adsorption rate coefficients to match an oil/water partition coefficient of 1.45, and we set the surfactant diffusivity in oil to be 1/48 its diffusivity in water given the 48 cP silicone oil viscosity, matching the viscosities and partition coefficient reported by Alvarez et al.[18] For the diffusion-controlled models discussed below, that are assumed to lack a significant resistance to adsorption, with and without re-dissolution into oil, we continued to use the generalized Frumkin rate equation but increased the model rate coefficients by a factor of 50 relative to the kinetically-limited adsorptions, which was sufficient to reach the diffusion-controlled regime.

3.2.2 Predicting energy barrier height from steady-state diffusion over a model energy landscape

The adsorption rate r (a molar flux) is the product of the rate constant k_{ads} (a speed) and the sub-surface concentration of surfactant cs. The significance of k_{ads} as a speed can be interpreted by considering the free energy profile representing the surfactant's interaction with the interface. For a molecule diffusing over such a free energy profile, the Smoluchowski equation (see section B-2) is a diffusion equation which can be solved to obtain rates of passage. In a pseudo-steady-state approximation, the sub-surface concentration is fixed to a value c_s at one boundary, x=X, and fixed to 0 at the bottom of the adsorption energy well at x=0. The flux of surfactant is taken to be constant along the free energy profile, and to keep it constant, the concentration and speed of surfactant transport along the profile vary inversely. At the sub-surface boundary, where the concentration is cs, the surfactant has a speed k_{ads} under our pseudo-steady-state approximation:

$$v(x) = -\left(\int_0^x \frac{e^{\Phi(x')-\Phi(x)}}{D^{(2)}(x')}dx'\right)^{-1} \tag{3}$$

$$k_{\mathrm{ads}} = |v(X)| \tag{4}$$

Here Φ(x) is the potential landscape in k_BT units as a function of position x, $D^{(2)}(x)$ is the local diffusion coefficient, v(x) is the local drift velocity, X is the position of the fixed-concentration boundary, and 0 is the position of the fast sink. See the Supporting Information (SI) for a detailed derivation of the above starting from the general stationary solution of the one-dimensional Smoluchowski equation.[36] We verified this approach for calculating k_{ads} by dividing it by k_{des} (reciprocal surfactant escape time) and checking that the ratio equals the equilibrium adsorption ratio $(\frac{\Gamma}{c_s})_{eq}$ calculated by integrating the local concentration, normalized by the equilibrium bulk concentration c_s, over x from 0 to X. This is given by Equation 5,

$$\left(\frac{\Gamma}{c_s}\right)_{\mathrm{eq}} = \int_0^X \exp\big(-\Phi(x)\big)\ dx \tag{5}$$

where $\Phi(x)$ is shifted to equal zero in the bulk solution at position X. In principle, one has to subtract the bulk contributions from the concentration profile so that the integrated concentration is the excess over each bulk phase. Rigorous calculation of the thermodynamic surface excess is described elsewhere,[23] but for a nonionic surfactant that forms a dense monolayer with concentration many orders of magnitude greater than the dilute bulk solution, the positioning of the Gibbs dividing surface, the invariant formalism, and the bulk concentrations are negligible to the calculation of (Γcs)eq described above. In the SI, we give a derivation of Equation 5 starting from the Gibbs-invariant surface excess.[37] The calculated quantities k_{ads}/k_{des} and $(\frac{\Gamma}{c_s})_{\mathrm{eq}}$ matched to within 1% for all barrier heights we tested. Once this pseudo-steady-state interface model was verified, we calibrated the barrier height to match the adsorption rate constants fitted by Alvarez et al.[18]

3.2.3 Molecular dynamics calculations

To reveal any barrier in the final nanometers of approach to the interface, we used umbrella sampling and the weighted histogram analysis method (WHAM), as described previously, [38] to compute the potential of mean force near the interface. Briefly, for each interfacial area per molecule studied ($a \in \{0.56, 0.62, 0.73, 2.25, 36.00\}$ nm^2/molecule), we used a set of 66 harmonically biased simulations with a spacing of 1.2 Å separating the minima in the bias potentials and a spring constant of 1500 kJ mol^{-1} nm^{-2} in Gromacs simulations.[39] Simulations were performed in rectilinear boxes with 6 nm by 6 nm interfacial area and at least 18 nm long in the direction normal to the interface. Boxes were filled by equilibrating solvent slabs of water and our model oil, 2-methyl-5-ethylnonane, pairing them next to each other, equilibrating again, inserting surfactants into one of the solvent phases, pulling the surfactants to the interfaces, and equilibrating a final time before a data production run. The interfacial position in every case – for example, in Figure 3-6 – is measured as the distance to the center of the oil slab. Each harmonically biased simulation ran for 20 ns, which we selected to be in excess of the slowest relaxation process we identified for a surfactant in a crowded monolayer, which was ≈ 1 ns, which is the surfactant relaxation time. We measured the surfactant relaxation time by computing the autocorrelation time of the offset of each unrestrained surfactant's center of mass relative to the center of mass of the entire unrestrained monolayer at a surface coverage of 0.62 nm^2/molecule.

WHAM was performed with the Gromacs utility g_wham.[40] The initial configurations for the harmonically biased simulations were generated by pulling the test surfactant molecule out from the interfacial monolayer. We repeated the PMF calculation for the most crowded interface with initial configurations generated by pulling the test molecule back into the monolayer, to check the resulting PMF for hysteresis, i.e. a difference in the calculated PMF depending on the pulling direction. We did not find hysteresis, which indicated there were no other important slow variables which were inadequately sampled, unlike in a previous study we performed on Tween 80.[41] In addition, estimated diffusivities from the harmonically biased simulations by dividing the variance of position by the position autocorrelation time as described by Zhu and Hummer (2012).[42] This calculation is described more below.

We modeled the alkyl ethoxylate $C_{12}E_8$ with the GROMOS 53a6$_{OXY+D}$ forcefield.[43] GROMOS 53a6$_{OXY+D}$ is an additive (fixed partial charge), united-atom forcefield, which has an explicit interaction site for each atom, except for non-polar hydrogen atoms which are united with the atom to which they are attached (carbon). We previously validated this GROMOS 53a6$_{OXY+D}$ for ethoxylate adsorption strength at the water/alkane interface.[41] We adopted the SPC water model as in our previous validation, and for our model oil we used the dodecane isomer, 2-methyl-5-ethylnonane. We picked dodecane despite its low molecular weight relative to the silicone oil used by Alvarez et al. and mineral oil (≈C30) used by Guo, because the low molecular weight led to faster relaxation and more efficient sampling, and we picked a branched isomer to suppress formation of a crystal-like layer that would form between linear n-dodecane solvent and the dodecane tails of the $C_{12}E_8$ surfactant. The stochastic velocity-rescale thermostat maintained a temperature of 300 K, the cross-sectional dimensions of the box were fixed, and the longitudinal component of the pressure was fixed to 1 bar with the Parrinello-Rahman barostat.[44,45]

3.2.4 Calculation of local diffusivity with the method of Zhu and Hummer

Zhu and Hummer (2012) showed how diffusivity of a species can be estimated from that species' position fluctuations under a strong harmonic bias, i.e. where the position distribution is Gaussian.42 In this method, the diffusivity is calculated as $D=(\frac{\delta Q^2}{\tau})$ where τ is the autocorrelation time of position in a biased simulation and $\langle \delta Q^2 \rangle$ is the variance of position. We use this method to estimate the local diffusivity near the interface and look for any position at which the diffusivity might decrease enough to explain the apparent interfacial resistance.

3.2.5 Calculating the association constant from MD simulation

The associativity K_1 of surfactant monomers, with concentration c_1, into dimers with concentration c_2 has the following relationship with the radial distribution function g(r) as[46]

$$K_1 = \frac{c_2}{c_1^2} = 4\pi \int_0^R g(r)\, r^2\, dr \tag{6}$$

To calculate g(r) between the two surfactants, we used umbrella sampling with 1.2 Å spacing between windows and a spring constant of 1450 kJ mol^{-1} nm^{-2}. To be generous to the pre-micellar aggregation hypothesis, we calculated K_1 taking a rather large separation distance R = 2.5 nm, counting a pair of surfactants with center of mass separation as great as 2.5 nm as a dimer. We also calculated a 90% confidence interval for K_1 based on the 5th and 95th percentile g(r) functions given by randomly resampling the biased trajectories (bootstrapping).

3.3 Results and discussion

3.3.1 Investigating re-dissolution

We found that re-dissolution of adsorbed surfactant into the silicone oil could not explain the apparent energetic barrier to adsorption. In Figure 3-3, the lines, predicted from Eq. 2, that correspond most closely with the experimental data are the black lines, which are theoretical predictions for dynamic surface tension (DST) in the presence of an adsorption resistance consistent with the modeling by Alvarez et al.[18] The blue lines are predictions of the same model with adsorption resistances removed. The black lines clearly predict the data better. The red lines are predictions for DST in the absence of resistances but allowing surfactant adsorbed from the water onto the oil-water interface to re-dissolve into the oil phase, using the rate constants described earlier. The figure shows that kinetic resistance and re-dissolution into the droplet phase have qualitatively different effects on the DST curve. The experimental resistance to adsorption expresses itself in a deviation at short times from the diffusion-limited case that lasts either until the equilibrium surface tension is achieved or until the diffusive resistance to adsorption dominates the energetic resistance. By contrast, the DST curve for re-dissolution does not deviate from the diffusion-limited case (blue lines) at short times. Instead, the deviation occurs at longer times at which the interface has filled up enough to support a significant concentration of surfactant at the oil sub-surface. This rules out Cause 1 from our list of possibilities.

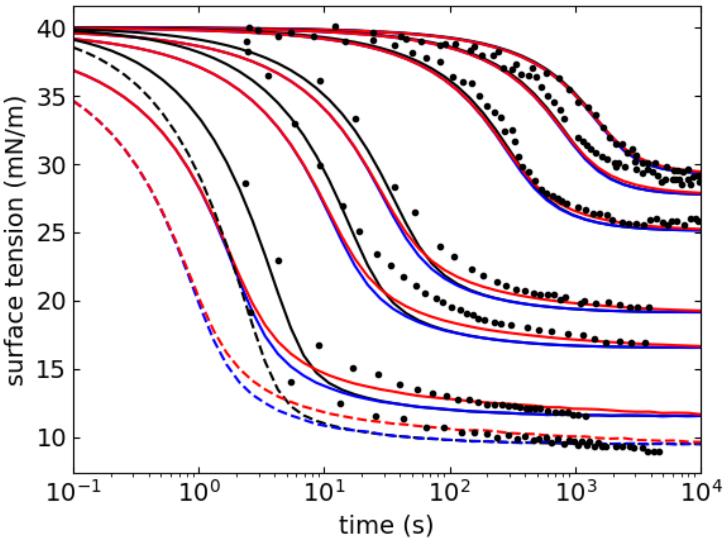

Figure 3-3: Interfacial tension at water/silicon oil interface versus logarithmic time for $C_{12}E_8$ from experimental data from Alvarez et al. in black dots, with data sets towards the left corresponding to higher concentrations. From left to right, the concentrations are 100 µM, 75 µM, 50 µM, 17.82 µM, 10.0 µM, 2.2 µM, 1.0 µM, and 0.6 µM. Three model predictions corresponding to each concentration are drawn with solid lines. Kinetically-and-diffusion-controlled, insoluble in oil (black); diffusion-controlled, insoluble in oil (blue); and diffusion-controlled, soluble in oil (red). The leftmost set of lines are dashed to make clear that they correspond to the same, highest, surfactant concentration.

3.3.2 Energy barrier estimation

Stationary (steady-state) solutions to the Smoluchowski equation (see B-2) are shown in Figure 3-4, with a fast sink boundary at x=0. The dashed blue line shows the underlying energy well without a barrier. Between x=2 and x=5, due to the flat energy landscape, the concentration profile (solid blue) is almost linear, as expected for Fickian diffusion. As the energy barrier E_b grows (orange and green dashed lines), the steady-state concentration gradient disappears at the right, and a steep concentration gradient forms at the outer base of the energy barrier.

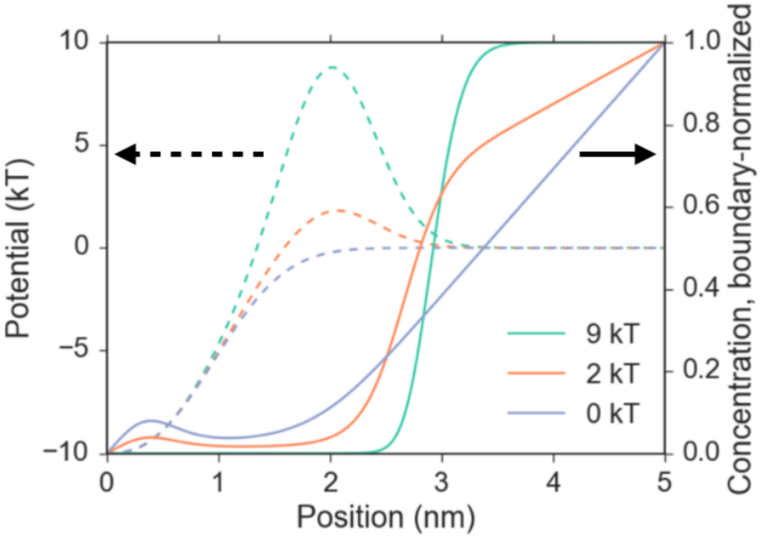

Figure 3-4: The probability densities with boundary concentrations normalized to unity are plotted with solid lines for three barrier heights E_b: 0 kT (blue), 2 kT (orange), and 9 kT (green). The corresponding energy landscapes are plotted with dashed lines. The black arrows indicate the axes corresponding to the dashed and solid lines.

Approximations for k_{ads} in the limits $E_b \rightarrow 0$ and $E_b \rightarrow \infty$ can be made. For the former, we calculate the adsorbing component velocity through a thin film with thickness equal to the distance between the source boundary and the energy cliff (l_b= 3 nm), assuming a linear drop from the boundary concentration to zero over this distance.

$$\text{(max. adsorption speed)} \approx \frac{D}{l_b} \tag{7}$$

Given our placement of the right-side boundary and the diffusion distance, this is the maximum adsorption speed without an energy barrier. In the case of a large barrier, the kinetics are dominated by the barrier, and we estimate with transition state theory where the transition state is the barrier peak and the reactive velocity is driven by the force over the length from peak to sink (l_a = 2 nm). For the large-barrier limit, we multiply the approximate force in the energy well E_a/l_a by the particle mobility D/k_BT to obtain the barrier-free drift velocity, and then reduce this by a Boltzmann factor due to the barrier,

$$\text{(barrier controlled adsorption speed)} \approx \frac{E_a/k_BT}{l_a} D \exp(-E_b/k_BT) \qquad (8)$$

An intermediate crossover occurs where neither the energetic barrier nor the diffusion resistance dominates. The approximations for the two limits give results close to the full calculation far from the crossover point, and they appear as dashed lines in Figure 3-5.

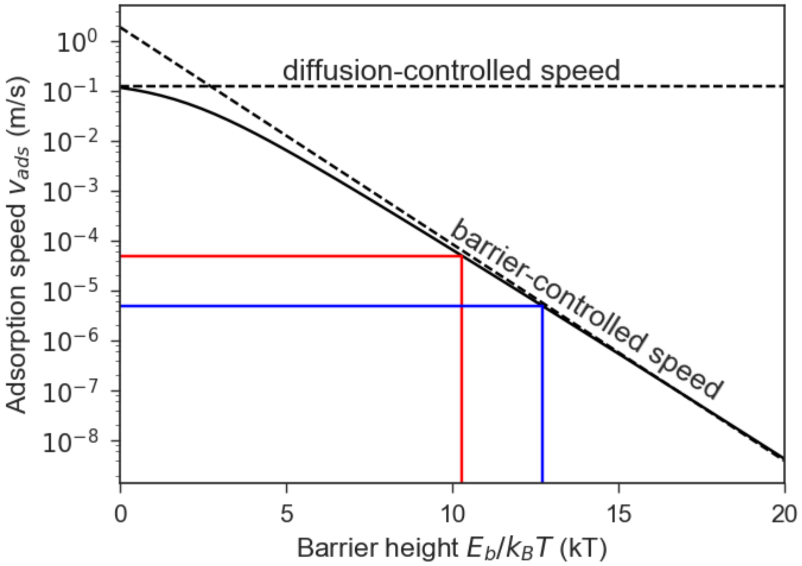

Figure 3-5: Adsorption speeds from limiting approximations (dashed black line) and stationary solution to Fokker-Planck equation (solid black). By interpolation from the adsorption speeds by Alvarez et al., the neat (red) and 90%-covered (blue) interfaces for $C_{12}E_8$ have barrier heights of 10 k_BT and 13 k_BT, respectively.

3.3.3 Molecular dynamics calculations of free energy barrier

We simulated surfactant-laden interfaces up to 130% of the empirical maximum surface coverage Γ_{max} and did not observe an energy barrier. Instead, in all cases, as seen in Figure 3-6, starting from the minimum in PMF, with increasing z, the potential monotonically approaches a plateau from below, with no overshoot that might represent a free energy barrier to adsorption.

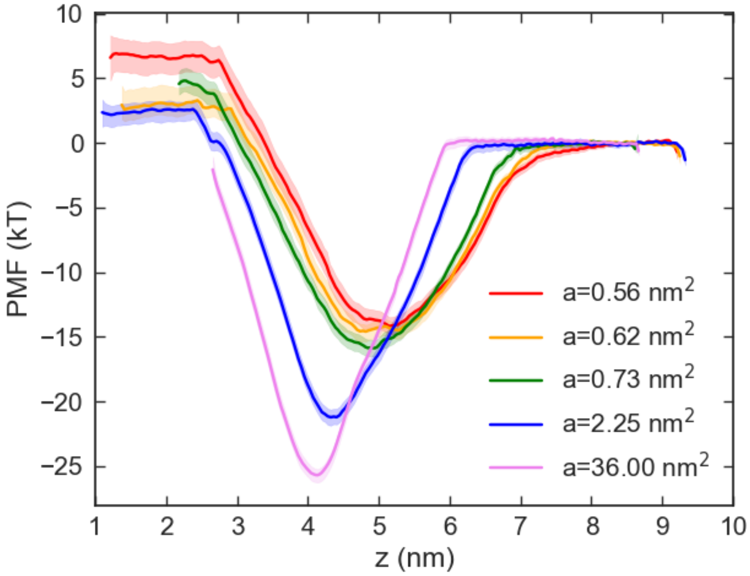

Figure 3-6: Potentials of mean force (PMF) in k_BT units plotted versus z in nm for increasing surface concentrations of $C_{12}E_8$ surfactant at an alkane/water interface, where the alkane is 2-methyl-5-ethylnonane. The plateau on the left side of the PMF represents dissolution into the bulk alkane phase, while the plateau on the right is dissolution into water. The small, abrupt drop at the far right end of each PMF is an artifact of the WHAM method. The shaded region around each PMF is the 95% confidence interval, and the molecular interfacial area a is indicated next to each legend symbol in nm^2/molecule.

In Figure 3-7, we plot the local diffusivities estimated from the fluctuations of harmonically-restrained surfactants, as described by Zhu and Hummer (2012).[42] To account for the reduction in adsorption speed shown by red and blue lines in Figure 3-5, the diffusivity would have to drop by a factor of around 10^4. There is no hint of any such diffusivity reduction in Figure 3-7. By confirming the surfactant encounters neither an energy barrier nor a zone of reduced diffusivity, we rule out Cause 2 from our above list.

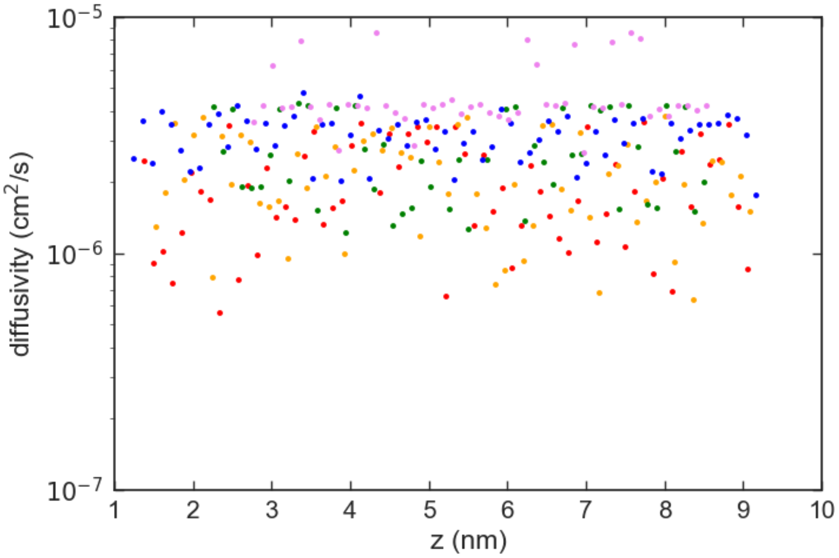

Figure 3-7: Diffusivities plotted versus z in nm for increasing surface concentrations of $C_{12}E_8$ surfactant. Color scheme is same as in Figure 3-6. Local diffusivities did not stray far from the expected values in bulk water.

3.3.4 Spontaneous adsorption

To further validate the absence of an energetic barrier, and to demonstrate that such a barrier is not hidden from the PMF, we ran simulations of spontaneous adsorption for surfactant molecules that had been pulled out from the surfactant monolayer and allowed to adopt independent configurations. If our interpretation of the PMF was incorrect, and we had somehow missed an energetic barrier with the WHAM technique, then the surfactant should be unable to rejoin the adsorbed monolayer after being pulled out. We performed this test on the second-most crowded interface, with a surfactant surface concentration of 2.6×10^{-6} moles/m^2, in excess of the experimentally determined maximum surface concentration of 2.25×10^{-6} moles/m^2. Using the PMF measured for this interface (orange curve in Figure 3-5), we integrated the Smoluchowski equation from the initial condition of surfactants starting at z = 8.3 nm with absorbing boundary conditions at z = 9.3 nm and z = 5.0 nm (c.f. horizontal axis of Figure 3-6). We selected the 5.0

nm position, because it corresponds to the PMF minimum for the two most crowded interfaces, at which position the test surfactant is inside the surfactant monolayer. We selected the 9.3 nm position, because it yielded a roughly 1:1 split of probability for first passage to each of the two boundaries. We calculated a 53% probability of the surfactant first passing through the z = 5.0 nm boundary and thus rejoining the surfactant monolayer, and a 47% probability of the surfactant first crossing the z = 9.3 nm boundary. Details of this calculation are in the SI. We then, in an MD simulation, pulled one test molecule of surfactant to a position of z = 8.3 nm from an interface loaded with 58 surfactants over an interfacial area of 36 nm^2. We chose z = 8.3 nm because while it is close to the interface, the PMFs are plateaued at this position, and snapshots of the surfactant at this position showed sufficient distance from the monolayer to have no interaction with other surfactant molecules, as would be expected for the PMF plateau. We then collected independent configurations with the test molecule restrained at the z = 8.3 nm position by a harmonic potential with spring constant 1500 kJ/mol nm^2. We allowed 1 ns to elapse between sampling configurations to allow relaxation of the surfactant monolayer and reorientation of the test surfactant. The autocorrelation of the restrained surfactant's head-to-tail vector decayed within 1 ns, as did the autocorrelation of each unrestrained surfactant's z position relative to the monolayer's center of mass. With each independent configuration, we then ran the simulation (without the harmonic restraint potential) until the test molecule crossed either boundary, at which point the simulation was stopped by the Plumed plug-in for Gromacs.[47] Remarkably, out of 10 repeats of this exercise, the surfactant re-adsorbed 5 times without crossing the outer boundary, and it crossed the outer boundary 5 times. Thus, the MD simulation itself is not hiding an energetic barrier from our PMF analysis. If there is a flaw in our search for an adsorption energy barrier through molecular simulation, it seems to be either in our choice of interfacial components, or in the bonding and interaction parameters of the simulated molecules.

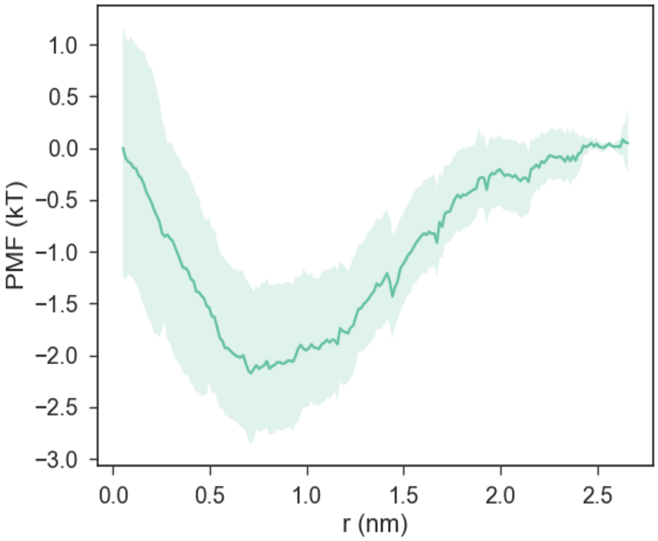

Figure 3-8: Potential of mean force of surfactant pair plotted versus radial distance between surfactant centers of mass. The shaded area is the 90% confidence interval.

3.3.5 Molecular dynamics simulation of pre-micellar aggregates

Next, we consider the effect of surfactant association. To be conservative, we considered surfactants less than 2.5 nm apart to be associated. The PMF in Figure 3-8 yields an associativity constant K_1 between 1.52×10^{-4} μM^{-1} and 6.21×10^{-5} μM^{-1} with 90% confidence. Even if c_1 equaled the $C_{12}E_8$ critical micelle concentration of 100 µM, the concentration ratio of dimers to monomers is at most 0.01. For trimers to achieve even this ratio with respect to the monomers, the dimer-monomer associativity for the third surfactant to join must be at least 50x greater than the monomer-monomer associativity, or roughly 4 k_BT deeper than the bottom of the shaded 90% confidence interval shown in Figure 3-8.

Even so, a concentration of small aggregates of a few percent or less relative to monomer concentration is insufficient to produce the observed resistance via a slow aggregate diffusion effect. And the effect – rather than acting at the CMC – must begin well below the CMC, which requires even deeper energy wells. The self-associativity of surfactants in dimers, trimers, and other small aggregates in pre-micellar solution seems much too small to produce the expected effect. This rules out Cause 3 from our list.

3.3.6 Nature of the apparent interfacial resistance

The adsorption model that allows for re-dissolution of surfactant into the oil phase gave results clearly different than the observed experimental resistance. A Smoluchowski-type analysis of the adsorption rate constant showed that we should expect an energy barrier at least 10 k_BT, if such a barrier is to explain the observed interfacial resistance to interfacial adsorption. Our molecular simulations did not show any such energy barrier to adsorption even at surface coverages above those achieved beyond the critical micelle concentration in experiments. Nor were the pre-micellar aggregates' somewhat slower diffusion sufficient to explain the observed resistance to adsorption.

The response delay between the observed DST and the diffusion-controlled DST was neither a fixed lag nor was it proportional to the diffusion-controlled adsorption time, which would put a constant gap between the diffusion-controlled response and observed response on the γ-log t graph.

Without a viable theoretical explanation for the apparent resistance assuming ideal experimental conditions, we consider the possibility that the apparent interfacial resistance is due to non-idealities in the experiments that the model does not capture. As we proposed in the introduction, the creation of interface at the initiation of the experiment could have an associated "dead time" due to depletion of surfactant from the diffusion layer by the ejected droplet. We are, however, cautious about this possibility, because significant discrepancies between the Alvarez et al. data and the diffusion-controlled model appear to exist up to at least 10 seconds, and the longest time it would take to grow a droplet from the experimental volume of 29 μL to our estimated pendant drop ejection volumes of 48 μL or 68 μL at the described 850 μL/min flow rate is 1-3 s. It is during these 1-3 s of growth before ejection and re-growth of a new experimental pendant drop that unsaturated interface could potentially deplete surfactant from a layer of solution that influences the new droplet. Furthermore, we don't even know if an aged pendant droplet was ejected prior to the experiments of Alvarez et al. The surface of the experimental pendant droplet may have been grown from a relatively flat silicone oil/water interface at the tip of the capillary, and the 25x growth of this interfacial area from capillary cross-section to experimental droplet surface could be sufficient to render the interface "clean" for practical purposes. In the case of the microtensiometer used by Guo, the hemispherical droplet is not slowly grown but is rapidly ejected from the capillary by a brief increase in the capillary pressure. Although this process would create significant unsaturated interfacial area, we do not know the time the ejected droplet would remain close enough to the fresh interface to deplete a layer of surfactant. However, if such processes occurred, this could lead to a delay in mass transfer to the interface, until the liquid zone near the interface could be replenished with surfactant, and this would appear as a resistance to interfacial mass transfer. To confirm or refute this possibility, detailed experimental interrogation of the flow and transport processes in the 10 seconds or so around the time of interface creation would need to be carried out, possibly supported by transport modeling.

3.4 Summary and conclusions

We tested several potential explanations for the apparent resistance to adsorption observed for alkyl ethoxylates at water/oil interfaces.[18,19] We found none of them to be consistent with molecular simulation and thermodynamic/transport models. Although an expected energy barrier of at least 10 k_BT can be inferred from experiments, the PMF calculations did not yield an energy barrier even a fraction of a k_BT despite very high surface concentration. A local diffusivity calculation using the harmonically biased interfacial surfactant runs did not show any deviation in diffusivity remotely large enough to cause the appearance of a kinetic barrier. And finally, in the most straightforward test for an energy barrier in simulation, we allowed a surfactant molecule to spontaneously adsorb to the interfacial monolayer, which it did within nanoseconds.

Thus, we did not find a definitive answer to the adsorption resistance question, but we hope this work inspires future studies that attempt to model a surfactant solution adsorbing to interfaces in different tensiometry apparatuses (e.g. pendant bubble/oil drop and continuous-flow) to expose discrepancies between tensiometry methods. One test of the robustness of calibrated adsorption rate equations is to fit to both adsorption and desorption processes which can be carried out in continuous-flow tensiometers.[48] Or perhaps a future study might identify flaws in our molecular simulation or analysis that lead us to erroneously predict no adsorption resistance.

Qualitative disagreement between experiment and molecular simulation of rates of adsorption is not unheard of. McLean and Phillips inferred activation energies to bring lipids from a bilayer into water that were 30 kJ/mol greater than the transfer free energies.[49] Yet, when Tieleman and Marrink calculated the potential of mean force for transfer of a DPPC molecule from a DPPC bilayer into water with umbrella sampling, they observed no activation barrier above the transfer free energy.[50] Thus, the large disagreement we observe between experimentally inferred interfacial resistances to adsorption at a water/oil interface and what can be inferred from molecular simulation of the interface is in line with our simulations of $C_{12}E_8$ transported to the water/oil interface.

Finally, although we ruled out a non-equilibrium concentration gradient effect for non-ionic surfactants because the deformation associated with dilation/contraction does not result in any immediate free energy change, it would be interesting to study surface excess electrochemical potentials and their contribution to surface tension in the presence of ionic surfactants with long-range interactions that change upon nonequilibrium interfacial dilation and contraction.

3.5 Acknowledgements

This research was made possible in part by a grant from BP/The Gulf of Mexico Research Initiative. We also acknowledge the support from the NSF under grant CBET-0853662. Any opinions, findings, and conclusions or recommendations expressed in this material are those of the authors and do not necessarily reflect the views of the National Science Foundation (NSF). Simulations were supported through computational resources and services provided by Advanced Research Computing at the University of Michigan, Ann Arbor. We thank Lynn Walker, Shelley Anna, and Stephanie Kirby from Carnegie Mellon University for helpful discussion and for sharing Yang Guo's master's thesis.

3.6 References

(1) Chang, C.-H.; Franses, E. I. Adsorption Dynamics of Surfactants at the Air/Water Interface: A Critical Review of Mathematical Models, Data, and Mechanisms. *Colloids Surf. Physicochem. Eng. Asp.* **1995**, *100*, 1–45.

(2) Karsa, D. R. *Surfactants in Polymers, Coatings, Inks and Adhesives*; Taylor & Francis US, 2003.

(3) Chistyakov, B. E. 6. Theory and Practical Application Aspects of Surfactants. In *Studies in Interface Science*; V.B. Fainerman, D. M. and R. M., Ed.; SurfactantsChemistry, Interfacial Properties, Applications; Elsevier, 2001; Vol. 13, pp 511–618.

(4) Shaw, D. *Introduction to Colloid and Surface Chemistry*, Fourth.; Butterworth-Heinemann, 1992.

(5) Yuan, F.; Wang, S.; Larson, R. G. Potentials of Mean Force and Escape Times of Surfactants from Micelles and Hydrophobic Surfaces Using Molecular Dynamics Simulations. *Langmuir* **2015**, *31* (4), 1336–1343.

(6) Chapter 1 Theory of Surface Tension. In *Studies in Interface Science*; Prokhorov, A. I. R. and V. A., Ed.; Interfacial Tensiometry; Elsevier, 1996; Vol. 3, pp 1–47.

(7) Liu, M.; Beattie, J. K.; Gray-Weale, A. The Surface Relaxation of Water. *J. Phys. Chem. B* **2012**, *116* (30), 8981–8988.

(8) Bai, C.; Herzfeld, J. Surface Propensities of the Self-Ions of Water. *ACS Cent. Sci.* **2016**, *2* (4), 225–231.

(9) Fainerman, V. B.; Miller, R. Adsorption Kinetics of Short-Chain Alcohols at the Water/Air Interface: Diffusion-Controlled Adsorption under the Conditions of a Nonequilibrium Surface Layer. *J. Colloid Interface Sci.* **1996**, *178* (1), 168–175.

(10) Fainerman, V. B.; Zholob, S. A.; Miller, R.; Joos, P. Non-Diffusional Adsorption Dynamics of Surfactants at the Air/Water Interface: Adsorption Barrier or Non-Equilibrium Surface Layer. *Colloids Surf. Physicochem. Eng. Asp.* **1998**, *143* (2–3), 243–249.

(11) Lin, S.-Y.; Wang, W.-J.; Hsu, C.-T. Adsorption Kinetics of 1-Octanol at the Air−Water Interface. *Langmuir* **1997**, *13* (23), 6211–6218.

(12) Eastoe, J.; Dalton, J. S.; Rogueda, P. G. A.; Crooks, E. R.; Pitt, A. R.; Simister, E. A. Dynamic Surface Tensions of Nonionic Surfactant Solutions. *J. Colloid Interface Sci.* **1997**, *188* (2), 423–430.

(13) Lin, S.-Y.; Tsay, R.-Y.; Lin, L.-W.; Chen, S.-I. Adsorption Kinetics of C12E8 at the Air−Water Interface: Adsorption onto a Clean Interface. *Langmuir* **1996**, *12* (26), 6530–6536.

(14) Mulqueen, M.; Datwani, S. S.; Stebe, K. J.; Blankschtein, D. Dynamic Surface Tensions of Aqueous Surfactant Mixtures: Experimental Investigation. *Langmuir* **2001**, *17* (24), 7494–7500.

(15) Alvarez, N. J.; Walker, L. M.; Anna, S. L. A Microtensiometer To Probe the Effect of Radius of Curvature on Surfactant Transport to a Spherical Interface. *Langmuir* **2010**, *26* (16), 13310–13319.

(16) Miller, R.; Aksenenko, E. V.; Fainerman, V. B. Dynamic Interfacial Tension of Surfactant Solutions. *Adv. Colloid Interface Sci.* **2017**, *247* (Supplement C), 115–129.

(17) Lindfors, L.; Skantze, P.; Skantze, U.; Westergren, J.; Olsson, U. Amorphous Drug Nanosuspensions. 3. Particle Dissolution and Crystal Growth. *Langmuir* **2007**, *23* (19), 9866–9874.

(18) Alvarez, N. J.; Lee, W.; Walker, L. M.; Anna, S. L. The Effect of Alkane Tail Length of CiE8 Surfactants on Transport to the Silicone Oil–water Interface. *J. Colloid Interface Sci.* **2011**, *355* (1), 231–236.

(19) Guo, Y. Characterization of Rhamnolipid at Oil-Water Interfaces Using a Microtensiometer, Carnegie Mellon University.

(20) Ward, A. F. H.; Tordai, L. Time-Dependence of Boundary Tensions of Solutions I. The Role of Diffusion in Time-Effects. *J. Chem. Phys.* **1946**, *14* (7), 453–461.

(21) Chapter 4 The Dynamics of Adsorption at Liquid Interfaces. In *Studies in Interface Science*; Dukhin, S. S., Kretzschmar, G., Miller, R., Eds.; Dynamics of Adsorption at Liquid Interfaces; Elsevier, 1995; Vol. 1, pp 100–139.

(22) *Computational Methods for Complex Liquid-Fluid Interfaces*; Rahni, M., Karbaschi, M., Miller, R., Eds.; Progress in Colloid and Interface Science; CRC Press, 2015.

(23) Kalinin, V. V.; Radke, C. J. An Ion-Binding Model for Ionic Surfactant Adsorption at Aqueous-Fluid Interfaces. *Colloids Surf. Physicochem. Eng. Asp.* **1996**, *114*, 337–350.

(24) Tan, L.; Pratt, L. R.; Chaudhari, M. I. Molecular-Scale Description of SPAN80 Desorption from the Squalane-Water Interface. *ArXiv160304033 Cond-Mat Physicsphysics* **2016**.

(25) Eastoe, J.; Dalton, J. S. Dynamic Surface Tension and Adsorption Mechanisms of Surfactants at the Air–water Interface. *Adv. Colloid Interface Sci.* **2000**, *85* (2–3), 103–144.

(26) Miller, R.; Makievski, A. V.; Fainerman, V. B. 4. Dynamics of Adsorption from Solutions. In *Studies in Interface Science*; V.B. Fainerman, D. M. and R. M., Ed.; SurfactantsChemistry, Interfacial Properties, Applications; Elsevier, 2001; Vol. 13, pp 287–399.

(27) Casandra, A.; Ismadji, S.; Noskov, B. A.; Liggieri, L.; Lin, S.-Y. A Study on the Method of Short-Time Approximation – Criteria for Applicability. *Int. J. Heat Mass Transf.* **2015**, *90*, 752–760.

(28) Lin, S.-Y.; McKeigue, K.; Maldarelli, C. Diffusion-Controlled Surfactant Adsorption Studied by Pendant Drop Digitization. *AIChE J.* **1990**, *36* (12), 1785–1795.

(29) United States Pharmacopeia and National Formulary (USP 40-NF 35); United States Pharmacopeial Convention: Rockville, MD, 2017; Vol. 1, pp 7768–7769.

(30) Scheele, G. F.; Meister, B. J. Drop Formation at Low Velocities in Liquid-Liquid Systems: Part I. Prediction of Drop Volume. *AIChE J.* **1968**, *14* (1), 9–15.

(31) Humphrey, J. A. C. Note on Drop Formation at Low Velocity in Quiescent Liquids. *Chem. Eng. Sci.* **1980**, *35* (6), 1452–1454.

(32) Chemistry, I. U. of P. and A. IUPAC Gold Book - diffusion layer (concentration boundary layer) https://goldbook.iupac.org/html/D/D01725.html (accessed Nov 14, 2017).

(33) Diamant, H.; Andelman, D. Kinetics of Surfactant Adsorption at Fluid−Fluid Interfaces. *J. Phys. Chem.* **1996**, *100* (32), 13732–13742.

(34) Yariv, E.; Frankel, I. The Diffusion-Control Limit Revisited. *Phys. Rev. Lett.* **2002**, *89* (26), 266107.

(35) Duncan, S. L.; Dalal, I. S.; Larson, R. G. Molecular Dynamics Simulation of Phase Transitions in Model Lung Surfactant Monolayers. *Biochim. Biophys. Acta* **2011**, *1808* (10), 2450–2465.

(36) Risken, H. *The Fokker-Planck Equation: Methods of Solution and Applications*; Springer Series in Synergetics; Springer Berlin Heidelberg, 1996; Vol. 18.

(37) Radke, C. J. Gibbs Adsorption Equation for Planar Fluid–fluid Interfaces: Invariant Formalism. *Adv. Colloid Interface Sci.* **2015**, *222*, 600–614.

(38) Kumar, S.; Rosenberg, J. M.; Bouzida, D.; Swendsen, R. H.; Kollman, P. A. The Weighted Histogram Analysis Method for Free-Energy Calculations on Biomolecules. I. The Method. *J. Comput. Chem.* **1992**, *13* (8), 1011–1021.

(39) Abraham, M. J.; Murtola, T.; Schulz, R.; Páll, S.; Smith, J. C.; Hess, B.; Lindahl, E. GROMACS: High Performance Molecular Simulations through Multi-Level Parallelism from Laptops to Supercomputers. *SoftwareX* **2015**, *1–2*, 19–25.

(40) Hub, J. S.; de Groot, B. L.; van der Spoel, D. G_wham—A Free Weighted Histogram Analysis Implementation Including Robust Error and Autocorrelation Estimates. *J. Chem. Theory Comput.* **2010**, *6* (12), 3713–3720.

(41) Huston, K. J.; Larson, R. G. Reversible and Irreversible Adsorption Energetics of Poly(Ethylene Glycol) and Sorbitan Poly(Ethoxylate) at a Water/Alkane Interface. *Langmuir* **2015**.

(42) Zhu, F.; Hummer, G. Convergence and Error Estimation in Free Energy Calculations Using the Weighted Histogram Analysis Method. *J. Comput. Chem.* **2012**, *33* (4), 453–465.

(43) Fuchs, P. F. J.; Hansen, H. S.; Hünenberger, P. H.; Horta, B. A. C. A GROMOS Parameter Set for Vicinal Diether Functions: Properties of Polyethyleneoxide and Polyethyleneglycol. *J. Chem. Theory Comput.* **2012**, *8* (10), 3943–3963.

(44) Bussi, G.; Donadio, D.; Parrinello, M. Canonical Sampling through Velocity Rescaling. *J. Chem. Phys.* **2007**, *126* (1), 014101.

(45) Parrinello, M.; Rahman, A. Polymorphic Transitions in Single Crystals: A New Molecular Dynamics Method. *J. Appl. Phys.* **1981**, *52* (12), 7182–7190.

(46) Warren, D. M. Molecular Dynamics Simulation of Barite and Celestite Ion-Pairs. Thesis, Georgia Institute of Technology, 2011.

(47) Tribello, G. A.; Bonomi, M.; Branduardi, D.; Camilloni, C.; Bussi, G. PLUMED 2: New Feathers for an Old Bird. *Comput. Phys. Commun.* **2014**, *185* (2), 604–613.

(48) Svitova, T. F.; Wetherbee, M. J.; Radke, C. J. Dynamics of Surfactant Sorption at the Air/Water Interface: Continuous-Flow Tensiometry. *J. Colloid Interface Sci.* **2003**, *261* (1), 170–179.

(49) McLean, L. R.; Phillips, M. C. Kinetics of Phosphatidylcholine and Lysophosphatidylcholine Exchange between Unilamellar Vesicles. *Biochemistry (Mosc.)* **1984**, *23* (20), 4624–4630.

(50) Tieleman, D. P.; Marrink, S.-J. Lipids Out of Equilibrium: Energetics of Desorption and Pore Mediated Flip-Flop. *J. Am. Chem. Soc.* **2006**, *128* (38), 12462–12467.

CHAPTER 4

Forward flux sampling simulation of polymer desorption from a smooth, solid surface into dilute solution

4.1 Introduction

To our knowledge, the rate of desorption of isolated chains from an interface has not been predicted using theory or simulation beyond post-hoc rationalization of a power law observed in some recent experiments with fluorescent imaging.[1,2] In the textbook by Fleer et al., the authors noted that, even in the absence of a kinetic barrier to desorption, the adsorbed polymer yields an equilibrium concentration in the subsurface solution that is so small that the resulting concentration gradient is unable to drive diffusion fast enough to observe experimentally in most cases.[3] The reason for the minuscule rate of desorption of long polymers from surfaces is that, if each monomer can adsorb with an adsorption free energy ϵ_{PW} that is an appreciable fraction of $k_B T$ or more, then the total adsorption energy of the polymer with N monomers will be of order $N\epsilon_{PW} >> 1$. The chain will then readily pay the entropic penalty to adsorb such a high fraction of these monomers that desorption of a chain becomes an exceedingly rare event. Although this general conclusion seems sound, there are situations in which one should expect exceptions. First, the adsorption energy per monomer may be very feeble, $\epsilon_{PW} << 1$, in which case even chains of modestly high molar mass are bound with energies $N\epsilon_{PW} < 10\ k_B T$, or so. These chains could desorb at a measurable rate. A second possibility is that only a fraction of the monomers can adsorb. This could occur for a variety of reasons. The polymer could be a heteropolymer, such as a protein in which only very hydrophobic, or hydrophilic, residues can bind. The adsorption might be due to charge interactions, wherein only charged monomers are attracted to charged sites on the surface, and if charge density is low on both polymer and surface, adsorption might be relatively weak. A case where this is known to be relevant is that of polyelectrolytes that adsorb onto a surface, either a bare surface or onto a surface already coated with polymer, such as occurs in the Layer-by-Layer (LbL) process. Depending on pH and salt concentration, there may be a relatively small number of charges per polymer able to bind to the pre-existing layer, thus making the adsorption partially reversible, as in fact is experimentally well known in LbL coating.[4] A related situation might be one in which monomers stick to a surface by van der Waals interactions, but are electrostatically repelled from the surface. In this case, the total free energy of adsorption is reduced, allowing faster desorption. Yet another situation might be one in which desorption somehow becomes cooperative, in that monomers that desorb are somehow kept from re-adsorbing, allowing monomers to desorb sequentially. This situation might arise if there is some force, for example, a hydrodynamic force, that acts on the polymers, so that desorbed monomers have little chance to re-adsorb, and so are removed sequentially from the surface rather than needing many monomers to simultaneously overcome their desorption barriers.[5]

Thus, while the simplest case of desorption of long chains of strongly adsorbing monomers has well-known, and trivial, desorption kinetics, namely negligible desorption on experimental time scales, there are interesting situations in which we do not expect this to hold, and a method to calculate the actual rate may be important. Even in cases for which desorption is likely to be exceedingly slow, there may be reasons to nonetheless wish to know the rate. For example, polymers coating implanted materials in the body may be dangerous or toxic, and one wishes to be confident that their desorption rate is completely negligible. Since calculations of desorption rates are, with the few exceptions described below, almost unknown in the literature, we wish to advance understanding of desorption by applying the rare-event sampling method *forward flux sampling* (FFS) to compute desorption rates for uncharged homopolymers in the absence of flow or any external field. We test chains of varying length, varying polymer-wall interaction energy, and various internal potentials governing chain configuration. A rare-event sampling method, such as FFS, is needed to determine desorption rate, since direct simulation of the rate will almost never see a single desorption event for strongly bound chains, even when using coarse-grained simulation methods.

In the remainder of this Introduction, we position our work within the existing literature. First, we review experimental studies of isolated polymer adsorption to solid/liquid interfaces. Second, we review the concept of "bulk-mediated diffusion" or "hopping" along an adsorbing surface, observed in some recent experiments, which is relevant to our analysis. Third, we briefly review theories of isolated polymer adsorption thermodynamics. Fourth, we review previous molecular simulations of polymer desorption. Then, we describe the forward flux sampling method and how its accuracy is analyzed. Then, we move onto the Modeling Details, Results and Discussion, and Summary and Conclusions.

4.1.1 Experimental studies of isolated polymer adsorption to solid/liquid interfaces

The experiments that encouraged us to initiate our study were carried out by Skaug, Mabry, and Schwartz[1], who followed the movement of poly(ethylene oxide) (PEO) chains labeled with fluorescein isothiocyante (FITC) near a polished fused silica surface coated with trimethylsiloxane (TMS) using Total Internal Reflectance Fluoresence Microscopy (TIRFM). In TIRFM, light undergoes total internal reflection, yielding a so-called evanescent wave which illuminates a narrow zone just beyond the reflective interface, with intensity decaying exponentially with distance from the interface. They observed an extremely slow surface diffusion of PEO molecules punctuated by apparent jumps over much larger distances. These jumps evidently occurred when the polymer desorbed from the wall, traversed a distance through the bulk fluid, and the re-adsorbed. These apparent jumps in the 2D trajectory are called *bulk-mediated surface displacements*. Skaug et al. measured the time t_{des} for an adsorbed polymer to jump, thereby obtaining desorption times for the PEO from the TMS-coated silica. The authors repeated these measurements many times to obtain the distribution of desorption times for several PEO chains between 45 and 908 repeat units long. They also measured the distribution of displacements of the polymer along the surface observed for a particular time interval. By fitting these distributions to a theoretical model[6] by Chechkin et al. for bulk-mediated surface displacements of particles near an adsorbing surface (discussed below), they obtained an adsorption rate Q_{ads} with dimensions of reciprocal time describing the frequency of adsorption of the polymer from a lattice site adjacent to the interface. Note that the model by Chechkin et al. is for particles which occupy a single lattice site, and thus use of this model implicitly places the entire polymer molecule into a single lattice site. Multiplying by the radius of gyration R_g reported by Skaug et al., Q_{ads} can be readily converted to a more familiar continuum adsorption rate constant k_{ads} with dimensions of speed. The flux of adsorbing material is then $k_{\mathrm{ads}}c_0$ given a concentration c_0 adjacent to the interface, i.e. the subphase concentration.

The authors found that the observed distribution of desorption times was not exponential, implying that the requirements for a Poisson process with exponential waiting time distribution were not met. If each adsorbed polymer could adopt an independent, equilibrium configuration within a time t_{relax}, and this surface relaxation time was much shorter than the desorption time, i.e., $t_{\text{relax}} \ll \langle t_{\text{des}} \rangle$, then the number of chains desorbing within any time interval would be given by a Poisson process, and the resulting distribution of desorption times would be exponential. Instead, the desorption time distribution for the PEO-FITC had a fat tail, fit by a power law with exponent nearly equal to -2.5 at each molecular weight tested. As the authors noted, the non-exponential distribution could be explained by the trapping of PEO-FITC in an adsorbed state that does not relax its configuration quickly relative to the mean desorption time $\langle t_{\text{des}} \rangle$. The authors identified these adsorbed states as "non-equilibrium." Some care has to be taken to contrast this process with the non-equilibrium adsorption phenomena that arise for irreversibly-adsorbing chains and in dense surface layers which become glassy or jammed near the surface. [7–9] While the adsorbed PEO-FITC on the TMS-coated surface remains "non-equilibrium" on the timescale of a single chain desorption event – that is, the configuration of each PEO-FITC molecule upon desorption could be correlated with the earlier configuration upon adsorption – the equilibrium distribution of adsorbed states may be explored over the timescale of the entire experiment, which encompasses a multitude of independent adsorption and desorption events.

Skaug et al. found that the average desorption time $\langle t_{\text{des}} \rangle$ scales as a power law $\propto N^{0.6}$ rather than as an exponential increase $\propto \exp(N)$ or $\propto \exp(N^{\nu})$, where ν is the Flory exponent, equal to 0.6 for a polymer good solvent, as is the case for PEO in water. Skaug et al. and later Wang et al. favored a sequential desorption mechanism to explain the power law [1,2]. We quote a passage from the latter:

"The characteristic time associated with the desorption of a train [i.e., a continuous sequence of adsorbed monomers] is expected to be $\tau_{\text{train}} \sim \exp[l_{\text{train}} \epsilon / k_B T]$, where l_{train} is the length of the train [i.e. number of monomers in the train] and ϵ is the binding energy of each polymer segment. The total desorption time for the polymer chain is therefore $n_{train}\tau_{\text{train}}$where n_{train} is the number of trains per polymer chain. Eisenriegler et al. indicated that for a loop-train-tail conformation $n_{train}\sim N^{0.6}$. Thus, one expects the desorption time to scale as $N^{0.6}$, as we previously observed for PEG desorbing from a solid hydrophobic surface."

The logic is clear, but we make a few of the points more explicit here. In the paper by Eisenriegler et al.,[10] cited above, it was found that $N_{\text{train}}\sim N^{0.6}$ where N_{train} is the total number of adsorbed monomers per chain ($N_{\text{train}} = n_{train}l_{train}$), equivalent to the total number of monomers in trains per chain. If one presumes that the number of monomers per train is independent of chain length, which is reasonable for long enough chains, then one has $n_{\text{train}} \sim N^{0.6}$. Obviously if $t_{\text{des}} = n_{\text{train}}\tau_{\text{train}}$, then $t_{\text{des}} \sim N^{0.6}$.

We have some reservations regarding this theory. The assumed sequence of independent train desorptions whose desorption times add up to the total desorption time ignores the likelihood that a train, once desorbed, could simply re-adsorb, as long as other trains keep the polymer pinned to the surface. However one estimates n_{train}, the amount of time that has to pass without any trains re-adsorbing is on the order of t_{desorb}, which Skaug et al. found to be between 0.1 s and 1 s. We cannot imagine why a desorbed train might resist re-adsorption over such a long period of time.

If we allow frequent train re-adsorption, we would expect the total waiting time to scale exponentially as $\sim \tau_{\text{train}}^{n_{\text{train}}} = \exp[n_{\text{train}}l_{\text{train}}\epsilon/k_BT]$ rather than $\sim n_{\text{train}}\tau_{\text{train}}$. The latter scaling seems more suited to a pulled desorption, where desorbed trains would be held away from the surface by tension, rather than the spontaneous adsorption we aim to describe. Sequential irreversible desorption of trains also neglects influence of chain diffusivity. Although Skaug et al. and Wang et al. cleverly model the desorption process as sequential train desorption to make sense of their results, we are skeptical that this mechanism is realistic. Skaug et al. also point out that with $t_{\text{des}} \propto N^{0.6}$ and $Q_{\text{ads}} \propto N^{-1.2}$, the equilibrium ratio h between adsorbed surface concentration Γ and bulk concentration c (h = Γ/c) will be nearly constant over the range of molecular weights studied, i.e. $h \propto N^0$. See the Supporting Information Section S.3 for a detailed approach to this result. As is well known, in dilute solution, the diffusivity D of a polymer chain scales as $N^{-\nu}$ due to hydrodynamic coupling to entrained solvent. As a first approximation, for an isolated polymer that is not strongly adsorbed (pancaked) to the surface, we expect this value of the chain diffusivity roughly to describe polymer diffusivity near a surface. Because $\nu \approx 0.6$ for PEO in aqueous solution, the scaling $t_{\text{des}} \propto D^{-1}h^0 \propto N^{0.6}$ can just as well be explained by the scaling of D with N and a simple model of a particle escaping from a potential well, rather than by deploying the sequential irreversible desorption mechanism. Although the result is the same as observed by Skaug et al., the counterintuitive sequential-desorption mechanism could be re-interpreted as a thermodynamic binding free energy that is independent of chain length, which is also counterintuitive.

FITC has been reported to adsorb to carbon single-walled nanotubes and to porous graphene.[11] PEO sticks to and shields hydrophobic surfaces in water, so it seems likely that the conjugated PEO and FITC would interact as well. However, Skaug et al. found that free FITC did not adsorb “appreciably” to the surface at the same concentrations they studied PEO-FITC, so the authors reasonably concluded that FITC alone was not the primary cause of PEO-FITC adsorption.

4.1.2 Theory of bulk-mediated diffusion

Skaug et al. obtained the adsorption rate constant k_{ads} by fitting the probability density $\lambda(r)$ of the distance of bulk-mediated surface jumps r where r is the distance the molecule moves parallel to the surface in a single jump by means of desorption, bulk diffusion, and re-adsorption. The fitting equation to a formula derived by Chechkin et al. in their Appendix A (Eqn. A8) is:[6]

$$\lambda(r)=\frac{1}{\mu\tau_{\text{des}}D}-\frac{\pi r}{2(\mu\tau_{\text{des}}D)^2}\left[H_0\left(\frac{r}{\mu\tau_{\text{des}}D}\right)-Y_0\left(\frac{r}{\mu\tau_{\text{des}}D}\right)\right] \tag{1}$$

where $\mu=\frac{1}{k_{\text{ads}}\tau_{\text{des}}}=\frac{k_{\text{des}}}{k_{\text{ads}}}$, H_0 is the zeroth-order Struve function and Y_0 is the zeroth-order Bessel function of the second kind. Making the substitution for μ yields the following.

$$\lambda(r)=\frac{k_{\text{ads}}}{D}-\frac{k_{\text{ads}}^2\pi r}{2D^2}\left[H_0\left(\frac{k_{\text{ads}}r}{D}\right)-Y_0\left(\frac{k_{\text{ads}}r}{D}\right)\right] \tag{2}$$

Noting that the distribution is normalized to unity, one can see that faster adsorption k_{ads} narrows the distribution of bulk-mediated jump distances, whereas a high bulk diffusivity D broadens it. Eq. (2) shows that t_{des} does not influence the size distribution of bulk-mediated jumps. Although t_{des} controls the time between jumps, it is irrelevant to the size of the jump in distance once the chain is desorbed, assuming k_{ads} is fixed. Skaug et al. sought to measure t_{des} directly from the trajectories, using the time interval between jumps. However, taking the parameters used by Skaug et al. for the M = 5 kg/mole chain (located in their Supporting Information) and the bulk-mediated jump distribution above, we find that 64% of jumps are smaller than the reported distance resolution of 0.040 μm, which suggests the authors may have systematically undercounted the number of jumps. Their t_{des} calculation may therefore be 3× too large, unless they made a correction to account for jumps that they cannot measure, which is not apparent from the manuscript. They do mention adding a random Gaussian displacement with standard deviation of 0.040 μm to immobilized particle trajectories, but it is not clear how this would correct their t_{des}. Nonetheless, neither the non-exponential distribution of desorption times nor the mean desorption time are attributable to this possible inaccuracy, because $\frac{k_{\text{ads}}}{D_b}$ is almost constant over the range of molecular weights tested, and so the correction factor for t_{des} would be constant as well.

4.1.3 Theories of isolated polymer adsorption thermodynamics and expected desorption rate for strongly adsorbed chains

In the limit of strong adsorption, a polymer chain flattens onto the surface like a pancake into a layer of thickness comparable to that of a Kuhn length of the polymer chain, and each monomer experiences the same mean-field potential V_{MF}, which in this case is the thermodynamic (i.e., Boltzmann-weighted) average interaction between the wall and the monomer, and is negative in sign, or attractive, i.e.,

$$V_{MF}(\sigma_{PW}, \epsilon_{PW}) = \int_{z=0} V_W(z; \sigma_{PW}, \epsilon_{PW}) \exp\left(-\frac{1}{k_B T} V_W(z; \sigma_{PW}, \epsilon_{PW})\right) dz \tag{3}$$

There is also a positive, repulsive, contribution to the free energy due to the confinement of the monomers to the surface region; i.e., the total free energy is [12]

$$F \cong k_B T N \left(\frac{a}{l}\right)^{\frac{1}{\nu}} + N V_{MF} \tag{4}$$

Here a is the Kuhn length, and l is the range of the adsorption well within which the polymer is confined. For a we can use the polymer bond length of the freely-jointed chain l_b, but l is less clearly defined. We try to tune l to find a universal plot for the desorption times of strongly-adsorbing chains, and the result of this effort is in the SI. Our underlying kinetic scaling assumption is that,

$$\frac{t_{\mathrm{des}} D}{R_g^2} \propto \exp\left(-\frac{F}{k_B T}\right) \tag{5}$$

We here drop the configurational term in Equation 4 to obtain a simple relation that we will refer to as the strong-adsorption scaling law:

$$\ln\left(\frac{t_{\mathrm{des}} D}{R_g^2}\right) \propto \frac{N V_{MF}(z; \sigma, \epsilon)}{k_B T} \tag{6}$$

If the variance in the distance of a monomer from the wall becomes larger than the width of the potential, the polymer is in a strong fluctuation regime of adsorption, and Equations 3 and 5 can no longer be relied upon. Instead, it is better to use field-theoretic methods to obtain desorption times.[12] Eisenriegler, Kremer, and Binder (1982) derived scaling exponents for the desorption time from the Gaussian polymer field theory for an ideal chain near the crossover point from adsorption to depletion by renormalization group theory.[10] For a self-avoiding walk, at the crossover point, the number of adsorbed monomers scales as $N_{\text{train}} \propto N^{\phi}$, and the exponent ϕ relating the number of adsorbed monomers to the total number of monomers N in the chain is approximately 0.6, as one might expect at the cross-over point where the chain configuration and monomer density is relatively unaffected by the presence of wall. Thus, the fraction of monomers that are adsorbed shrinks to zero as the chain becomes longer at the cross-over point.

4.1.4 Previous molecular simulations of polymer desorption

In what follows, we describe published works that are the most similar to what we propose here. Wang, Rajagopalan, and Mattice[13] performed Monte Carlo simulations on a cubic lattice of the desorption of an adsorbed film of polymer from a surface. Their results cannot explain the experiments of Skaug et al. because the experimental chains were isolated while the simulated chains shared the surface with other adsorbed chains, giving a volume fraction in the adsorbing layer as high as 0.62. Dutta, Dorfman, and Kumar[5] simulated desorption of isolated Kremer-Gest bead-spring chains in a shearing flow, but in the absence of flow, the chains did not desorb during the simulation, so the kinetics of desorption in this limit could not be measured.

Källrot and Linse (2007) studied desorption of polymers which had adsorbed under an attractive potential and were then switched to a repulsive potential, but these results are of limited use for understanding desorption from an attractive wall. Paturej, Milchev, Rostiashvili, and Vilgis

(2012) studied the detachment time of polymers under tension, with a pulling force generated by viscous drag on the string of tensile blobs extending from the surface, countered by the restoring force from the blob at the end of the string in contact with the surface. They developed a theoretical prediction giving a detachment time that scales as N^2 for strong adsorption and overdamped dynamics, and their Monte Carlo simulation results yielded a scaling exponent on N of 1.96 +/- 0.03, while their Langevin-like simulation which they describe as underdamped, yielded a scaling exponent of 1.75 +/- 0.1 [14]. In a later study (2014) which included hydrodynamic interactions (HI) among polymer beads via dissipative particle dynamics, they found HI did not have a significant effect on the forced desorption process.[15]

Mökkönen, et al. (2015) calculated the rate for a 1D ideal bead-spring polymer to translocate from one basin to another in a symmetric, quartic (i.e., given by a fourth order polynomial) double-well potential. [16] After using the "nudged elastic band method" to find the saddle point as the maximum energy point along the minimum energy path, they used harmonic transition state theory with corrections and found close agreement with brute-force Brownian dynamics and Langevin dynamics simulation. Mökkönen, et al. (2016) further improved their calculation method with a re-crossing correction and found it was more computationally efficient than forward flux sampling for achieving an equal degree of uncertainty in the rate calculation. Park and Sung showed that in such a double-well system, the activation energy reaches a plateau when $N > N_C$ where N_C is a critical polymer size above which the transition state ceases to be a coil and is instead a stretched chain reaching from basin to basin.[17,18] These results for escape from one half of the double-well potential may have implications for polymer escape from highly convex surfaces (e.g. a nanoparticle) whose curvature leads to a maximum free energy followed by a decreasing free energy with increasing radial distance far from the surface, rather than a plateau as in desorption from a planar surface. For desorption from a flat surface, because the free energy should reach a plateau for the desorbed state, there would be no such N_C such that a polymer with $N > N_C$ can span two thermodynamically favorable basins.

This review exposes a fundamental gap in the literature, as no published work analyzes the desorption of isolated chains in the absence of flow. We aim to fill this gap using our array of capabilities.

4.2 Forward flux sampling: and analysis of correlation error

4.2.1 Forward flux sampling method

To compute the desorption rate, we use forward flux sampling.[19,20] In this method, a reaction coordinate $C(\boldsymbol{x})$ is defined where $\boldsymbol{x}$ is the microstate, which is the instantaneous vector of particle positions and velocities. In this work, because the dynamics are in a non-inertial regime, we take the microstate to be specified by the configuration of the polymer chain, i.e. $\boldsymbol{x}$ is a vector of the bead positions only. C will be later defined to reflect the degree to which the chain is adsorbed to the surface. A starting state $\boldsymbol{A}$ and ending state $\boldsymbol{B}$ are each defined by the collection of microstates lying within specified intervals on the reaction coordinate C. We want to know the rate of transitions from $\boldsymbol{A}$ to $\boldsymbol{B}$, $k_{A\to B}$. The *splitting* technique oversamples trajectories which advance toward $\boldsymbol{B}$ by passing through intermediate values of C, which we call *gates,* denoted λ_i, so that arrival at $\boldsymbol{B}$ can be observed.[21] These *gates* λ_i (elsewhere called barriers, levels, interfaces, etc.) are defined such that $\lambda_0 \geq \lambda_1 \geq \lambda_2 \geq \cdots \geq \lambda_n$. When a trajectory crosses a gate λ_i, it can be split, whereby replicas of the observed microstate at λ_i are made. The replicas' ensuing trajectories diverge due to the simulation's stochastic nature, and some will travel farther along the reaction coordinate C than others. In forward flux sampling, trajectories that are split at λ_i are used to calculate the advancing probability $P(\lambda_{i+1} \mid \lambda_i)$, which is the probability of reaching λ_{i+1} before returning to λ_0, having started as a random representative of the *entrance distribution* at λ_i. For a system at equilibrium, the entrance distribution can be defined by starting from the equilibrium ensemble of microstates at λ_i, tracing the microstates back in time, and discarding all but those which cross λ_0 more recently than either re-crossing λ_i or crossing λ_{i+1}. Forward flux sampling generates samples (of observed microstates) of the entrance distribution at each level, but due to the replication of microstates in splitting, samples may contain correlated microstates (i.e., "familial correlation"), which can bias $P(\lambda_{i+1} \mid \lambda_i)$. We discuss this possibility later. With the rate of a more frequent process than $\boldsymbol{A} \rightarrow \boldsymbol{B}$ such as the first passage from $\boldsymbol{A}$ to λ_1, $k_{A\rightarrow\lambda_1}$, and with the advancing probabilities $P(\lambda_{i+1} \mid \lambda_i)$, assuming that sampling is thorough and unbiased the rate of the overall process can be expressed as

$$k_{A\rightarrow B} = k_{A\rightarrow\lambda_1} \prod_{i=1}^{i=n-1} P(\lambda_{i+1} \mid \lambda_i) \tag{7}$$

if we define the starting state $\boldsymbol{A}$ as the set of adsorbed microstates and the ending state $\boldsymbol{B}$ as the set of desorbed microstates, i.e

$$\boldsymbol{A} = \{\boldsymbol{x} \in \mathbb{R}^N \mid C(\boldsymbol{x}) \geq \lambda_0\}$$

$$\boldsymbol{B} = \{\boldsymbol{x} \in \mathbb{R}^N \mid C(\boldsymbol{x}) \leq \lambda_n < 1\}$$

The quantities in Equation 7 might not be fully specified without some additional information about the initial distribution in $\boldsymbol{A}$. If mixing of phase space density in $\boldsymbol{A}$ is very fast relative to $\boldsymbol{A} \rightarrow \boldsymbol{B}$ then $k_{A\rightarrow B}$ should be relatively insensitive to the distribution within $\boldsymbol{A}$. However, if mixing in $\boldsymbol{A}$ is not fast relative to $\boldsymbol{A} \rightarrow \boldsymbol{B}$, as seems to be the case experimentally, given the non-exponential distribution of waiting times, then the initial distribution in $\boldsymbol{A}$ can be important. And even if mixing in $\boldsymbol{A}$ is fast relative to $\boldsymbol{A} \rightarrow \boldsymbol{B}$, in forward flux sampling, due to the splitting of paths at each λ_i, it is rather important to consider whether mixing in $\boldsymbol{A}$ is fast relative to $\boldsymbol{A} \rightarrow \lambda_1$.

Otherwise, the measurement of $k_{A\rightarrow\lambda_1}$ and the advancing probabilities can be biased by the initial configuration in $\boldsymbol{A}$. To circumvent potential slow mixing in our state $\boldsymbol{A}$ (the adsorbed state) in this work, we measured $k_{A\rightarrow\lambda_1}$ and collected microstates at λ_1 for a large number of independent configurations starting in $\boldsymbol{A}$.

To set each value λ_i on-the-fly, a relatively small number (e.g. 200) of observed microstates at λ_i are split and trajectories are launched as *trials* run solely to scout the landscape and help in the selection of the next gate. From this limited number of trial trajectories, λ_{i+1} is positioned so that a moderate fraction (e.g. 10%) of the trials would have arrived at λ_{i+1} before returning to λ_0. Once λ_{i+1} is selected, the trial runs can be discarded, and a much larger number of splits (e.g. 5000) are made which are launched as *attempts* to reach λ_{i+1} after λ_{i+1} has been defined. Approximately 500 of the 5000 attempts would be expected to reach λ_{i+1}. The "attempts" are trajectories whose success statistics are used to compute $P(\lambda_{i+1} \mid \lambda_i)$.

This is the basis of forward flux sampling. In the original formulation described by Allen, Frenkel, and ten Wolde, the *attempts* to reach level *i+1* were initiated from microstates chosen at random from the pool of observed microstates at level *i*. This approach is known as *random assignment* or *random selection*.[20,22] However, random assignment of the *M* attempts ("offspring") from observed microstates at each level can exacerbate the problem of "genetic drift" by randomly denying some observed microstates any attempts. For example, if 1500 attempts were randomly assigned to 500 observed microstates at level *i*, then 25 microstates at each level would be randomly wiped out by assignment of zero attempts, on average. An alternative selection method that eliminates the genetic drift due to random assignment is called *fixed assignment* in which each microstate at level *i* is assigned the same number of attempts, except for any remainder after division, in which case the remaining attempts are assigned to the level *i* microstates at random.

Fixed assignment is more equitable in assigning attempts, and it can be used without introducing any bias.[22] We know of no downside to using fixed assignment, and we believe it should always be preferred to random assignment. This point does not seem to be generally appreciated in the FFS literature. We note that fixed assignment does not eliminate genetic drift entirely, because the number of *successful* attempts will still fluctuate randomly, but genetic drift is reduced relative to that occurring in random assignment of attempts.

4.2.2 Error analysis accounting for correlations

We briefly consider two simple statistical models to estimate familial correlation in forward flux sampling. In the first, the number of successes is taken to depend only on the number of attempts assigned to microstate *j* at level i and the advancing probability for the *i*th level, p_i.

$$n_{i,j}^{+} = \text{Binomial}\left(\mathrm{n}_{i,j}, p_i\right) \tag{8}$$

where $\mathrm{n}_{i,j}$ is the number of attempts at level *i* and $n_{i,j}^{+}$ is the number of successful attempts. This model is overly simple because it neglects the fact that certain microstates *j* are advantaged relative to others. If, on the other hand, we allow that each configuration (i.e., microstate) *j* has its own advancing probability $p_{i,j}$, then we instead have

$$n_{i,j}^{+} = \text{Binomial}\left(\mathrm{n}_{i,j}, p_{i,j}\right) \tag{9}$$

A second relatively simple model for $p_{i,j}$ is the Beta distribution $p_{i,j} \sim \text{Beta}(\alpha_i, \beta_i)$ where the Beta distribution is defined on the interval [0, 1] and depends on the distribution shape parameters α_i and β_i. The Beta distribution allows for some microstates *j* to have advantaged attempts which are more likely to succeed in advancing to the next level. Although the simple statistical model in Equation 9 combined with Beta-distributed $p_{i,j}$ yields advantaged microstates with variable $p_{i,j}$, it lacks a mechanism for heritable advantage, in which a microstate *j* with a high probability to advance $p_{i,j}$ produces a microstate at the next level that also possesses a high probability to advance. A statistical model could be cooked up that yields some heritable advantage and familial correlation in an ad hoc manner, but it would require even more arbitrary modeling decisions and the advantage heritability may behave very differently than the full computational-physical model. Instead, we can identify the number of *uncorrelated* estimates of p_i at each level and use the standard error of the mean to quantify the uncertainty in our estimate for p_i. One approach follows for the standard error of the mean based on estimates of p_i.

$$\sigma_{p_i} = \sqrt{\frac{1}{\left|\mathcal{G}_i^{(L)}\right|\left(\left|\mathcal{G}_i^{(L)}\right| - 1\right)} \sum_{g \in \mathcal{G}_i^{(L)}} \left(p_i^{(L)} - \frac{1}{\left|\mathcal{M}_{i,g}\right|} \sum_{j \in \mathcal{M}_{i,g}} p_{i,j}\right)^2} \qquad (10)$$

where $\mathcal{G}_i^{(L)}$ is the set of *smallest uncorrelated descendant groups* at level i and $\mathcal{M}_{i,g}$ is the set of observed microstates in group g at level i. $|S|$ above denotes the size of a set S. We use the following four paragraphs and Equations 11-13 to construct the definition for the term *smallest uncorrelated descendant groups*.

First we define *descendant groups*. At each level, forward flux sampling yields a set of observed microstates $\mathcal{M}_i$. By looking back *n* levels, we can group together all microstates at *i* that have a common ancestor at some previous level *i-n*. If $n = 1$, all microstates will be in a group with their siblings only and with no other microstates. For $n > 1$, all microstates will be in a group with their siblings and their *(n-1)*th cousins and no other microstates. This is illustrated in Figure 4-1. We use such groups of descendants at each level, which we henceforth refer to as *n**th-order descendant groups*, to check for intragroup correlation relative to the entire sample of microstates at some level.

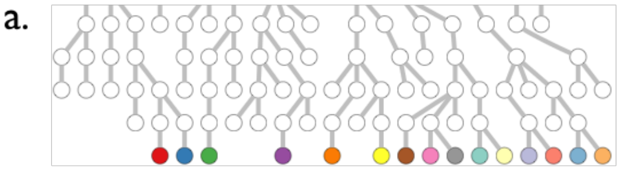

Number of microstates: 15

1st-order descendant groups: 11

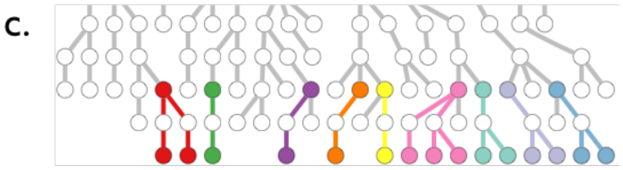

2nd-order descendant groups: 9

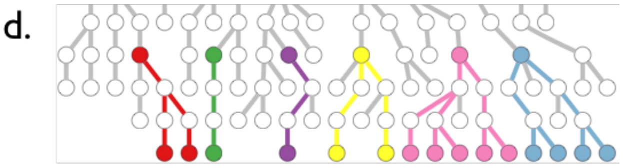

3rd-order descendant groups: 6

Figure 4-1: Microstates (circles) are colored in the bottom row by descendant group. Each row represents a level, and each circle corresponds to an observed microstate at the level. The common nth-order ancestor microstate of each group is also colored, and the lineage paths are colored as well. Parts b, c, d show the 1st, 2nd, and 3rd-order descendant groups.

We next define the measure of intragroup correlation for the descendant groups. The descendant groups may be correlated for values of n up to some limit, at which point the correlation falls below a threshold, such as e^{-1}. To measure intragroup correlation, we adapt Fisher's *intraclass correlation coefficient*.[23] We calculate intragroup correlation in $p_{i,j}$ for the n^{th}-order descendant groups as,

$$r_i^{(n)} = \frac{|\mathcal{M}_i|}{\left|\mathcal{P}_i^{(n)}\right|} \frac{\sum_{(j,k)\in\mathcal{P}_i^{(n)}} \left(p_{i,j} - p_i^{(n)}\right)\left(p_{i,k} - p_i^{(n)}\right)}{\sum_{j\in\mathcal{M}_i} \left(p_{i,j} - p_i^{(n)}\right)^2} \qquad (11)$$

where $r_i^{(n)}$ is the intragroup correlation, and $\mathcal{P}_i^{(n)}$ is the set of all intragroup microstate pairs for the n^{th}-order descendant groups at level *i*. (Each intragroup microstate pair has two microstates that are in the same group, but $\mathcal{P}_i^{(n)}$ includes the intragroup microstate pairs for all *nth*-order descendant groups at level *i*, i.e. the number of intragroup pairs in the bottom level of Fig. 4-1d is 1+0+0+1+10+6=18.) Also, $p_i^{(n)}$ is the average advancing probability for level *i* calculated with the following equation:

$$p_i^{(n)} = \frac{1}{\left|\mathcal{G}_i^{(n)}\right|} \sum_{g \in \mathcal{G}_i^{(n)}} \frac{1}{\left|\mathcal{M}_{i,g}\right|} \sum_{j \in \mathcal{M}_{i,g}} p_{i,j} \tag{12}$$

Here, the pre-averaging over the uncorrelated microstates within each group removes undue weight from large descendant groups whose observed microstates are potentially correlated. Finally, we can identify the smallest uncorrelated descendant groups $\mathcal{G}_i^{(L)}$ as the L^{th}-order descendant groups where

$$L = \min\left\{n \mid r_i^{(n)} \leq \frac{1}{e}\right\} \tag{13}$$

A simpler and more conservative approach than the one just described is to assume that *any* common ancestor leads to correlation between descendants. Both types of error bars are shown as 95% confidence intervals in Figures 4-7 and 4-8. The very thick error bars are based on the standard error of the mean with the number of independent estimates of p_i at each level based on the smallest uncorrelated descendant groups. The thin error bars are based on the more conservative standard error of the mean with number of independent estimates of p_i at each level based on the number of groups which shared no common ancestor.

4.3 Modeling details

In this section, we define the adsorbed state, the interaction potential, and other simulation parameters. We also describe the algorithmic details of simulation setup and analysis.

4.3.1 Contact number and polymer-wall potential

Our adsorbed state is defined in terms of the wall contact number C, and the contact number is defined in terms of a continuous switching function of the distance z from the wall.

$$s(z) = \frac{1 - \left(\frac{z - d_0}{r_0}\right)^n}{1 - \left(\frac{z - d_0}{r_0}\right)^m} \tag{14}$$

where $d_0 = 0.35$ nm, $r_0 = 0.7$ nm, $n = 6$, $m = 14$. A horizontally symmetric function results if n and m are even; then m must be larger than n for the function to have a maximum at 1 and minimum at 0, n is made large enough to yield a smooth plateau, d_0 and r_0 are chosen to shift and size the plateau, and m is increased to yield a more rapid cutoff. These chosen parameters produced the switching function shown in Figure 4-2 with a dashed line that switches smoothly from 1 at the bottom of the polymer-wall energy well, which is at d_0, to 0. We calculated s using the Plumed plugin and its switching function of rational type. Then the contact number is,

$$C = \sum_{i=1}^{N} s(z_i) \tag{15}$$

where z_i is the z component of the position of bead i, and N is the number of beads in the chain. We defined the desorbed state as $C \leq 10^{-5}$. This was sufficient to ensure the polymer upon reaching the final state was in a random coil configuration rather than remaining deformed from its prior adsorption to the wall. To model the wall, we use the Steele 10-4-3 potential, which has been used previously for simulation of polymer at a fluid-solid interface.[5]

$$V_W(z; \sigma_{PW}, \epsilon_{PW}) = 2\pi\epsilon_{PW}\left[\frac{2}{5}\left(\frac{\sigma_{PW}}{z}\right)^{10} - \left(\frac{\sigma_{PW}}{z}\right)^{4} - \frac{\sqrt{2}\sigma_{PW}^{3}}{3\left(z + \left(\frac{0.61}{\sqrt{2}}\right)\sigma_{PW}\right)^{3}}\right] \tag{16}$$

where z is the distance of a bead from the wall, and σ, ϵ are the bead-wall interaction parameters.

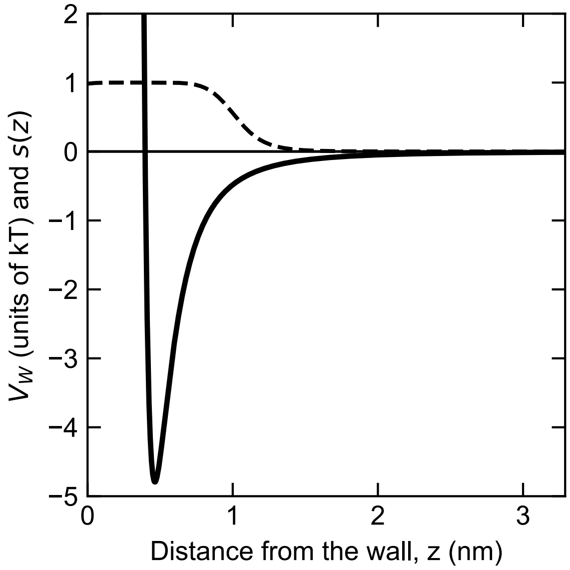

Figure 4-2: Switching function s(z) weights the degree to which a monomer counts as "adsorbed," thereby adding to C (dashed) and monomer-wall potential V_W for $\epsilon_{PW} = 1$ kBT (thick). Zero potential is plotted as the thin, horizontal line.

4.3.2 Langevin equation of motion and polymer models

We ran simulations in LAMMPS. We used the *real* units scheme that operates with time in femtoseconds, length in Å, and energy in kcal/mole. We converted length units to nm and energies to k_BT for publication. Polymer configurations were evolved using the Langevin equation of motion:

$$m\ddot{\boldsymbol{x}}_i = \nabla_{x_i}V - \frac{m}{\tau}\dot{\boldsymbol{x}}_i + \boldsymbol{R} \tag{17}$$

with a damping parameter t_{damp} of 250 fs, and a bead mass m of 45 g/mole. This latter input value was a typographical error in the simulation, since the repeat unit of PEO has a mass of 44 g/mole, but the mass is irrelevant except for its role in setting the diffusivity, since we verified that we were in a non-inertial dynamics regime. The acceleration and velocity of bead i are $\ddot{\boldsymbol{x}}_{\boldsymbol{i}}$ and $\dot{\boldsymbol{x}}_{\boldsymbol{i}}$. The random force is given by R, which is sampled in accordance with the fluctuation-dissipation theorem and a temperature of $T = 300$ K. The conservative force on particle i is given by the gradient of the potential $-\nabla_{x_i} V$. The potential V is composed of bead-bead interactions, bead-wall interactions, and bond stretch, bending, and torsion-like potentials, and is given by

$$V = \sum_{i \neq j} V_{LJ}\left(r_{i,j}, \sigma_{PP}, \epsilon_{PP}\right) + \sum_{i=1}^{N} V_W\left(z_i; \sigma_{PW}, \epsilon_{PW}\right) + \sum_{i=1}^{N-1} k_b\left(r_{i,i+1} - l_b\right)^2 + \sum_{i=1}^{N-2} k_A\left(\theta_{i,i+1,i+2} - \theta_A\right)^2 + \sum_{i=1}^{N-3} k_D\left(r_{i,i+3} - r_D\right)^2 \tag{18}$$

where σ_{PP}, ϵ_{PP}, σ_{PW}, ϵ_{PW}, k_b, l_b, θ_A, k_D, and r_D are model parameters, $r_{i,j}$ is the distance between bead i and bead j, and $\theta_{i,j,k}$ is the bending angle formed by beads i, j, k. V_{LJ} is the standard Lennard Jones interaction potential between beads. The parameter values for the chain models considered are in Table 1. Unless otherwise noted, $l_b = 0.33$ nm and $k_b = 16000$ kJ/mole. In cases without excluded volume between beads, $\epsilon_{PP} = 0$. In cases with excluded volume, $\epsilon_{PP} = 0.2$ kJ/mole and $\sigma_{PP} = 0.43$ nm. In cases described as freely-jointed, $k_A = 0$, whereas in cases described as freely-rotating, $k_A = 2000$ kJ mole^{-1} radian^{-1} and $\theta_A = 111.58°$. θ_A was chosen to yield a persistence length of 1 for an ideal freely-rotating chain. σ_{PP}, ϵ_{PP}, and l_b were adopted from a coarse-grained model for PEO, and k_b and k_A were chosen to approximate stiffness while remaining numerically stable.

Table 1: Parameter values for the chain models considered. N/A means not applicable – that the value was irrelevant because its potential was set to zero. A blank space means the value was varied. The double quote means the value is repeated from the cell above. N, ϵ_{PW} are not listed in the table because they were allowed to vary for each chain model.

	nm	kJ/mol	nm	kJ/mol/nm 2	nm	kJ/mol/rad 2	deg.	kJ/mol/nm 2	nm
	$\boldsymbol{\sigma_{PP}}$	$\boldsymbol{\epsilon_{PP}}$	$\boldsymbol{\sigma_{PW}}$	$\boldsymbol{k_b}$	$\boldsymbol{l_b}$	$\boldsymbol{k_A}$	$\boldsymbol{\theta_A}$	$\boldsymbol{k_D}$	$\boldsymbol{r_D}$
FJC	N/A	0	0.47	16000	0.33	0	N/A	0	N/A
FRC	"	"	"	"	"	2000	"	"	"
FJC+EV	"	0.2	"	"	"	0	"	"	"
FRC+EV	"	"	"	"	"	2000	112	"	"
FRC+EV+D	"	"	"	"	"	“	"	60	0.6

We verified that the Lennard-Jones excluded volume interaction was sufficient to prevent chains from crossing each other. The parameters except σ_{PP} and ϵ_{PP} were borrowed from a Dry Martini model for polyethylene oxide (PEO) which had the correct dependence of gyration radius on N for a PEO polymer.[24]

The mobility of an isolated bead is given by the inverse friction coefficient $\mu_1 = \zeta^{-1} = \frac{t_{\text{damp}}}{m}$. Using the Einstein relation, the monomer diffusivity is given by $D_1 = \mu_1 k_B T = \frac{t_{\text{damp}}}{m} k_B T$. At low ζ, the molecule's momentum will decay slowly, and the molecule may oscillate within a potential well. At high ζ, the molecule's dynamics may be overly sluggish, and simulation performance suffers needlessly. Klimov and Thirumalai found that folding rate in simulations of certain small polypeptides increases linearly with friction coefficient ζ at low ζ, reaches a maximum at intermediate ζ, and decreases as ζ^{-1} at high ζ.[25] The decrease in folding rate with increasing ζ at high ζ is an intuitive result of increasing friction in overdamped dynamics, whereas the less intuitive increase of folding rate with increasing ζ at low ζ may be attributable to the increasing strength of thermal fluctuations with ζ due to the fluctuation-dissipation theorem. At extremely low ζ, although a particle feels little drag, it also receives weaker thermal kicks, which are needed to attempt barrier crossings.

A primary concern of ours was to avoid results that were sensitive to small changes in bead mass m and bending constant k_b. At coarse-grained scales in water, we expected inertial effects to be minimal, so we ensured that desorption times were in the non-inertial scaling regime, such that desorption times scaled as ζ^{-1}.

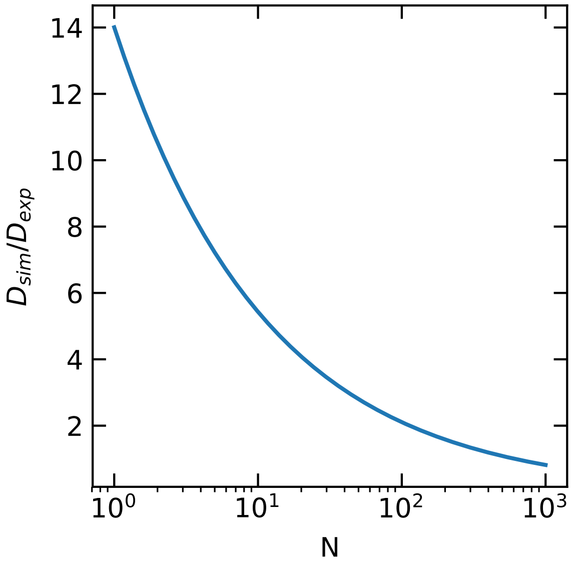

Figure 4-3: Ratio of simulation diffusion coefficient D_{sim} to “experimental” diffusion D_{exp} coefficient as a function of N.

This serves as the conversion factor to convert simulation time to real time. To compare times between the simulation results and the experimental results, one can scale from simulation time t_{sim} to experimental time t_{exp} using $t_{\text{exp}} = t_{\text{sim}} \frac{D_{\text{sim}}}{D_{\text{exp}}}$, where D_{sim} and D_{exp} are the self-diffusion coefficients of a polymer coil in solution for simulation and what is expected in experiment, respectively. Given our fixed damping time $t_{\text{damp}} = 250$ fs, the dependence of D_{sim} on N is fixed and has Rouse ($D_{\text{sim}} \propto N^{-1}$) scaling, i.e. $D_{\text{sim}}(N) = \frac{D_1}{N}$, as opposed to the experimental $D_{\text{exp}} \propto N^{-0.6}$ scaling expected for a polymer in a good solvent. This means that the time scaling factor $\frac{D_{\text{sim}}}{D_{\text{exp}}}$ depends on N. The time scaling factor varies between 14.0 and 0.816

between $N = 1$ and $N = 1000$, respectively. This factor is plotted in Figure 4-3. For the $N = 50$ polymer in simulation we observe D_{sim}= 278 μm^2/s whereas interpolating from the diffusion coefficient for PEO in water using a table in the SI of Skaug et al. we find D_{exp}= 99 μm^2/s. This means, for the $N = 50$ polymer, that simulation times should be increased by a factor of 2.8 (or rates should be decreased by a factor of 2.8) to compare with the experiments in Skaug et al. In the results section, we plot the dimensionless $\frac{t_{\text{sim}} D_{\text{sim}}}{R_g^2}$, so multiplying this dimensionless quantity by the real $\frac{R_g^2}{D_{\text{exp}}}$ yields the real time t_{exp} corresponding to the simulated chain.

4.3.3 Equilibrating and adsorbing polymer coils

Random polymer configurations were generated for all model types in Table 1 by first randomly selecting and rotating bonds. Detailed balance was not respected in this process due to the bending potential, excluded volume potential, and pseudo-dihedral potential that are imposed on many of the simulated chains, so the set of initial configurations was not necessarily an equilibrium sample. Each configuration was then evolved in LAMMPS with Langevin dynamics, the end-to-end distance autocorrelation time τ_{e2e} was calculated, and configurations were saved at intervals of $2\tau_{e2e}$. The resulting nearly independent coil configurations were then transplanted into a simulation box with the wall potential described above, and they were translated along the z direction to bring one of their beads to a *z* position of 0.2 nm, with the remaining beads at larger z values. The configurations were then evolved using Langevin dynamics until the chain center of mass had either moved 12 nm from the wall, 90% of its beads were adsorbed, or a maximum time in ps equal to $100N$ had elapsed, which proved to be an efficient method of generating adsorbed chains to be used as starting states for the FFS simulation. Once the simulation stopped, if at least 10 beads or 10% of beads were in contact with the wall, the configuration was saved as a pre-adsorbed configuration to be used in forward flux sampling of the desorption process. This process of equilibration followed by adsorption was controlled with a Python script utilizing MDAnalysis and calling LAMMPS with the Plumed plugin.

4.3.4 Other forward flux sampling details

We implemented forward flux sampling as outlined in the introduction with a control script in Python which managed LAMMPS sessions with the Plumed plugin. The control script would initiate a LAMMPS run whenever the number of active LAMMPS sessions dropped below the number of available cores, allowing the operating system to schedule the CPUs rather than binding each session to a core.

The $\boldsymbol{B}$ or end basin in every case was defined as $C < \lambda_n = 10^{-5}$, the $\boldsymbol{A}$ or starting basin was defined as $C \geq \lambda_0 = \langle C \rangle_{\text{ads}} - \sigma_{C,\text{ads}}$, and the first level $\lambda_1 = \langle C \rangle_{\text{ads}} - 2\sigma_{C,\text{ads}}$, where $\langle C \rangle_{\text{ads}}$ is the average C calculated over 100 initial runs starting from 100 independently pre-adsorbed microstates and $\sigma_{C,\text{ads}}$ is the standard deviation of the C values explored by the 100 adsorbed chains. A lower bound of 1 was set on λ_0 and λ_1 to avoid the algorithm setting $\lambda_0 < \lambda_n$ or even $\lambda_0 < 0$ in the case of very weakly adsorbing chains. For all intermediate levels λ_i with $1 < i < n$, the levels were set on the fly as described in the following paragraph. Aside from these initial runs being used to position λ_0 and λ_1, the initial rate was measured as the number of forward crossings of λ_1 with history traceable to λ_0 more recently than previous crossing of λ_1, summed over all 100 initial runs, and divided by the total time of the 100 runs excluding any time spent in $\boldsymbol{B}$ and time spent transitioning from $\boldsymbol{B}$ to $\boldsymbol{A}$.

We set the levels λ_i on-the-fly as described in the introduction with $M_{\text{trial}} = 200$ trials, each of which ran until either arriving at the destination $C < 10^{-5}$ or the starting level $C > \lambda_0$. The Plumed plugin would calculate C every 10 timesteps and stop the simulation if either threshold had been crossed. The subsequent level λ_{i+1} was set such that 20 of the 200 trial trajectories would have reached it ($p_i = 10\%$). In other words, λ_{i+1} was set to the 10th percentile of the minima of C reached by the trial runs. After setting a level λ_{i+1} based on the trial runs, we then used $M = 5000$ attempts to reach λ_{i+1} from L_i. These attempts would run until arriving either at $C < \lambda_i$ or $C > C_0$. Approximately 500 of the next 5000 attempts would then make it to the next level. The number of successful attempts, i.e. arriving at $C < \lambda_i$, divided by the total number of attempts $M = 5000$, was taken to be p_i.

4.3.5 Analysis of transition paths

We used the networkx Python module to build a directed graph that recorded microstates and trajectories as nodes.[26] Each observed microstate at the first level was assigned a parent named *start*. The *attempt* trajectories of a microstate were assigned as children of the microstate. Trajectories which failed to reach the next level and returned to the starting basin were assigned *start* as a child. Trajectories which succeeded in reaching the subsequent (but not final) level were assigned the resulting entrance state as a child. Trajectories which reached the final level were assigned a child named *end*. Entrance state nodes in the graph carried information including the level and configurational data file. We used networkx to analyze the graph. For example, we could ask for all paths starting at *start* and ending at *end*, which would return all transition paths as a list of nodes $\{\text{start, entrance state, trajectory, entrance state, …, trajectory, end}\}$. We could then obtain the set of all microstates at level 0 with descendants at level λ_n.

4.4 Results and discussion

We first verified that the damping time $t_{\text{damp}} = 0.25$ ps yielded non-inertial dynamics. We also ensured that the results were insensitive to the change in the bending constant $k_b \to k_b/2$ and bead mass $m \to m/3$. The data verifying this are in the Supporting Information (SI). The main result can be seen in Figure 4-4. The square markers are forward flux sampling results for an $N = 50$ chain for six different values of t_{damp}. The desorption time for $t_{\mathrm{damp}} = 0.25$ ps is the second-from-the-left point. Comparison with the dashed line of log-log slope -1 shows that the results for $t_{\mathrm{damp}} = 0.064$ ps and $t_{\mathrm{damp}} = 0.25$ ps are in the non-inertial regime.

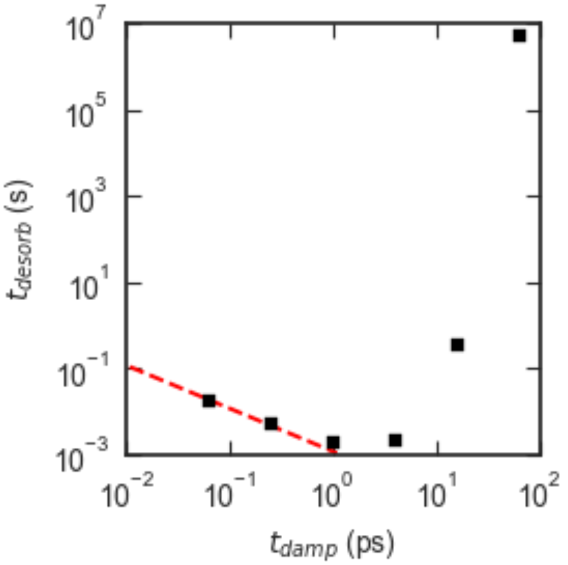

Figure 4-4: Plot of mean desorption times calculated with forward flux sampling for a series of freely jointed chains (FJCs) with N = 50, εPW = 0.6 and with varying tdamp. Black squares are FFS data, and the red dashed line has slope -1 on the log-log plot to illustrate the inverse scaling of t_{desorb} with t_{damp} as expected for non-inertial dynamics.

Desorption times presented in this section are *simulation* times which have not been converted to *experimental* (i.e. real) times. The conversion is discussed in the “Langevin equation of motion and polymer models” section, and the conversion factors for all simulations are within an order of magnitude of unity. In Figure 4-5, we show six snapshots of polymer chains of two different lengths (*N* = 50, 180) and three different polymer-wall interaction energies ($\varepsilon_{\mathrm{PW}}$ = 0.6, 0.4, 0.3). For $\varepsilon_{\mathrm{PW}}$ = 0.6, the adsorbed polymer resembles a pancake, confined to the potential well adjacent to the wall. For $\varepsilon_{\mathrm{PW}}$ = 0.3, the polymer has considerably more configurational freedom. The configurations suggest that the mean-field approach of Equations 3-5 should work for polymers with $\varepsilon_{\mathrm{PW}} \geq 0.6$.

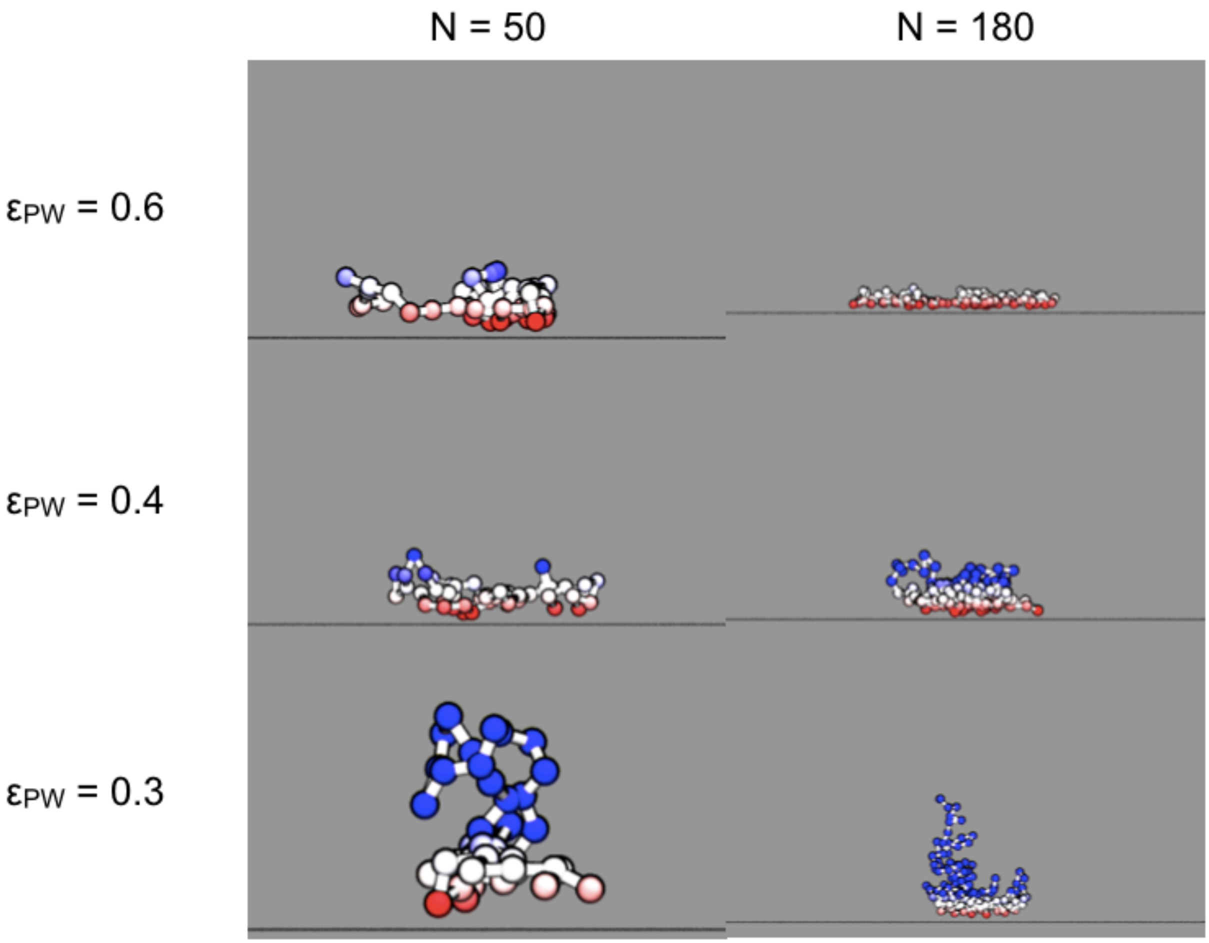

Figure 4-5: Snapshots of chains with three different polymer-wall interaction energies and of two different lengths. These chains did not have excluded volume interactions. Beads are colored on a scale of red (adsorbed) to blue (desorbed), where $z \leq 0.4$ nm is red, $z = 0.7$ nm is white, $z \geq 1$ nm is blue, and intermediate colors are blended.

With the FFS scheme and simulation parameters chosen and verified to produce non-inertial dynamics, we first check the strong mean-field scaling given by Equation 5. Figure 4-6 plots the dimensionless desorption times $\frac{t_{\mathrm{des}}D}{R_g^2}$ for FJC+EV polymers against the degree of polymerization N scaled by V_{MF} as defined in Equation 3. The approach to strong scaling is evident, but strong scaling is apparently not approached except for chains with astronomical mean desorption times, making these chains essentially irreversibly adsorbed. This suggests that the strong-scaling law is not very useful, because it predicts unobservable rates of desorption. We were surprised that even for the ε_{PW}=5.0 data series that the slope hadn't reached the limit shown by the dashed line in Fig. 4-6. Either Equation 5 is invalid or both terms on the right-hand side (RHS) of Equation 4 are required. We attempted to introduce the first RHS term in Eqn. 4 by guessing the confinement size *l*, and the results are presented in the SI. It is, however, possible that this large-N regime might be of interest for desorption assisted by flow or other fields, although in that case the formula, Equation 5, would obviously not be valid, although other simple scaling laws might apply.

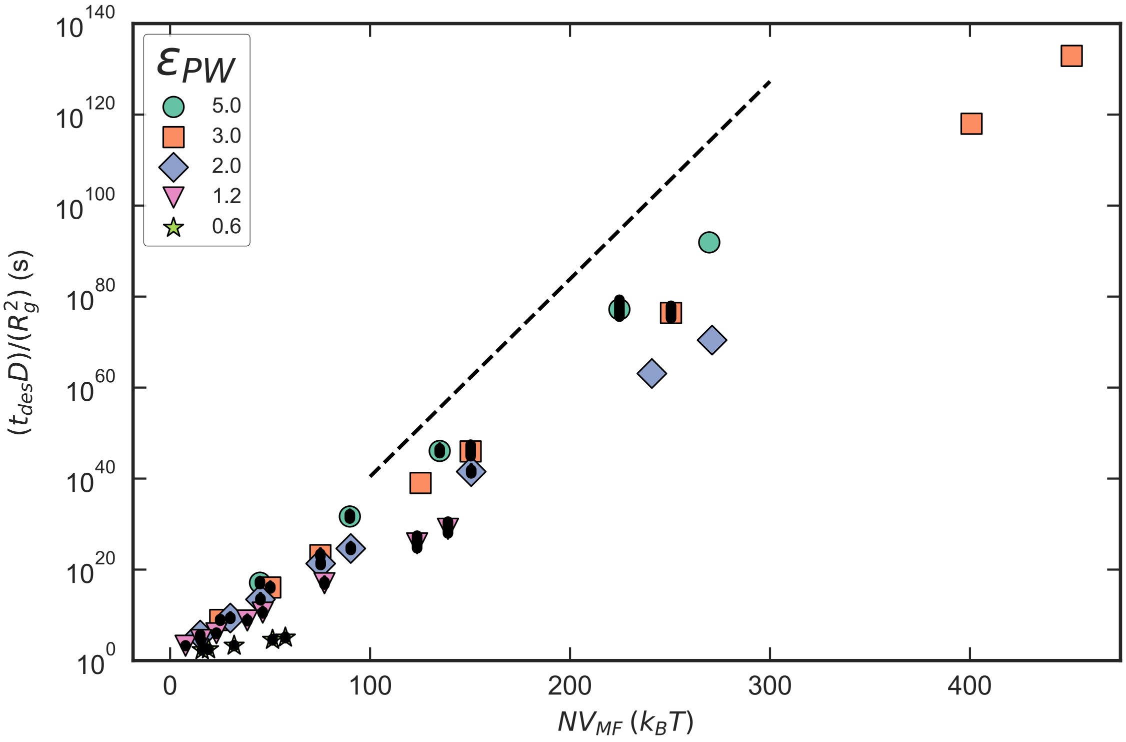

Figure 4-6: Desorption times calculated from FFS for FJC+EV polymers plotted versus $\frac{NV_{MF}}{k_BT}$ for εPP = 3.0, 2.0, and 1.0. The dashed line represents $\frac{t_{des}}{N} = A\, exp\left(\frac{NV_{MF}}{k_BT}\right)$ where A is an arbitrary constant selected for visual clarity. Error bars are omitted because they are smaller than the marker size in almost all cases. Thick lines represent the 95% confidence intervals based on the smallest uncorrelated descendant groups as previously described. Many of these appear as black dots, because the error bars are relatively small compared to the scale of the plot. Thin line error bars representing the error based on the largest descendant groups are not shown in this Figure, because most of the microstates at the final level descended from a single common ancestor microstate, which led to infinite-sized error bars.

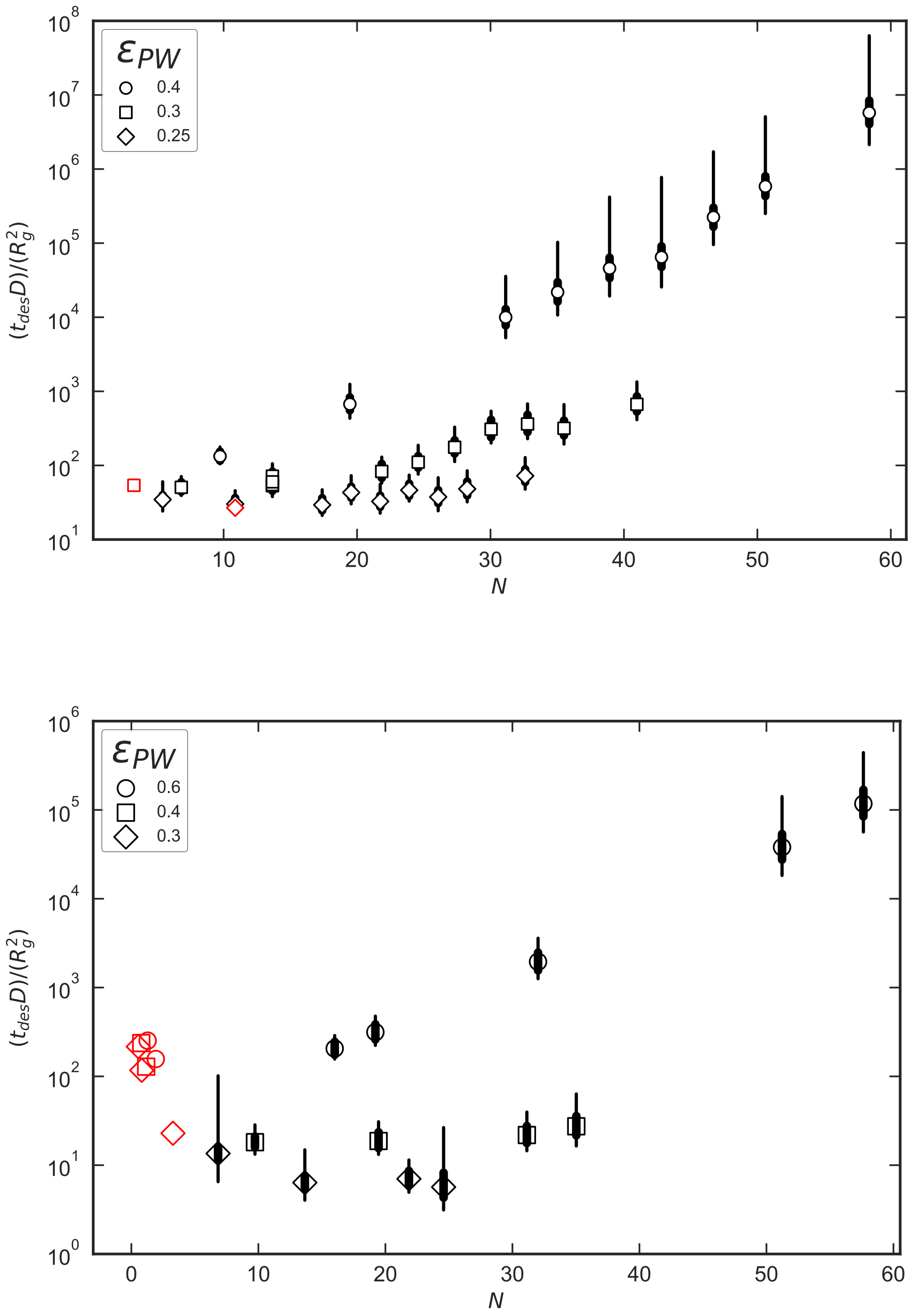

Figure 4-7: Plot of dimensionless desorption time vs. NVMF for FJC (top) and FJC+EV (bottom) polymers. FFS results are colored black and brute-force results are colored red. As chain length within each εPW series increases, the dimensionless desorption times settle into a linear dependence on N (noting that VMF is fixed for each εPW series) For the weakest adsorption, the dimensionless time becomes almost constant. The thick error bars represent the 95% confidence interval calculated from the standard error σ_{p_i} for the smallest uncorrelated descendant groups defined in Equation 10. The thin error bars are based on the largest descendant groups.

Figure 4-7 shows the desorption time for short-chain polymers and low interactions strengths for both FJC and FJC+EV polymers. The *x*-axis again is *N* scaled by V_{MF}, where V_{MF} is constant for each ε_{PW} data series. After the initial *N*-dependence regime before the polymeric configurational penalty takes full effect, a crossover occurs, and desorption time dependence on N becomes exponential, as shown by linear relations in the semilog plots in Figure 4-7. The exception is for the weakest-adsorbing series of polymers in Figure 4-7. In this case, the dimensionless desorption time appears almost independent of *N*. Due to the power law dependencies of R_g and *D*, this implies that t_{des} itself has power law dependence on *N*. Whereas in experiment $t_{des} \propto D^{-1} \propto N^{0.6}$, we observe $t_{des} \propto R_g^2 D^{-1} \propto N^{2\nu+1}$ where $\nu \approx 0.5$ for the FJC without EV and $\nu \approx 0.6$ for the FJC with EV.

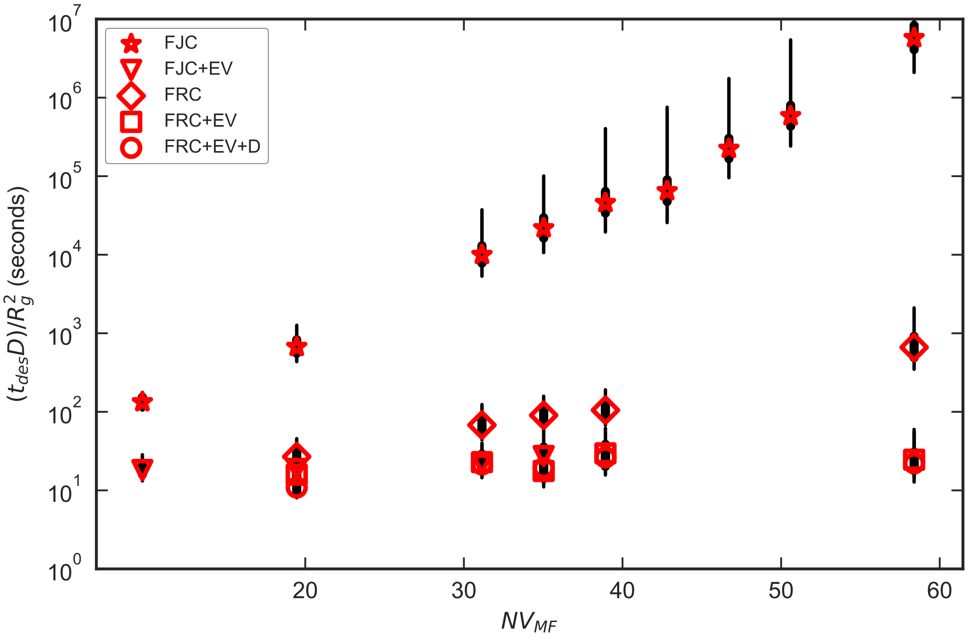

Figure 4-8: Mean desorption times for chains with $\epsilon_{PW} = 0.4$ and varying internal potentials. Legend labels correspond to the parameter definitions in Table 1. FJC: freely-jointed chain, FJC+EV: freely-jointed chain with excluded volume, FRC: freely-rotating chain, FRC+EV: freely-rotating chain with excluded volume, FRC+EV+D: freely-rotating chain with excluded volume and dihedral-like potential. Error bars are drawn as in Figure 4-7.

Figure 4-8 shows dimensionless desorption times on a semilog plot for chains with various internal potentials and $\varepsilon_{PW} = 0.4$. The addition of a bending potential and excluded volume reduce the scaling exponent of the desorption time by more than a factor of 2. The FJC (star) and FRC (diamond) data do not fall on a line on the log-log plot and are evidently still exponential. For the chains with excluded volume (EV), the data appear to be consistent with a power law, though the range of data may need to be extended to higher *N* to make this clearer.

The experimental results of Skaug et al. for the mean polymer desorption time t_{des}, yield two main conclusions. One is that t_{des}lies between 0.1 s and 1 s for N = 45 to N = 1000. The second (not unrelated) conclusion is that the power-law scaling of t_{des} within that range is very weak. It is apparent that a power law scaling in which t_{des} increases from 0.1 s to 1 s over the range N = 45 to N = 1000 is not achievable with our coarse-grained models. After converting the desorption times in Figures 4-7 and 4-8 to real times, the polymers whose desorption times begin to approach the *N*-dependence observed in experiment desorb several orders of magnitude too fast. Our simulation data invariably seem to show that such a weak scaling is consistent with $t_{des} \sim 1$ μs rather than ~ 1 s. The simulation is clearly missing a physical feature of the experiment. Below, we consider three hypothetical missing features that could explain the two experimental observations.

1. The amphiphilicity of the repeat unit: Polyethylene oxide is understood to be amphiphilic on a monomer scale. This has been confirmed in at least one experiment[27] and simulation.[28] *Possibly, the amphiphilic nature of the monomer should be explicitly included in the model. In other words, an atomistic chain with implicit solvent is the minimal polymer model that might yield accurate desorption times.*

2. Atomistic detail of the repeat unit and water: The coarse-grained inter-bead potential in our simulation is the same in solution and at the interface. *Given the hydrogen bonding interaction between surface water molecules and adsorbed PEO, the effective interaction potential between adsorbed monomers could be altered.*
3. Surface heterogeneity: If the surface is unevenly hydrophobic, segments of the chain may become attached to difficult-to-find patches of surface. *If the polymer segments, once desorbed from such patches, could not locate them again before the entire chain desorbs, then the sequential desorption mechanism for the power law desorption time scaling could be justified.*

The first hypothetical explanation could be tested with a finer-grained model for PEO. Given the computational expense of FFS, an implicit solvent for the polymer is a must, but an atomistic implicit-solvent model of PEO is feasible with proper parameterization with respect to solution and adsorbed configurations, with special attention paid to the torsional angle distributions when adsorbed to the surface. The second hypothetical could be investigated with a fully atomistic simulation. The third hypothetical could, in principle, be checked in the laboratory, but a much finer time resolution (and shorter exposure) would be needed. A cursory review of recent TIRFM progress seems to indicate that state-of-the-art time resolution for single-molecule microscopy is at best ~10 ms.[29]

4.5 Summary and conclusions

We computed the desorption times in the absence of an external field or flow for a range of coarse-grained polymer models using forward flux sampling. Our main findings follow:

1. The simple strong-adsorption scaling appears to be asymptotically approached by our simulation results, but the scaling does not become accurate within a time range of physical relevance. This is in line with the comment by Fleer et al. that polymer adsorption under quiescent conditions is generally irreversible. They note that diffusion-controlled desorption alone is extremely slow, but the kinetic barrier to each desorption event can also be astronomical.
2. Excluded volume interactions and bending angle potentials reduce the mean desorption time and also weaken the scaling of t_{des} with *N*.
3. For the coarse-grained chains we studied, the scaling and its prefactor seem to be tightly coupled, such that, with these models, there is no way to achieve the magnitude of t_{des} of stronger adsorbing chains with the weak N-dependence of the weaker-adsorbing chains.

We did not explore the role of persistence length in detail. One reason for this is that we do not expect the persistence length, a property of a coil in solvent, to have a direct role to play in the adsorbed polymer “trains” on the surface. We also emphasize here that our implicit solvent model here does not include hydrodynamic interactions, so the polymer dynamics are Rouse dynamics. Dutta et al. found that hydrodynamic interaction between the polymer and the wall were essential to simulate the shear-induced desorption of isolated polymers. Later study may show that such hydrodynamic interactions are also important to scaling of desorption time under quiescent conditions, but we defer such an investigation for a later study.

Future computational work should investigate more closely the sensitivity of polymer desorption times to the choice of desorption criterion. The independence of $\frac{t_{\text{des}}D}{R_g^2}$ with respect to *N* for the weakest-adsorbing chains suggests that the overall desorption rate could be no longer dominated by a polymer detachment process and instead be dominated by diffusion of the chain through some distance proportional to R_g. This is at odds with the experimental finding which is that $t_{\mathrm{des}}D$ was independent of *N*. More work can be done to understand the desorption rate in this limit and whether the R_g dependence predicted by our simulations is reflective of the Skaug et al. experiments, whether the R_g dependence is an artefact of our method, or whether there is an alternative mode of polymer surface diffusion not yet considered such as heightened mobility after nearly all contacts have been broken. In this work, we used a particular value for the continuous contact number C defined in Equation 15. Although the monomer-wall contact switch function $s(z)$ defined in Equation 14 decays rapidly, as the number of monomers increases, they collectively contribute to C so that longer chains must migrate farther from the surface to satisfy the desorption criterion $C < 10^{-5}$. The effect may be to increase the calculated t_{des} by several times for long chains or lend t_{des} a dependence on some length scale proportional to R_g. The specific criterion may have an especially important effect when studying regimes in which t_{des} scales very weakly with *N*, as it may inflate the scaling of t_{des} with *N* relative to what is observed experimentally. There may also be significant performance advantages to using a hard cutoff for $s(z)$ at which monomers no longer contribute to C, because the FFS algorithm will not have to wait for long chains to migrate as far from the surface.

Another area for future study is how the monomer-scale amphiphilicity of PEO affects the desorption rate. This could be investigated with an implicit-solvent atomistic model of PEO that includes more detailed intramolecular potentials than those studied here, or perhaps a simpler model with alternating attractive and repulsive monomer-surface interactions would suffice. A key question is whether the apparent tight coupling between the t_{des} vs. N scaling and prefactor can be broken. We also intend to study partially sticky copolymer chains. For weakly adsorbing chains which meander to and from the adsorbing surface, it may be possible to effectively coarse-grain the adsorbing trains into individual, sticky beads. Another excellent area for study is the role of polymer or surface heterogeneity on the desorption time and its scaling with chain length.

4.6 Acknowledgments

This research was made possible in part by a grant from BP/The Gulf of Mexico Research Initiative. We also acknowledge the support from the NSF under grant CBET-0853662. Any opinions, findings, and conclusions or recommendations expressed in this material are those of the authors and do not necessarily reflect the views of the National Science Foundation (NSF). Simulations were supported through computational resources and services provided by Advanced Research Computing at the University of Michigan, Ann Arbor.

4.7 References

(1) Skaug, M. J.; Mabry, J. N.; Schwartz, D. K. Single-Molecule Tracking of Polymer Surface Diffusion. J. Am. Chem. Soc. 2014, 136 (4), 1327–1332.

(2) Wang, D.; Hu, R.; Mabry, J. N.; Miao, B.; Wu, D. T.; Koynov, K.; Schwartz, D. K. Scaling of Polymer Dynamics at an Oil–Water Interface in Regimes Dominated by Viscous Drag and Desorption-Mediated Flights. J. Am. Chem. Soc. 2015, 137 (38), 12312–12320.

(3) Fleer, G.; Stuart, M. A. C.; Scheutjens, J. M. H. M.; Cosgrove, T.; Vincent, B. Polymers at Interfaces; Springer Science & Business Media, 1993.

(4) Salehi, A.; Desai, P. S.; Li, J.; Steele, C. A.; Larson, R. G. Relationship between Polyelectrolyte Bulk Complexation and Kinetics of Their Layer-by-Layer Assembly. Macromolecules 2015, 48 (2), 400–409.

(5) Dutta, S.; Dorfman, K. D.; Kumar, S. Shear-Induced Desorption of Isolated Polymer Molecules from a Planar Wall. ACS Macro Lett. 2015, 4 (3), 271–274.

(6) Chechkin, A. V.; Zaid, I. M.; Lomholt, M. A.; Sokolov, I. M.; Metzler, R. Bulk-Mediated Diffusion on a Planar Surface: Full Solution. Phys. Rev. E 2012, 86 (4).

(7) de Gennes, P. G. Polymers at an Interface; a Simplified View. Adv. Colloid Interface Sci. 1987, 27 (3–4), 189–209.

(8) O'Shaughnessy, B.; Vavylonis, D. Irreversible Adsorption from Dilute Polymer Solutions. Eur. Phys. J. E 2003, 11 (3), 213–230.

(9) O'Shaughnessy, B.; Vavylonis, D. Non-Equilibrium in Adsorbed Polymer Layers. J. Phys. Condens. Matter 2005, 17 (2), R63.

(10) Eisenriegler, E.; Kremer, K.; Binder, K. Adsorption of Polymer Chains at Surfaces: Scaling and Monte Carlo Analyses. J. Chem. Phys. 1982, 77 (12), 6296–6320.

(11) Peng, B.; Chen, L.; Que, C.; Yang, K.; Deng, F.; Deng, X.; Shi, G.; Xu, G.; Wu, M. Adsorption of Antibiotics on Graphene and Biochar in Aqueous Solutions Induced by π-π Interactions. Sci. Rep. 2016, 6, 31920.

(12) Netz, R. R.; Andelman, D. Neutral and Charged Polymers at Interfaces. Phys. Rep. 2003, 380 (1), 1–95.

(13) Wang, Y.; Rajagopalan, R.; Mattice, W. L. Kinetics of Detachment of Homopolymers from a Solid Surface. Phys. Rev. Lett. 1995, 74 (13), 2503–2506.

(14) Paturej, J.; Milchev, A.; Rostiashvili, V. G.; Vilgis, T. A. Polymer Detachment Kinetics from Adsorbing Surface: Theory, Simulation and Similarity to Infiltration into Porous Medium. Macromolecules 2012, 45 (10), 4371–4380.

(15) Paturej, J.; Erbas, A.; Milchev, A.; Rostiashvili, V. G. Detachment of Semiflexible Polymer Chains from a Substrate: A Molecular Dynamics Investigation. J. Chem. Phys. 2014, 141 (21), 214902.

(16) Mökkönen, H.; Ikonen, T.; Ala-Nissila, T.; Jónsson, H. Transition State Theory Approach to Polymer Escape from a One Dimensional Potential Well. J. Chem. Phys. 2015, 142 (22), 224906.

(17) Park, P. J.; Sung, W. Dynamics of a Polymer Surmounting a Potential Barrier: The Kramers Problem for Polymers. J. Chem. Phys. 1999, 111 (11), 5259–5266.

(18) Lee, S.; Sung, W. Coil-to-Stretch Transition, Kink Formation, and Efficient Barrier Crossing of a Flexible Chain. Phys. Rev. E 2001, 63 (2).

(19) Allen, R. J.; Valeriani, C.; Wolde, P. R. ten. Forward Flux Sampling for Rare Event Simulations. J. Phys. Condens. Matter 2009, 21 (46), 463102.

(20) L'Ecuyer, P.; Le Gland, F.; Lezaud, P.; Tuffin, B. Splitting Techniques. In Rare Event Simulation using Monte Carlo Methods; Rubino, G., Tuffin, B., Eds.; John Wiley & Sons, Ltd, 2009; pp 39–61.

(21) Adams, D. A.; Sander, L. M.; Ziff, R. M. The Barrier Method: A Technique for Calculating Very Long Transition Times. J. Chem. Phys. 2010, 133 (12), 124103.

(22) Amrein, M.; Künsch, H. R. A Variant of Importance Splitting for Rare Event Estimation: Fixed Number of Successes. ACM Trans Model Comput Simul 2011, 21 (2), 13:1–13:20.

(23) Fisher, R. A. Statistical Methods for Research Workers. 1934.

(24) Wang, S.; Larson, R. G. Coarse-Grained Molecular Dynamics Simulation of Self-Assembly and Surface Adsorption of Ionic Surfactants Using an Implicit Water Model. Langmuir 2015, 31 (4), 1262–1271.

(25) Klimov, D. K.; Thirumalai, D. Viscosity Dependence of the Folding Rates of Proteins. Phys. Rev. Lett. 1997, 79 (2), 317–320.

(26) Hagberg, A. A.; Schult, D. A.; Swart, P. J. Exploring Network Structure, Dynamics, and Function Using NetworkX. In Proceedings of the 7th Python in Science Conference; Varoquaux, G., Vaught, T., Millman, J., Eds.; Pasadena, CA USA, 2008; pp 11–15.

(27) Kim, J.; Opdahl, A.; Chou, K. C.; Somorjai, G. A. Hydrophobic-Interaction-Induced Alignment of Polymers at the Solid/Liquid Interface Studied by Infrared−Visible Sum Frequency Generation. Langmuir 2003, 19 (23), 9551–9553.

(28) Huston, K. J.; Larson, R. G. Reversible and Irreversible Adsorption Energetics of Poly(Ethylene Glycol) and Sorbitan Poly(Ethoxylate) at a Water/Alkane Interface. Langmuir 2015.

(29) Tang, J.; Sun, Y.; Pang, S.; Han, K. Y. Spatially Encoded Fast Single-Molecule Fluorescence Spectroscopy with Full Field-of-View. Sci. Rep. 2017, 7 (1), 10945.

CHAPTER 5

Conclusions and future directions

In the second chapter, we showed how to correctly calculate the surface excess for a non-ionic surfactant, and we showed how it can be integrated with computed surface pressure data to generate the entire sub-micellar adsorption isotherm, which in turn can be used to predict diffusion-controlled desorption dynamics. In the third chapter, we combined the potential of mean force with the diffusivity to model surfactant interfacial dynamics as Markovian diffusion-migration over the distance from the interface to obtain an adsorption rate constant. In the fourth chapter, we used rare event sampling to calculate the desorption rate constant of an isolated homopolymer chain from a wall.

The utility of these methods for quantitative prediction depends on development of accurate force fields which retain their accuracy when modeling the interface between phases. This latter requirement in particular is a challenge due to the continuously varying dielectric constant near the interface, which can influence the effective point charges on each atom through the polarizability. Forcefields like GROMOS, CHARMM, and Amber were primarily developed for biomolecular simulation in water at ambient conditions. In the case of lipids, these forcefields have been optimized to reproduce observable features of lipid monolayers and bilayers. Increasingly refined quantitative agreement is being obtained for lipids even today – see for example work by Javanainen, Lamberg, Cwiklik, Vattulainen, and Ollila (2017) in which the researchers adopt the modern OPC-4 model for water.[1] Despite the ever-improving models for lipids, there is no general recipe for developing highly accurate surfactant force fields. It is not yet understood what the minimally-required features for quantitative predictions are. Several questions need to be answered before these minimal features are known:

- Must polarizability (environmentally-dependent point charges) of the molecule be accounted for?
- Are long-ranged non-Coulombic forces needed?
- Are the autoions of water needed?
- Which model for water should be used?
- Can polydispersity of the surfactant be neglected?

Today there is an increasing focus on quantitative predictions. Industrial researchers prefer a rapid, automated workflow that can generate accurate predictions within days without manual parameterization and prerequisite decision making.[2] Computational tensiometry and other quantitative predictions based on molecular simulation of the interface will not be feasible for industrial application without more basic research to identify the minimally-required physical features for quantitative predictions. The future work most essential to advancing the field lies in this direction.

5.1 References

(1) Javanainen, M.; Lamberg, A.; Cwiklik, L.; Vattulainen, I.; Ollila, O. H. S. Atomistic Model for Nearly Quantitative Simulations of Langmuir Monolayers. *Langmuir ACS J. Surf. Colloids* **2017**.

APPENDIX A

Supplementary information for Chapter 2

A.1 Additional results

A.1.1 Oleic acid (protonated) potentials of mean force

We measured PMFs for protonated oleic acid with the GROMOS 53a6OXY and MARTINI forcefields at the water/hexadecane interface. We found the free energy to transfer oleic acid from bulk alkane to bulk water was 10 k_BT and 19 k_BT for the GROMOS 53a6OXY+D and Martini forcefields, respectively. Despite this large difference in transfer free energies, the free energy differences from water to the PMF minimum were remarkably close, both -23 k_BT. The PMFs are plotted in Figure A-1.

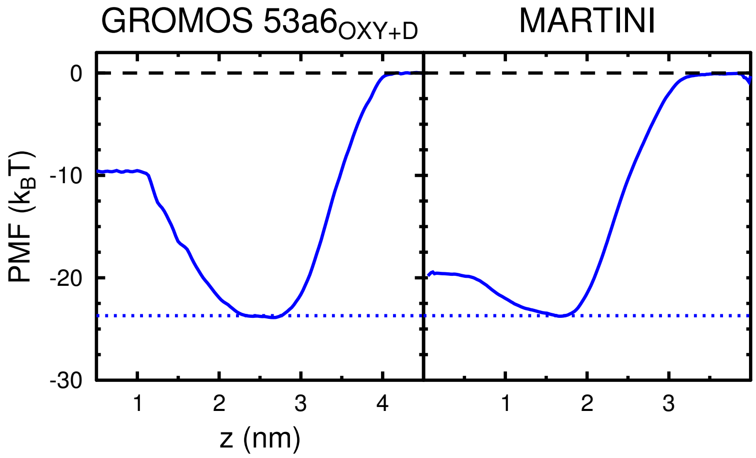

Figure A-1. PMFs of oleic acid at the hexadecane/water interface in the GROMOS 53a6OXY+D and MARTINI forcefields. The horizontal dotted line highlights how close the PMF minima are. PMF minima occur when the tail is removed from water into oil, with the carboxylic acid head remaining in water; z is defined so that to the left is hexadecane, to the right is water.

A.1.2 MARTINI models of hydroxyl-terminal PEG

We measured PMFs for a few oligomers using the hydroxyl-terminal modifications of the Lee et al. and Rossi et al. forcefields. We found that the trends are similar upon increasing oligomer length, and that the hydroxyl-terminal chains adsorb less strongly overall.

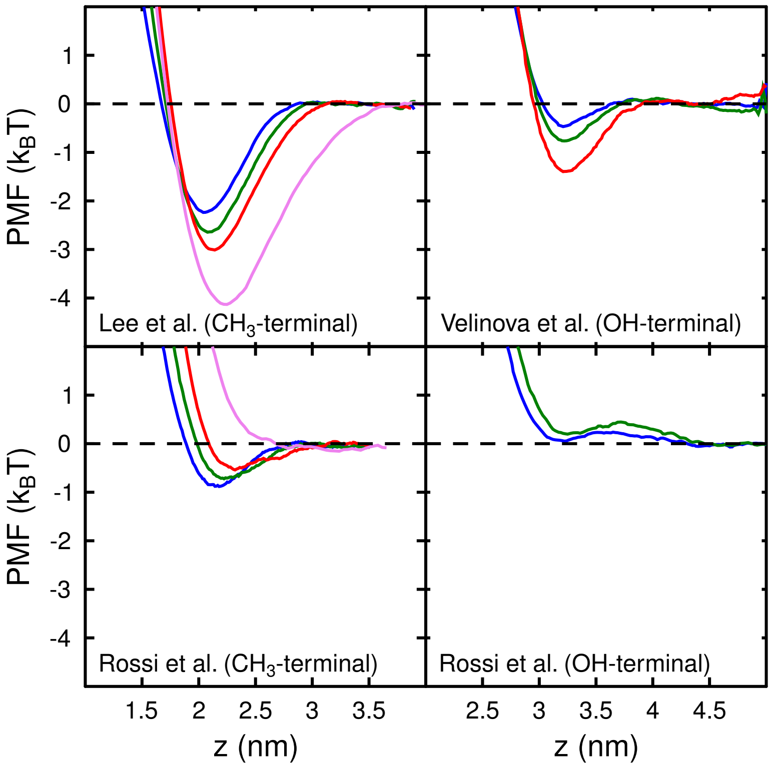

Figure A-2. PMFs of methyl- and hydroxyl-terminal PEG oligomers using MARTINI forcefields by Lee et al., Velinova et al., and Rossi et al.

A.2 Derivations

A.2.1 Derivation of dilute adsorption coefficient from simulation

In this work, we assume a Tween 80 monolayer accounts for the thermodynamic surface excess of Tween 80. The Gibbs-invariant surface excess of a component $i \neq 1$ at a planar interface is given by Radke[1]:

$$\Gamma_i = \Gamma_{i0} - \Gamma_{10}\left(\frac{c_i^\alpha - c_i^\beta}{c_1^\alpha - c_1^\beta}\right)$$

where $\mathit{\Gamma}_i$ is the invariant surface excess of component i, $\mathit{\Gamma}_{i0}$ is the surface excess of component i based on a Gibbs dividing surface at $z = z_0$, ρ_i^α is the volumetric concentration of component i in a bulk phase α.

Let bulk phase $\alpha = w$ be the aqueous phase, let bulk phase $\beta = o$ be the oil phase, let component 1 be water, and let component $i = s$ be the surfactant Tween 80 (assumed to be a single component). We can then rearrange the above equation to

$$\mathit{\Gamma}_s = \mathit{\Gamma}_{s0} - \mathit{\Gamma}_{10} \frac{c_s^w}{c_1^w} \left(\frac{1 - \frac{c_s^o}{c_s^w}}{1 - \frac{c_1^o}{c_1^w}} \right)$$

Because water is nearly insoluble in the oil phase, $c_1^o \ll c_1^w$. Tween 80 is also insoluble in the oil phase in the absence of reverse micelles, so $c_s^o \ll c_s^w$, and we can obtain,

$$\mathit{\Gamma}_s = \mathit{\Gamma}_{s0} \left[1 - \frac{c_s^w}{\mathit{\Gamma}_{s0}} \frac{\mathit{\Gamma}_{10}}{c_1^w} \right]$$

The adsorption coefficient of surfactant $\mathit{\Gamma}_{s0}/c_s^w$ is safely assumed to be many orders of magnitude larger than that of water $\mathit{\Gamma}_{10}/c_1^w$, and so we confirm that $\mathit{\Gamma}_s \approx \mathit{\Gamma}_{s0}$. We calculate $\mathit{\Gamma}_{s0}$ using its definition from Rowlinson and Widom.2

$$\mathit{\Gamma}_{s0} = \int_{-\infty}^{z_0} [c_s(z) - c_s^o]\, dz + \int_{z_0}^{\infty} [c_s(z) - c_s^w] dz$$

where $c_s(z)$ is the local concentration of surfactant, and c_s^o and c_s^w are the bulk concentrations of surfactant in the oil and water phases, and the division between bulk phases is set by a Gibbs dividing surface at $z = z_0$.

We divide by c_s^w to obtain an adsorption coefficient

$$\frac{\Gamma_{s0}}{c_s^w} = \int_{-\infty}^{z_0} \left[\frac{c_s(z)}{c_s^w} - \frac{c_s^o}{c_s^w}\right] dz + \int_{z_0}^{\infty} \left[\frac{c_s(z)}{c_s^w} - 1\right] dz$$

For a surfactant interfacial potential of mean force (PMF) W_Z shifted so that $W_Z = 0$ in the bulk water, we have by the Boltzmann equation

$$\frac{\Gamma_{s0}}{c_s^w} = \int_{-\infty}^{z_0} \left[e^{-\beta W_Z(z)} - \frac{c_s^o}{c_s^w}\right] dz + \int_{z_0}^{\infty} \left[e^{-\beta W_Z(z)} - 1\right] dz \qquad \text{(S1)}$$

From this formula, we can obtain the adsorption coefficient Γ_{s0}/c_s^w from an PMF, assuming the simulation accurately models equilibrium conditions. We seek the dilute-limit "Henry's law" adsorption coefficient for which surfactant molecules do not interact with each other, so a lone Tween 80 molecule at a clean water-oil interface is the correct environment to simulate.

In practice, we do not numerically evaluate the integral from $-\infty$ to $+\infty$. We evaluate over a finite range which encompasses the interface and the contribution from $e^{-\beta W_Z(z)}$ around the

PMF minimum. Since the magnitude of $c_s(z)$ at the interface is many orders greater than c_s^w and c_s^o, positioning of the Gibbs dividing surface z_0 is not needed.

A.2.2 Derivation of dilute adsorption coefficient from Nikas-Mulqueen-Blankschtein (NMB) Theory

In this work, we refer to the "adsorption free energy" parameter in Nikas-Mulqueen-Blankschtein theory as the dilute adsorption free energy. We derive Equation 5 from the manuscript below and verify that the dilute adsorption free energies $\Delta\mu_i^0$ from Nikas, Puvvada, and Blankschtein[3] and $\Delta\mu_i^{\sigma/w,0}$ from Mulqueen and Blankschtein4 have the same relation to the dilute adsorption coefficient, save for a dependence on the units of the adsorption coefficient.

Starting from Equation 5 in Nikas et al.,[3]

$$\mu_i^\sigma = \mu_i^{\sigma,0} + k_B T \left[\ln \frac{x_i^\sigma}{a - \sum_j x_j^\sigma a_j} + \frac{a_i + 2\pi r_i \sum_j x_j^\sigma r_j}{a - \sum_j x_j^\sigma a_j} + \frac{\pi a_i \left(\sum_j x_j^\sigma r_j\right)^2}{\left(a - \sum_j x_j^\sigma a_j\right)^2} \right] + \frac{2}{a} \sum_j B_{ij} x_j^\sigma$$

a is the total area available per adsorbed surfactant molecule, i.e. $\frac{A}{N}$ where A is the total area and N is the total number of surfactant molecules adsorbed to the interface.

a_i is the hard disk area of a surfactant species i based on its hard disk radius r_i

x_i^σ is the mole fraction of surfactant i at the interface, i.e. N_i/N

Firstly, we make simplifications to consider only a single surfactant species. E.g. $x_j^\sigma = 1$ and we rewrite the radii r_i in terms of areas a_i.

$$\mu_i^\sigma = \mu_i^{\sigma,0} + k_B T \left[\ln \frac{1}{a - a_i} + \frac{3a_i}{a - a_i} + \frac{a_i^2}{(a - a_i)^2} \right] + \frac{2}{a} B_{ii}$$

Secondly, we take the dilute limit, such that $a \gg a_i$ and $a \gg B_{ii}$.

$$\mu_i^\sigma = \mu_i^{\sigma,0} + k_B T \ln \frac{1}{a}$$

Thirdly, we recognize that $1/a$ is the quantity N/A which we write as Γ.

$$\mu_i^\sigma = \mu_i^{\sigma,0} + k_B T \ln \Gamma$$

Although the precise definition of Γ with respect to a Gibbs dividing surface or some other thermodynamic formalism

I leave this result for now and turn to the chemical potential write in terms of bulk phase properties. Starting from Equation 6 in Nikas et al.,

$$\mu_A^b = \mu_A^{b,0} + k_B T \left[\ln X_{1A} + X - \sum_{n_A, n_B} X_{n_A, n_B} \right]$$

X_{1A} is the bulk mole fraction of surfactant monomer type A.

X is the bulk mole fraction of surfactant.

X_{n_A, n_B} are the bulk mole fraction of mixed micelles.

Consider only a single surfactant species in the dilute limit well below the critical micelle concentration,

$$\mu_A^b = \mu_A^{b,0} + k_B T\ [\ln X + X]$$

In the dilute limit, $\lim_{X \to 0} X = 0$ but $\lim_{X \to 0} \ln X$ will remain important.

$$\mu_A^b = \mu_A^{b,0} + k_B T \ln X$$

The chemical potentials μ_A^σ and μ_A^b are equal at equilibrium. Setting them equal, we obtain an equation governing equilibrium for a single surfactant in the dilute limit:

$$\mu_A^{\sigma,0} - \mu_A^{b,0} = -k_B T \ln \frac{\Gamma}{X}$$

$$\Delta\mu_i^0 = -k_B T \ln \frac{\Gamma}{X}$$

where Γ is the dimensional surface density and X is the bulk phase mole fraction of surfactant. Furthermore, we can write,

$$\frac{\Gamma}{c_s^w} = c_w^w e^{-\Delta\mu_i^0 / k_B T} \tag{S2}$$

where c_s^w is the concentration of surfactant molecules in bulk water, and c_w^w is the concentration of water in bulk water. This is valid in the dilute limit because $c_s^w \ll c_w^w$ so $\frac{c_s^w}{c_w^w} \approx X$.

Equation 5 in Mulqueen and Blankschtein can be transformed to Equation 5 in Nikas et al. with a simple transformation: divide numerator and denominator by Γ as needed.

$$\mu_i^{\sigma} = \mu_i^{\sigma,0} + k_B T \left[\ln\left(\frac{\Gamma_i}{1 - \sum_{k=1}^{n} \Gamma_k a_k} \right) + \frac{a_i + 2\pi r_i \sum_{k=1}^{n} \Gamma_k r_k}{1 - \sum_{k=1}^{n} \Gamma_k a_k} + \frac{\pi a_i (\sum_{k=1}^{n} \Gamma_k r_k)^2}{(1 - \sum_{k=1}^{n} \Gamma_k a_k)^2} \right]$$

Actually, this doesn't quite get you the same result. There appears to be a typo in the second term in square brackets, and the above should be:

$$\mu_i^{\sigma} = \mu_i^{\sigma,0} + k_B T \left[\ln\left(\frac{\Gamma_i}{1 - \sum_{k=1}^{n} \Gamma_k a_k} \right) + \frac{\Gamma a_i + 2\pi r_i \sum_{k=1}^{n} \Gamma_k r_k}{1 - \sum_{k=1}^{n} \Gamma_k a_k} + \frac{\pi a_i (\sum_{k=1}^{n} \Gamma_k r_k)^2}{(1 - \sum_{k=1}^{n} \Gamma_k a_k)^2} \right]$$

Equation 6 from Mulqueen and Blankschtein gives the chemical potential for a surfactant molecule in the aqueous phase:

$$\mu_i^{w} = \mu_i^{w,0} + k_B T \ln\left(\frac{n_i^w}{n_w^w} \right)$$

where n_i^w is the concentration of surfactant molecules of type i in the aqueous phase and n_w^w is the concentration of water molecules in the aqueous phase. For a single species, n_i^w

Because Equation 5 from Mulqueen and Blankschtein can be transformed to Equation 5 from Nikas et al., it can also be simplified in the dilute limit to Equation S2. Setting the chemical potentials equal,

$$\mu_i^{\sigma,0} - \mu_i^{w,0} = -k_B T \ln \frac{n_w^w \, \Gamma}{n_i^w}$$

Again, we can write

$$\frac{\Gamma}{n_i^w} = n_w^w e^{-\Delta\mu_i^{\sigma/w,0}/k_B T} \tag{S3}$$

and observe by comparison of Equations S2 and S3 that $\Delta\mu_i^0$ and $\Delta\mu_i^{\sigma/w,0}$ from the two papers are functionally equivalent.

Note there is a difference between these adsorption free energies and the value used in the body of this paper. For Mulqueen and Blankschtein, $\Delta\mu_i^{\sigma/w,0} = \mu_i^{\sigma,0} - \mu_i^{w,0}$. We defined it instead $\Delta\mu_i^{\sigma/w,0} = \mu_i^{\sigma,0} - \mu_i^{w,0} + k_B T \ln c_w^w$ which gives $\Delta\mu_i^{\sigma/w,0}$ the simplier relation to the adsorption coefficient, shown in Equations 6, 7, and 9. Comparison with Equation S1 shows that the dilute adsorption free energy can be calculated from the PMF of an isolated surfactant.

A.2.3 Derivation of marginal excess pressure-area work integral in terms of intensive area a

Starting from Equation 4 in Nikas et al.,[3] we make a substitution $\mu_s^{\sigma,0} = \tilde{\mu}_i^{\sigma,0} + k_B T \left(1 + \ln\left(\frac{k_B T}{\Pi_0}\right)\right)$ and $\Pi^{\text{id}} = \Gamma_s k_B T$ and observe that $x_i^\sigma = 1$ for a single component to obtain:

$$\mu_s^\sigma = \mu_s^{\sigma,0} + \ln \Gamma_s - \int_\infty^A \left(\frac{\partial \left(\Pi(A', N_s^\sigma) - \Pi^{\text{id}}(A', N_s^\sigma) \right)}{\partial N_s^\sigma} \right)_{A',T,p} dA'$$

Surface pressure $\Pi(A, N_s^\sigma)$ is a function of the intensive area per molecule $\Pi(A, N_s^\sigma) = \Pi(a)$ where $a = \frac{A}{N_s^\sigma}$. We note that the integral above comes from the expression below:

$$\frac{\partial}{\partial N_s^\sigma} \left[\int_\infty^A \Pi(A', N_s^\sigma) - \Pi^{\text{id}}(A', N_s^\sigma)\, dA' \right]_{A,p,T}$$

The Π-A integral follows a path of constant N_s^σ, and the partial derivative $\frac{\partial}{\partial N_s^\sigma}|_{A,p,T}$ measures the marginal change in that integral upon adding an adsorbed surfactant without changing the area.

$$\int_\infty^A \left(\frac{\partial \left(\Pi(A', N_s^\sigma) - \Pi^{\mathrm{id}}(A', N_s^\sigma) \right)}{\partial N_s^\sigma} \right)_{A',T,p} dA'$$

Our task is simply to transform this expression from extensive coordinates $\{N_s^\sigma, A\}$ to the intensive area a. We will use the differential:

$$A = N_s^\sigma a$$

$$dA = N_s^\sigma da + dN_s^\sigma a$$

The partial derivative is taken along $dA = 0$, so we can use a simple chain rule to transform it:

$$0 = N_s^\sigma da + dN_s^\sigma a$$

$$\frac{\partial a}{\partial N_s^\sigma} = -\frac{a}{N_s^\sigma}$$

$$\left(\frac{\partial \left(\Pi(A', N_s^\sigma) - \Pi^{\mathrm{id}}(A', N_s^\sigma) \right)}{\partial N_s^\sigma} \right)_{A',T,p}$$

$$= \left(\frac{\partial \left(\Pi(A', N_s^\sigma) - \Pi^{\mathrm{id}}(A', N_s^\sigma) \right)}{\partial a'} \right)_{A',T,p} \left(\frac{\partial a'}{\partial N_s^\sigma} \right)_{A',T,p}$$

$$= -\left(\frac{\partial\left(\Pi(A', N_s^\sigma) - \Pi^{\mathrm{id}}(A', N_s^\sigma)\right)}{\partial a'}\right)_{A',T,p} \frac{a'}{N_s^\sigma}$$

Over the integration, we have $dN_s^\sigma = 0$, so the differential area $dA' = N_s^\sigma da'$. When we change the variable of integration, we also change the bounds of integration:

$$A' = \infty \rightarrow a' = \infty$$

$$A' = A \rightarrow a' = a$$

$$\int_\infty^A \dots\ dA' \rightarrow \int_\infty^a \dots\ da'$$

Putting this together, we obtain

$$-\int_\infty^a \left(\frac{\partial\left(\Pi(A', N_s^\sigma) - \Pi^{\mathrm{id}}(A', N_s^\sigma)\right)}{\partial a'}\right)_{A',T,p} \frac{a'}{N_s^\sigma} N_s^\sigma\, da'$$

$$-\int_\infty^a \left(\frac{\partial\left(\Pi(A', N_s^\sigma) - \Pi^{\mathrm{id}}(A', N_s^\sigma)\right)}{\partial a'}\right)_{A',T,p} a' da'$$

Yielding our final expression of the surface chemical potential equation in terms of intensive area.

$$\mu_s^\sigma = \mu_s^{\sigma,0} + \ln \Gamma_s + \int_\infty^a \left(\frac{\partial\left(\Pi(a') - \Pi^{\mathrm{id}}(a')\right)}{\partial a'}\right)_{A',T,p} a' da'$$

A.3 Analysis method details

A.3.1 Dilute adsorption free energy from simulation and its uncertainty

Given the PMF $W_Z(z)$ for an isolated surfactant at a clean water/oil interface, we can calculate the dilute adsorption free energy by comparing Equations 6 and 10.

$$\Delta\mu^{\sigma/w,0} = -k_B T \ln\left[\int_{-\infty}^{z_0}\left[e^{-\beta W_Z(z)} - \frac{c_s^o}{c_s^w}\right] dz + \int_{z_0}^{\infty}\left[e^{-\beta W_Z(z)} - 1\right] dz\right]$$

To obtain the uncertainty in adsorption free energies calculated from PMFs using this equation, we generated 1,000 bootstrapped PMFs with g_wham. These bootstrapped PMFs were vertically shifted such that the average W_Z in the horizontal section was equal to zero. Dilute adsorption free energy $\Delta\mu^{\sigma/w,0}$ was calculated from each vertically-shifted, bootstrapped PMF. Subtracting 1,000 bootstrapped $\Delta\mu^{\sigma/w,0}$ for $C_{12}E_2$ from each of the 1,000 bootstrapped $\Delta\mu^{\sigma/w,0}$ for $C_{12}E_8$, we obtained 1,000,000 $\Delta\Delta\mu^{\sigma/w,0}$ for the difference between $C_{12}E_2$ and $C_{12}E_8$. From this distribution of $\Delta\Delta\mu^{\sigma/w,0}$, we calculated the 2.5 and 97.5 percentiles to determine the 95% confidence interval.

For GROMOS 53a6OXY+D, the lower and upper limits of the 95% confidence interval were 6.77 and 8.14, with a mean of 7.47, so we reported $\Delta\Delta\mu^{\sigma/w,0} = 7.5 \pm 0.7$ kBT.

For MARTINI (Lee et al.), the lower and upper limits of the 95% confidence interval were 1.33 and 1.85, with a mean of 1.58, so we reported $\Delta\Delta\mu^{\sigma/w,0} = 1.6 \pm 0.3$ kBT.

A.3.2 Marginal excess pressure-area work

The pressure-area isotherm is interpolated from pressure-area data using a piecewise function with a sum of exponentials and a 2D vdW-like excluded-area equation of state:

$$\Pi = \left[\begin{array}{ll} p_0 + \sum_{i=1}^{n} p_i e^{-q_i(a-a_0)} & \text{for } a < a_{\text{switch}} \\ \dfrac{k_B T}{a - A} & \text{for } a > a_{\text{switch}} \end{array}\right. \tag{S4}$$

We write the marginal excess pressure-area work (MEPAW) integral

$$\int_{\infty}^{a} \frac{\partial(\Pi(a') - \Pi_{\text{id}}(a'))}{\partial a'}\, a' da'$$

and substitute the piecewise functional form of the $\Pi(a)$ isotherm.

$$\int_{a_{\text{switch}}}^{a} \frac{\partial}{\partial a'}(\Pi_{\text{SoE}}(a'; \{p_i\}, \{q_i\}, a_0) - \Pi_{\text{id}}(a'))\; a' da' + \int_{\infty}^{a_{\text{switch}}} \frac{\partial}{\partial a'}(\Pi_{vdW}(a'; A) - \Pi_{\text{id}}(a'))\, a' da'$$

We evaluate the sum of exponentials piece:

$$\int_{a_{\text{switch}}}^{a} \frac{\partial(\Pi_{\text{SoE}}(a'; \{p_i\}, \{q_i\}, a_0) - \Pi_{\text{id}}(a'))}{\partial a'}\, a' da'$$

$$\int_{a_{\text{switch}}}^{a_2} \frac{\partial\left(p_0 + \sum_{i=1}^{n} p_i e^{-q_i(a'-a_0)} - k_B T / a'\right)}{\partial a'}\, a' da'$$

$$\int_{a_{\text{switch}}}^{a_2} \frac{\partial\left(\sum_{i=1}^{n} p_i e^{-q_i(a'-a_0)} - k_B T/a'\right)}{\partial a'}\; a' da'$$

$$\int_{a_{\text{switch}}}^{a_2} \left(-\sum_{i=1}^{n} p_i q_i e^{-q_i(a'-a_0)} + \frac{k_B T}{a'^2}\right) a' da'$$

$$\int_{a_{\text{switch}}}^{a_2} -\sum_{i=1}^{n} p_i q_i e^{-q_i(a'-a_0)}\, a' + \frac{k_B T}{a'}\; da'$$

$$\int_{a_{\text{switch}}}^{a_2} -\sum_{i=1}^{n} p_i q_i e^{-q_i(a'-a_0)}\, a' + \frac{k_B T}{a'}\; da'$$

$$\left[\sum_{i=1}^{n} \frac{p_i q_i e^{-q_i(a'-a_0)}(q_i a' + 1)}{q_i^2} + k_B T \log a'\right]_{a_{\text{switch}}}^{a_2}$$

$$\sum_{i=1}^{n} \frac{p_i}{q_i}\left(e^{-q_i(a-a_0)}(q_i a + 1) - e^{-q_i a_{\text{switch}} - a_0)}(q_i a_{\text{switch}} + 1)\right) + k_B T \log \frac{a}{a_{\text{switch}}}$$

And the 2D vdW piece:

$$\int_{\infty}^{a_{\text{switch}}} \frac{\partial}{\partial a\,'}\left(-\frac{k_B T}{A - a'} - \frac{k_B T}{a'}\right) a' da'$$

$$\int_{\infty}^{a_{\text{switch}}} \frac{\partial}{\partial a\,'}\left(-\frac{k_B T}{A - a'} - \frac{k_B T}{a'}\right) a' da'$$

$$k_B T\left[\frac{A}{a_{\text{switch}} - A} + \log\left(\frac{a_{\text{switch}}}{a_{\text{switch}} - A}\right)\right]$$

Adding these two pieces, we obtain the MEPAW at a given area per molecule a. Note that if $a \leq a_{\text{switch}}$, only the 2D vdW piece needs to be evaluated.

In fitting the parameters, a_{switch} is simply set to the maximum a in the pressure-area data set, a_0 is set to the minimum a in the pressure-area data set, and $\{p_i\}, \{q_i\}$ are fitted using the Kaufmann (2003) scheme, implemented at https://github.com/khuston/Kaufmann2003. This scheme will fit the data with $1 + 2n$ parameters (p_0 and p_i, q_i for $i \in [1, n]$). The script used as large an n as possible, so long as parameters p_i and q_i were positive. For GROMOS 53a6OXY+D Tween 80, the fitting parameters were $p_0 = 0.2323, p_1 = 38.5993, q_1 = 0.4657$.

A.3.3 Intramolecular density contour plots

To make the intramolecular density contour plots, a sample of atomic coordinates from the last 20 ns of monolayer simulation was converted from Cartesian (x,y,z) to cylindrical (r,z) coordinates, where the direction z points along the interface normal from oil into water. The coordinate system is defined relative to a central atom (chosen to be the ester carbon, in this case) and the vector $(0,0,1)$. Atomic positions are binned into a 2D histogram on r,z. Note that bins at larger r collect points froma larger cylindrical shell, whose volume scales as r. For this reason, the density was normalized with respect to this increasing shell volume. The plots are meant to be qualitative, so the atoms were weighted equally in binning. The contour values were at a fixed number density of atoms in the group (either head or tail).

A.3.4 Note on hysteresis

Hysteresis arises from inadequate sampling of the simulated system. Molecular dynamics simulation samples configuration space by following Newton's equations of motion, which provide the correct Boltzmann weighting if ergodicity is given, but MD is inefficient at crossing high-energy barriers. Such an energy barrier exists between "tail-extended” and “tail-retracted” states (see Fig. A-3):

In outward pulling, the tail begins in contact with the oil. As Tween 80 pulls away, the tail lingers in contact, so the “tail-extended” state is initially sampled. If this “tail-extended” state is overrepresented, the calculated PMF will be artificially deep.

In inward pulling, the tail begins in aqueous solution. As Tween 80 approaches, the tail eventually extends to contact the interface, but the “tail-retracted” state is initially over-sampled, and if the inward pulling is not extremely slow, this overrepresentation is not averaged out and the calculated PMF will be artificially shallow.

For the oleate tail to pass between “tail-extended” and “tail-retracted” states, it must break contact with the oil and then retract. This process has a free energy barrier that makes passage between the two states difficult. Given sufficient time to sample, the PMFs calculated from inward and outward pulling will converge to the correct PMF. Otherwise, the calculated PMFs will bracket the correct PMF. In the PMF generated by inward pulling (solid line in Figure A-3), sharp jumps (e.g. point “B” in Figure A-3) near the profile’s right end are due to simulation windows in which the tail contacted and stuck to the oil. Some adjacent windows did not have enough time for the oleate tail to contact the interface; the Tween 80 feels an isotropic environment, and the PMF remains horizontal (e.g. points “C” in Figure A-3).

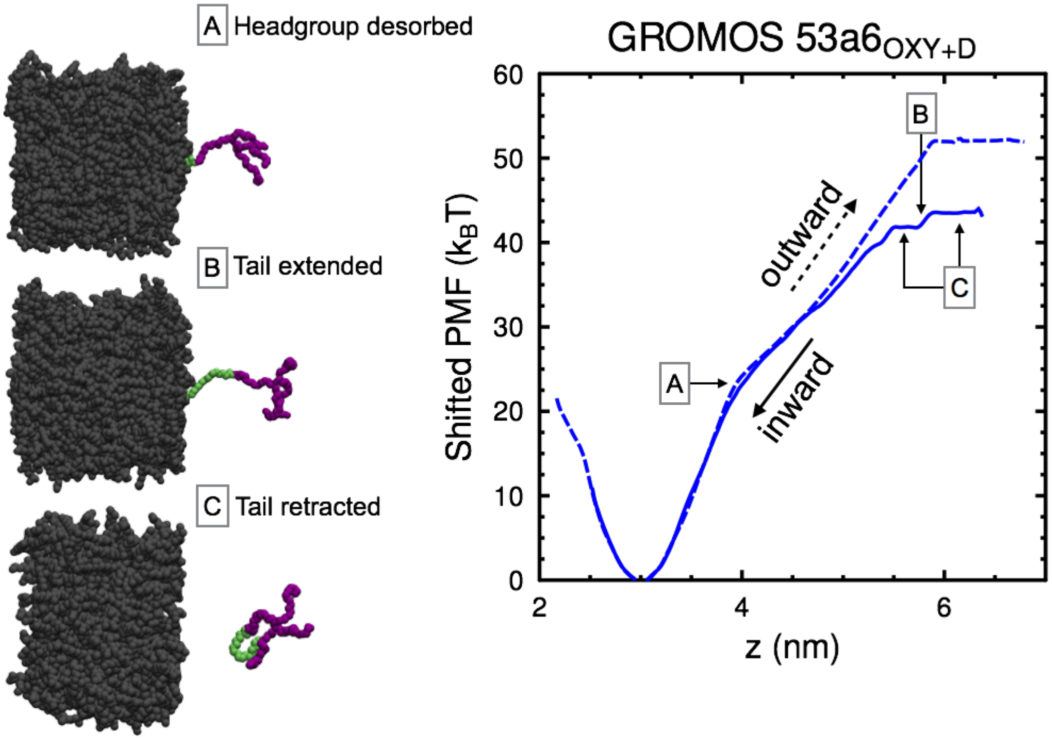

Figure A-3. Above, non-converged PMFs of Tween 80 at the clean water/squalane interface are zeroed at their minima to highlight their overlap near the interface and divergence toward aqueous bulk. "A" separates tail desorption (to its right) from headgroup desorption (to its left). "B" and "C" point to sections of the inward-pulling PMF that are based on tail-extended and tail-retracted windows, respectively. The tail-extended windows cause abrupt jumps in the PMF. These are separated by horizontal stretches where the surfactant with retracted tail senses an isotropic environment.

Advanced sampling techniques may hop the barrier between extended and retracted states more quickly, yielding the correct PMF without brute-force MD simulation. For this study, we contented ourselves with bracketing the correct profiles in some cases where even with the uncertainty in the exact depth of the potential, we could still make strong conclusions about the irreversibility of the adsorption.

A.3.5 2D-biased umbrella sampling to obtain 1D PMF

We introduced a second harmonic bias on the surfactant tail's center of mass Y (Fig. A-4). With the resulting 2D-biased trajectories, we used Grossfield's WHAM5 to output the 2D potential of mean force W_{ZY}:

$$W_{ZY}(z, y) = -k_B T \ln \rho_{ZY}(z, y) + C \qquad \text{(S5)}$$

where ρ_{ZY} is the unbiased joint probability density of finding the molecule at $Z = z$ and $Y = y$, k_B is Boltzmann's constant, T is the simulation temperature (300 K), and C is an arbitrary PMF shift independent of z and y. We could then integrate the joint probability ρ_{ZY} along Y to obtain the 1D PMF.

$$W_Z(z) = \, -k_B T \ln \left[\int e^{-\frac{W_{ZY}(z,y)}{k_B T}} \, dy \right] + B \qquad \text{(S6)}$$

Following the convention in Equation 1, the constant B shifts W_Z vertically to be zero in bulk water.

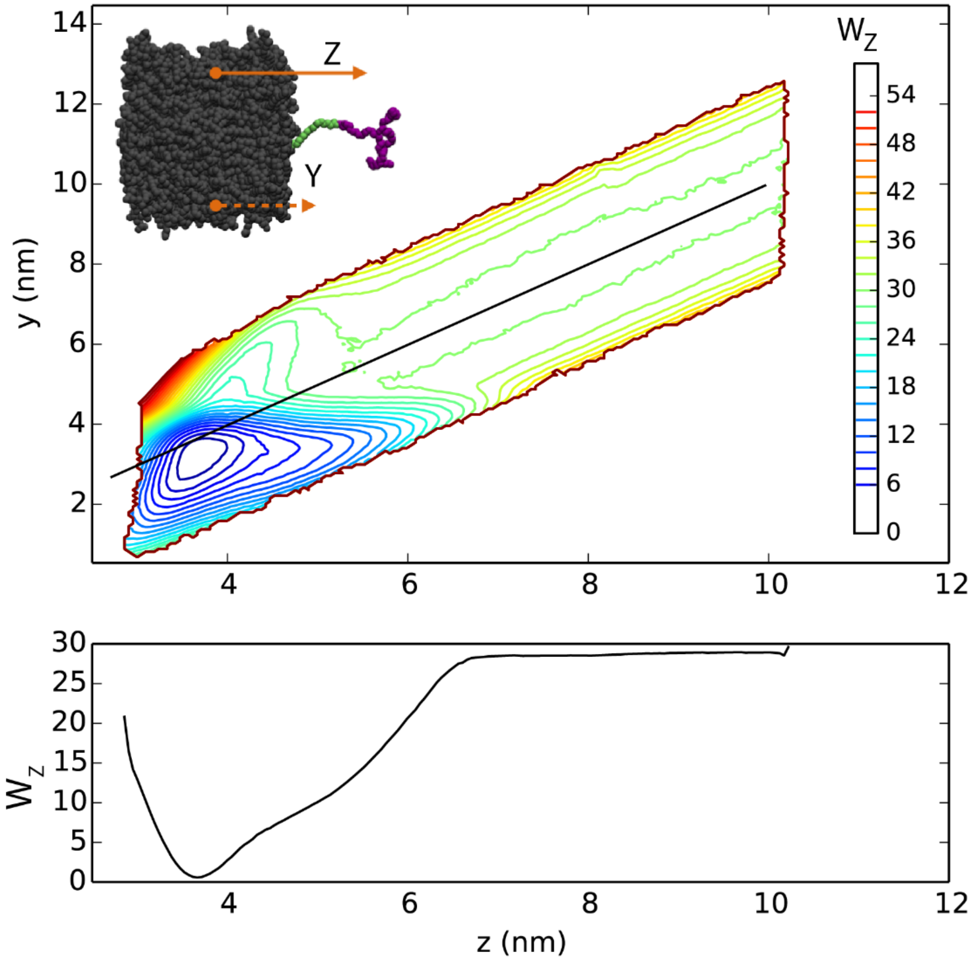

Figure A-4. The upper plot shows colored contours of constant PMF W_{ZY} sampled for Tween 80 using the MARTINI (Lee et al.) forcefield. The line $y = z$ is superimposed on the contour plot in black. Following this line to large z, we see W_{ZY} becomes symmetric in y where the surfactant no longer makes contact with the interface, as expected. The lower plot shows the 1D PMF W_Z that results from integrating over tail positions y (Eqn. S6). The two reduced coordinates Z (surfactant center of mass) and Y (tail center of mass) are illustrated in the inlaid image.

To generate initial configurations for 2D-biased sampling, we restrained the surfactant center of mass at a series of positions along Z, and for each z, we pulled the tail center of mass to a series of positions along Y. This provided a grid of initial configurations in (Z,Y) space to launch simulations for the 2D PMF plotted with contours in the upper part of Figure A-4. Harmonic spring constants for Z and Y were 1000 and 250 kJ mol^{-1} nm^{-2}, respectively.

A.3.6 Partial sampling of 2D PMF

Contributions to the adsorption coefficient drop off exponentially with increases in the PMF (see Equation 8). When the tail is pulled far enough, i.e. when y deviates far enough from the $z = y$ line, the PMF increases monotonically with increasing distance. Thus, coordinate space beyond this point with PMF more than several k_BT greater than the PMF minimum can be neglected. Hysteretic sections of the 1D PMF could be avoided altogether by carving a path through the 2D (z,y) space to bridge two regions which adequately sample y. We used such a scheme in generating the 1D PMFs for the Rossi et al. Tween 80. Figure A-5 highlights in gray the section around 7-11 nm in which y was not fully sampled, and a narrow path was taken from the adsorption basin to the bulk. The section of W_Z highlighted in gray is then not in fact a PMF, but an artifact of the integrating the partially-sampled 2D space.

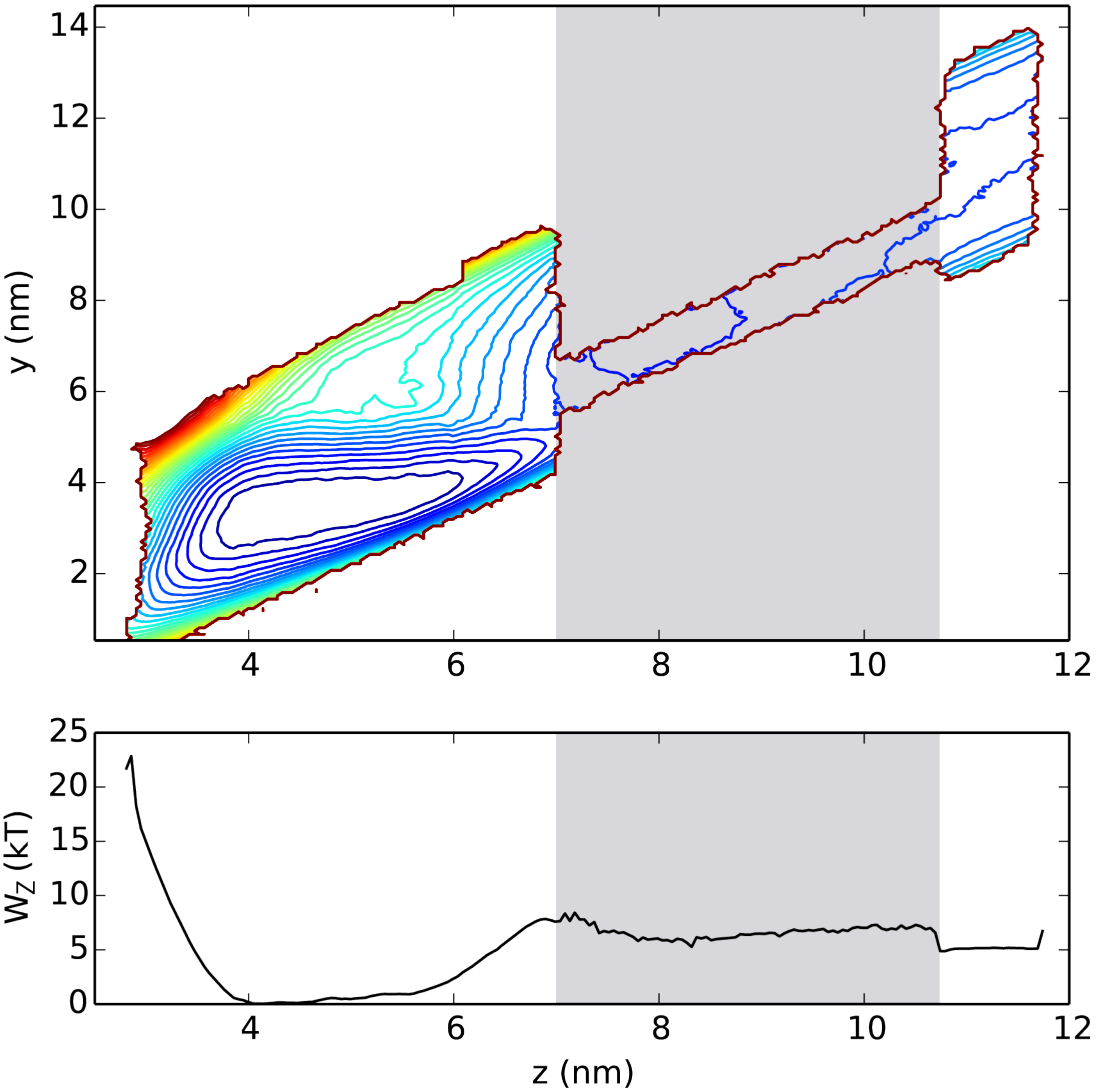

Figure A-5. The plots are grayed where the sampled 2D space is missing significant contributions to the partition function at a given *z*. Thus the integrated 1D PMF is meaningless in that region. However, a path is established in 2D space between the adsorbed region (left) and bulk region (right), and differences in the 1D PMF between these regions are accurate, so long as the PMF difference along the 2D path is accurate.

A.4 Molecular simulation details

A.4.1 SMILES strings

PEG3 (hydroxyl-terminal)
OCCOCCOCCO

PEG5 (hydroxyl-terminal)
OCCOCCOCCOCCOCCO

PEG8 (hydroxyl-terminal)

OCCOCCOCCOCCOCCOCCOCCOCCO

PEO3 (methyl-terminal)
COCCOCCOC

PEO5 (methyl-terminal)
COCCOCCOCCOCCOC

PEO8 (methyl-terminal)
COCCOCCOCCOCCOCCOCCOCCOC

A.4.2 Coarse-grained structure schematics

PEO3, Lee et al. (methyl-terminal)

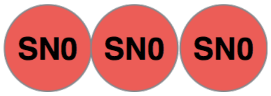

PEO5, Lee et al. (methyl-terminal)

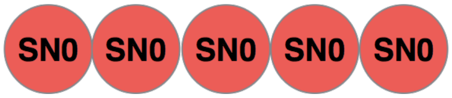

PEO8, Lee et al. (methyl-terminal)

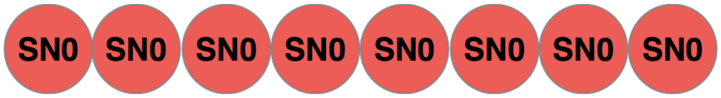

PEG3, Velinova et al. (hydroxyl-terminal)

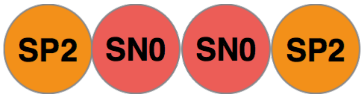

PEG5, Velinova et al. (hydroxyl-terminal)

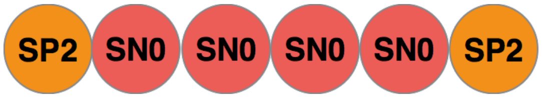

PEG8, Velinova et al. (hydroxyl-terminal)

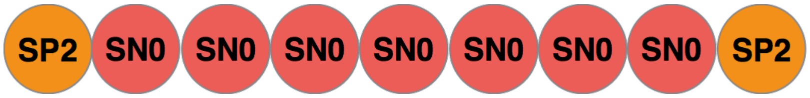

PEG3, Rossi et al. (hydroxyl-terminal)

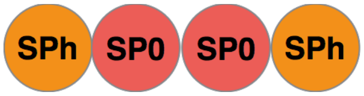

PEG5, Rossi et al. (hydroxyl-terminal)

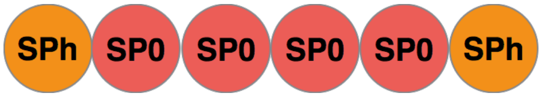

PEG8, Rossi et al. (hydroxyl-terminal)

A.4.3 Gromacs included topology (.itp) files

Some .itp files are printed here for reference.

PEO3 – Martini, Lee et al. (-CH3 terminal)

```
#define     peob     1    0.33      17000.0
#define     peoa     1    130.0     50.0
#define    peod1     1    180.0     1.96      1.0
#define    peod3     1    0.0       0.33      3.0
#define    peod2     1    0.0       0.18      2.0
#define    peod4     1    0.0       0.12      4.0

[ moleculetype ]
; Name            nrexcl
LIG           1

[ atoms ]
;  nr type    resnr resname  atom  cgnr  charge mass
    1  SN0     1     LIG      A1     1     0     54    ;
    2  SN0     1     LIG      A2     2     0     54    ;
    3  SN0     1     LIG      A3     3     0     54    ;

[ bonds ]
;    ai    aj     fu c0, c1, ...
      1     2 peob       ;
      2     3 peob       ;

[ angles ]
;    ai    aj    ak    fu c0, c1, ...
      1     2     3 peoa        ;
```

PEO5 – Martini, Lee et al. (-CH3 terminal)

```
#define     peob     1    0.33      17000.0
#define     peoa     1    130.0     50.0
#define    peod1     1    180.0     1.96      1.0
#define    peod3     1    0.0       0.33      3.0
#define    peod2     1    0.0       0.18      2.0
#define    peod4     1    0.0       0.12      4.0

[ moleculetype ]
; Name            nrexcl
LIG           1

[ atoms ]
;  nr type    resnr resname  atom  cgnr  charge mass
    1  SN0     1     LIG      A1     1     0     54    ;
    2  SN0     1     LIG      A2     2     0     54    ;
    3  SN0     1     LIG      A3     3     0     54    ;
    4  SN0     1     LIG      A4     4     0     54    ;
    5  SN0     1     LIG      A5     5     0     54    ;

[ bonds ]
```

```
;    ai    aj    fu c0, c1, ...
      1     2 peob       ;
      2     3 peob       ;
      3     4 peob       ;
      4     5 peob       ;

[ angles ]
;    ai    aj    ak    fu c0, c1, ...
      1     2     3 peoa       ;
      2     3     4 peoa       ;
      3     4     5 peoa       ;

[ dihedrals ]
;    ai    aj    ak    al    fu c0, c1, ...
      1     2     3     4 peod1      ;
      1     2     3     4 peod3      ;
      1     2     3     4 peod2      ;
      1     2     3     4 peod4      ;
      2     3     4     5 peod1      ;
      2     3     4     5 peod3      ;
      2     3     4     5 peod2      ;
      2     3     4     5 peod4      ;
```

PEO8 – Martini, Lee et al. (-CH3 terminal)

```
#define     peob     1    0.33      17000.0
#define     peoa     1    130.0     50.0
#define    peod1     1    180.0     1.96      1.0
#define    peod3     1    0.0       0.33      3.0
#define    peod2     1    0.0       0.18      2.0
#define    peod4     1    0.0       0.12      4.0

[ moleculetype ]
; Name            nrexcl
LIG           1

[ atoms ]
;  nr type    resnr resname  atom  cgnr  charge mass
    1  SN0     1     LIG      A1     1     0     54    ;
    2  SN0     1     LIG      A2     2     0     54    ;
    3  SN0     1     LIG      A3     3     0     54    ;
    4  SN0     1     LIG      A4     4     0     54    ;
    5  SN0     1     LIG      A5     5     0     54    ;
    6  SN0     1     LIG      A6     6     0     54    ;
    7  SN0     1     LIG      A7     7     0     54    ;
    8  SN0     1     LIG      A8     8     0     54    ;

[ bonds ]
;    ai    aj    fu c0, c1, ...
      1     2 peob       ;
      2     3 peob       ;
      3     4 peob       ;
      4     5 peob       ;
      5     6 peob       ;
      6     7 peob       ;
      7     8 peob       ;

[ angles ]
;    ai    aj    ak    fu c0, c1, ...
      1     2     3 peoa       ;
      2     3     4 peoa       ;
      3     4     5 peoa       ;
      4     5     6 peoa       ;
      5     6     7 peoa       ;
      6     7     8 peoa       ;

[ dihedrals ]
;    ai    aj    ak    al    fu c0, c1, ...
      1     2     3     4 peod1      ;
      1     2     3     4 peod3      ;
      1     2     3     4 peod2      ;
      1     2     3     4 peod4      ;
      2     3     4     5 peod1      ;
      2     3     4     5 peod3      ;
      2     3     4     5 peod2      ;
      2     3     4     5 peod4      ;
      3     4     5     6 peod1      ;
      3     4     5     6 peod3      ;
      3     4     5     6 peod2      ;
      3     4     5     6 peod4      ;
      4     5     6     7 peod1      ;
      4     5     6     7 peod3      ;
      4     5     6     7 peod2      ;
      4     5     6     7 peod4      ;
      5     6     7     8 peod1      ;
      5     6     7     8 peod3      ;
      5     6     7     8 peod2      ;
      5     6     7     8 peod4      ;
```

PEG3 – Martini, Velinova et al. (-OH terminal)

```
#define     peob     1    0.33      17000.0
#define     peoa     1    130.0     50.0
#define    peod1     1    180.0     1.96      1.0
#define    peod3     1    0.0       0.33      3.0
#define    peod2     1    0.0       0.18      2.0
#define    peod4     1    0.0       0.12      4.0

[ moleculetype ]
; Name            nrexcl
LIG           1

[ atoms ]
;  nr type    resnr resname  atom  cgnr  charge mass
    1  SP2     1     LIG      A1     1     0     54    ;
    2  SN0     1     LIG      A2     2     0     54    ;
    3  SN0     1     LIG      A3     3     0     54    ;
    4  SP2     1     LIG      A4     4     0     54    ;

[ bonds ]
;    ai    aj    fu c0, c1, ...
      1     2 peob       ;
      2     3 peob       ;
      3     4 peob       ;

[ angles ]
;    ai    aj    ak    fu c0, c1, ...
      1     2     3 peoa       ;
      2     3     4 peoa       ;

[ dihedrals ]
;    ai    aj    ak    al    fu c0, c1, ...
      1     2     3     4 peod1      ;
      1     2     3     4 peod3      ;
      1     2     3     4 peod2      ;
      1     2     3     4 peod4      ;
```

PEG5 – Martini, Velinova et al. (-OH terminal)

```
#define     peob     1    0.33      17000.0
#define     peoa     1    130.0     50.0
#define    peod1     1    180.0     1.96      1.0
#define    peod3     1    0.0       0.33      3.0
#define    peod2     1    0.0       0.18      2.0
#define    peod4     1    0.0       0.12      4.0

[ moleculetype ]
; Name            nrexcl
LIG           1

[ atoms ]
;  nr type    resnr resname  atom  cgnr  charge mass
    1  SP2     1     LIG      A1     1     0     54    ;
    2  SN0     1     LIG      A2     2     0     54    ;
    3  SN0     1     LIG      A3     3     0     54    ;
    4  SN0     1     LIG      A4     4     0     54    ;
    5  SN0     1     LIG      A5     5     0     54    ;
    6  SP2     1     LIG      A6     6     0     54    ;

[ bonds ]
;    ai    aj    fu c0, c1, ...
      1     2 peob       ;
      2     3 peob       ;
      3     4 peob       ;
      4     5 peob       ;
      5     6 peob       ;

[ angles ]
;    ai    aj    ak    fu c0, c1, ...
      1     2     3 peoa       ;
      2     3     4 peoa       ;
      3     4     5 peoa       ;
      4     5     6 peoa       ;

[ dihedrals ]
;    ai    aj    ak    al    fu c0, c1, ...
      1     2     3     4 peod1      ;
      1     2     3     4 peod3      ;
      1     2     3     4 peod2      ;
      1     2     3     4 peod4      ;
      2     3     4     5 peod1      ;
      2     3     4     5 peod3      ;
      2     3     4     5 peod2      ;
      2     3     4     5 peod4      ;
      3     4     5     6 peod1      ;
      3     4     5     6 peod3      ;
      3     4     5     6 peod2      ;
      3     4     5     6 peod4      ;
```

PEG8 – Martini, Velinova et al. (-OH terminal)

```
#define     peob     1    0.33      17000.0
#define     peoa     1    130.0     50.0
#define    peod1     1    180.0     1.96      1.0
#define    peod3     1    0.0       0.33      3.0
#define    peod2     1    0.0       0.18      2.0
#define    peod4     1    0.0       0.12      4.0

[ moleculetype ]
; Name            nrexcl
LIG           1

[ atoms ]
;  nr type    resnr resname  atom  cgnr  charge mass
    1  SP2     1     LIG      A1     1     0     54    ;
    2  SN0     1     LIG      A2     2     0     54    ;
    3  SN0     1     LIG      A3     3     0     54    ;
    4  SN0     1     LIG      A4     4     0     54    ;
    5  SN0     1     LIG      A5     5     0     54    ;
    6  SN0     1     LIG      A6     6     0     54    ;
    7  SN0     1     LIG      A7     7     0     54    ;
    8  SN0     1     LIG      A8     8     0     54    ;
    9  SP2     1     LIG      A9     9     0     54    ;

[ bonds ]
;    ai    aj    fu c0, c1, ...
      1     2 peob       ;
      2     3 peob       ;
      3     4 peob       ;
      4     5 peob       ;
      5     6 peob       ;
      6     7 peob       ;
      7     8 peob       ;
      8     9 peob       ;

[ angles ]
;    ai    aj    ak    fu c0, c1, ...
      1     2     3 peoa       ;
      2     3     4 peoa       ;
      3     4     5 peoa       ;
      4     5     6 peoa       ;
      5     6     7 peoa       ;
      6     7     8 peoa       ;
      7     8     9 peoa       ;

[ dihedrals ]
;    ai    aj    ak    al    fu c0, c1, ...
      1     2     3     4 peod1      ;
      1     2     3     4 peod3      ;
      1     2     3     4 peod2      ;
      1     2     3     4 peod4      ;
      2     3     4     5 peod1      ;
      2     3     4     5 peod3      ;
      2     3     4     5 peod2      ;
      2     3     4     5 peod4      ;
      3     4     5     6 peod1      ;
      3     4     5     6 peod3      ;
      3     4     5     6 peod2      ;
      3     4     5     6 peod4      ;
      4     5     6     7 peod1      ;
      4     5     6     7 peod3      ;
      4     5     6     7 peod2      ;
      4     5     6     7 peod4      ;
      5     6     7     8 peod1      ;
      5     6     7     8 peod3      ;
      5     6     7     8 peod2      ;
      5     6     7     8 peod4      ;
      6     7     8     9 peod1      ;
      6     7     8     9 peod3      ;
      6     7     8     9 peod2      ;
      6     7     8     9 peod4      ;
```

PEG3 – GROMOS 53a6OXY+D (-OH terminal)

```
[ moleculetype ]
; Name            nrexcl
triethyleneglycol    3

[ atoms ]
;   nr       type  resnr residue  atom   cgnr     charge       mass  typeB    chargeB
massB
; residue   1 EG3 rtp EG3  q  0.0
     1          H      1    EG3     H1      1       0.41      1.008   ; qtot 0.41
     2        OA2      1    EG3     O2      2       -0.7    15.9994   ; qtot -0.29
     3        CH2      1    EG3     C3      3       0.29     14.027   ; qtot 0
     4        CH2      1    EG3     C4      4       0.29     14.027   ; qtot 0.29
     5        OE2      1    EG3     O5      5      -0.58    15.9994   ; qtot -0.29
     6        CH2      1    EG3     C6      6       0.29     14.027   ; qtot 0
     7        CH2      1    EG3     C7      7       0.29     14.027   ; qtot 0.29
     8        OE2      1    EG3     O8      8      -0.58    15.9994   ; qtot -0.29
     9        CH2      1    EG3     C9      9       0.29     14.027   ; qtot 0
    10        CH2      1    EG3    C10     10       0.29     14.027   ; qtot 0.29
    11        OA2      1    EG3    O11     11       -0.7    15.9994   ; qtot -0.41
    12          H      1    EG3    H12     12       0.41      1.008   ; qtot 0

[ bonds ]
;  ai    aj funct            c0            c1            c2            c3
    1     2     2
    2     3     2
    3     4     2
    4     5     2
    5     6     2
    6     7     2
    7     8     2
    8     9     2
    9    10     2
   10    11     2
   11    12     2

[ pairs ]
;  ai    aj funct            c0            c1            c2            c3
    1     4     1
    2     5     1
    3     6     1
    4     7     1
    5     8     1
    6     9     1
    7    10     1
    8    11     1
    9    12     1

[ angles ]
;  ai    aj    ak funct            c0            c1            c2            c3
    1     2     3     2
    2     3     4     2
    3     4     5     2
    4     5     6     2
    5     6     7     2
    6     7     8     2
    7     8     9     2
    8     9    10     2
    9    10    11     2
   10    11    12     2
[ dihedrals ]
;  ai    aj    ak    al funct            c0            c1            c2            c3
c4            c5
    1     2     3     4     1
    2     3     4     5     1
    3     4     5     6     1
    4     5     6     7     1
    5     6     7     8     1
```

```
     6     7     8     9     1
     7     8     9    10     1
     8     9    10    11     1
     9    10    11    12     1
```

A.5 Discussion of force field accuracy

Transfer of an alkane from oil to water can follow an indirect path with two steps: 1) transfer of an alkane from liquid alkane to gas (vaporization) and 2) transfer of an alkane from gas to liquid water (hydration). GROMOS 45a3 underwent optimization of aliphatic interaction parameters to reproduce the heat of vaporization and free enthalpy of hydration.[6] These parameters were retained in GROMOS 53a6, so the free energy to transfer the alkane-like fatty acid tail from liquid alkane to liquid water should be accurate.[7] The MARTINI forcefield should also be accurate; Baron et al.[8] measured alkane/water transfer free energies for MARTINI alkanes, and their values for butane, octane, and dodecane (5.81, 9.12, 12.8 kcal/mole at 303 K) closely match the respective experimental values in Abraham et al.[9] (5.02, 9.52, 12.85 kcal/mole at 298 K).

A.6 References

(1) Radke, C. J. Gibbs Adsorption Equation for Planar Fluid–fluid Interfaces: Invariant Formalism. Adv. Colloid Interface Sci.

(2) Rowlinson, J. S.; Widom, B. Molecular Theory of Capillarity; Courier Corporation, 2013.

(3) Nikas, Y. J.; Puvvada, S.; Blankschtein, D. Surface Tensions of Aqueous Nonionic Surfactant Mixtures. Langmuir 1992, 8 (11), 2680–2689.

(4) Mulqueen, M.; Blankschtein, D. Theoretical and Experimental Investigation of the Equilibrium Oil−Water Interfacial Tensions of Solutions Containing Surfactant Mixtures. Langmuir 2002, 18 (2), 365–376.

(5) Grossfield, A. WHAM: The Weighted Histogram Analysis Method.

(6) Schuler, L. D.; Daura, X.; van Gunsteren, W. F. An Improved GROMOS96 Force Field for Aliphatic Hydrocarbons in the Condensed Phase. J. Comput. Chem. 2001, 22 (11), 1205–1218.

(7) Oostenbrink, C.; Villa, A.; Mark, A. E.; Van Gunsteren, W. F. A Biomolecular Force Field Based on the Free Enthalpy of Hydration and Solvation: The GROMOS Force-Field Parameter Sets 53A5 and 53A6. J. Comput. Chem. 2004, 25 (13), 1656–1676.

(8) Baron, R.; Trzesniak, D.; de Vries, A. H.; Elsener, A.; Marrink, S. J.; van Gunsteren, W. F. Comparison of Thermodynamic Properties of Coarse-Grained and Atomic-Level Simulation Models. ChemPhysChem 2007, 8 (3), 452–461.

(9) Abraham, M. H. Thermodynamics of Solution of Homologous Series of Solutes in Water. J. Chem. Soc. Faraday Trans. 1 Phys. Chem. Condens. Phases 1984, 80 (1), 153–181.

APPENDIX B

Supplementary information for Chapter 3

B.1 Surfactant self-associativity

Associativity constants K_1, K_2, etc. are defined to give a series of equilibria, including for dimers and trimers.

$$c_2 = K_1 c_1 c_1 \tag{S.1.1}$$

$$c_3 = K_2 c_2 c_1 \tag{S.1.2}$$

where c_i is the concentration of i-mers such that $c_T = \sum_i i c_i$. The above equilibria can be written in a recursive form:

$$c_n = K_{n-1} c_{n-1} c_1 \tag{S.1.3}$$

For analysis, we make use of the composition ratios of multimers to monomers.

$$\frac{c_n}{c_1} = K_{n-1} c_{n-1} \tag{S.1.4}$$

Furthermore, we note that c_{n-1} can be iteratively expanded to as a product of associativity constants and c_1.

$$\frac{c_n}{c_1} = \left(\prod_{j=1}^{n-1} K_j \right) c_1^{n-1} \tag{S.1.5}$$

By substituting $n - 1$ for n in the above equation, we obtain:

$$\frac{c_{n-1}}{c_1} = \left(\prod_{j=1}^{n-2} K_j\right) c_1^{n-2} \tag{S.1.6}$$

$$\frac{c_n}{c_1} = K_{n-1} c_1 \left(\prod_{j=1}^{n-2} K_j\right) c_1^{n-2} \tag{S.1.7}$$

$$\frac{c_n}{c_1} = K_{n-1} c_1 \frac{c_{n-1}}{c_1} \tag{S.1.8}$$

The ratio of surfactant n-mer concentration to surfactant monomer concentration decreases with aggregation number unless $K_{n-1}c_1 > 1$.

To calculate the associativity from molecular simulation (given the radial distribution function *g* for surfactant molecules relative to an aggregate of size n),

$$K_n = \frac{c_{n+1}}{c_n c_1} = 4\pi \int_0^R g(r)\, r^2\, dr \tag{S.1.9}$$

B.2 Deriving steady-state probability current into sink from Dirichlet boundary condition

We start from the one-dimensional Smoluchowski equation:[1]

$$\frac{\partial W}{\partial t} = \frac{\partial}{\partial x}\left[D^{(2)} e^{-\tilde{G}} \frac{\partial}{\partial x}\left(e^{\tilde{G}} W\right)\right] \tag{S.2.1}$$

with $W(x,t)$ the species probability distribution (or concentration), $D^{(2)}(x)$ the diffusivity, $\tilde{G}(x)$ the free energy in kT units, x the position, and t the time. First we perform differentiations using the product rule and take advantage of some cancellations of terms.

$$\frac{\partial W}{\partial t} = \frac{\partial}{\partial x}\left[D^{(2)} \frac{\partial \tilde{G}}{\partial x} e^{-\tilde{G}} e^{\tilde{G}} W + D^{(2)} e^{-\tilde{G}} e^{\tilde{G}} \frac{\partial W}{\partial x}\right] \tag{S.2.2}$$

$$\frac{\partial W}{\partial t} = \frac{\partial}{\partial x}\left[D^{(2)} \frac{\partial \tilde{G}}{\partial x} W + D^{(2)} \frac{\partial W}{\partial x}\right] \tag{S.2.3}$$

Let $\varDelta^{(1)} = -D^{(2)}\frac{\partial\tilde{G}}{\partial x}$ (S.2.4)

$$\frac{\partial W}{\partial t} = \frac{\partial}{\partial x}\left[-\varDelta^{(1)}W + D^{(2)}\frac{\partial W}{\partial x}\right] \tag{S.2.5}$$

$$\frac{\partial W}{\partial t} = -\frac{\partial}{\partial x}\left[\varDelta^{(1)}W\right] + \frac{\partial}{\partial x}\left[D^{(2)}\frac{\partial W}{\partial x}\right] \tag{S.2.6}$$

Let $D^{(1)} = \varDelta^{(1)} + \frac{\partial D^{(2)}}{\partial x}$ (S.2.7)

$$\frac{\partial \mathrm{W}}{\partial \mathrm{t}} = -\frac{\partial}{\partial \mathrm{x}}\left[\mathrm{D}^{(1)}\mathrm{W} - \frac{\partial \mathrm{D}^{(2)}}{\partial \mathrm{x}}\mathrm{W}\right] + \frac{\partial}{\partial \mathrm{x}}\left[\mathrm{D}^{(2)}\frac{\partial \mathrm{W}}{\partial \mathrm{x}}\right] \tag{S.2.8}$$

Re-arrange the terms to get

$$\frac{\partial W}{\partial t} = -\frac{\partial}{\partial x}\left[D^{(1)}W\right] + \frac{\partial}{\partial x}\left[D^{(2)}\frac{\partial W}{\partial x} + \frac{\partial D^{(2)}}{\partial x}W\right] \tag{S.2.9}$$

Reverse the product rule in the right term, giving

$$\frac{\partial W}{\partial t} = -\frac{\partial}{\partial x}\left[D^{(1)}W\right] + \frac{\partial^2}{\partial x^2}\left[D^{(2)}W\right] \tag{S.2.10}$$

This is the one-dimensional Fokker-Planck equation specified by Equations 5.1 and 5.2 from Risken.[2]

We now eliminate $\varDelta^{(1)}$ from S.2.4 and S.2.7 to obtain

$$-D^{(2)}\frac{\partial\tilde{G}}{\partial x} = D^{(1)} - \frac{\partial D^{(2)}}{\partial x} \tag{S.2.11}$$

$$\frac{\partial\tilde{G}}{\partial x} = -\frac{D^{(1)}}{D^{(2)}} + \frac{1}{D^{(2)}}\frac{\partial D^{(2)}}{\partial x} \tag{S.2.12}$$

$$\tilde{G}(x) = \ln D^{(2)}(x) - \int^{x}\frac{D^{(1)}(x')}{D^{(2)}(x')}dx' \tag{S.2.13}$$

The stationary solution of S.2.10, given a uniform probability current S, is equation 5.16 from Risken:[2]

$$W_{st}(x) = Ne^{-\Phi(x)} - Se^{-\Phi(x)} \int^{x} \frac{e^{\Phi(x')}}{D^{(2)}(x')} dx' \tag{S.2.14}$$

where N is a constant, $W_{st}(x)$ is the steady-state probability distribution, and $\Phi(x) = \ln D^{(2)}(x) - \int^{x} \frac{D^{(1)}(x')}{D^{(2)}(x')} dx'$. By comparing this expression with Eq. S.2.13, we can see that $\Phi(x)$ is $\tilde{G}(x)$, the free energy in kT units.

The solution, Eq. S.2.14, is subject to the normalization condition

$$\int_{0}^{X} W_{st}(x)\, dx = 1 \tag{S.2.15}$$

And we also impose a sink boundary condition

$$x = 0 \rightarrow W_{st} = 0$$

We expand the indefinite integral in Eq. S.2.14 into a definite integral plus an additive constant.

$$W_{st}(x) = Ne^{-\Phi(x)} - Se^{-\Phi(x)} \left(\int_{0}^{x} \frac{e^{\Phi(x')}}{D^{(2)}(x')} dx' + C \right) \tag{S.2.16}$$

We can apply the sink boundary condition here, giving

$$W_{st}(0) = 0 = Ne^{-\Phi(0)} - SCe^{-\Phi(0)} \tag{S.2.17}$$

$$C = \frac{N}{S} \tag{S.2.18}$$

Re-substituting the constant C, we find that N is eliminated from the equation:

$$W_{st}(x) = Ne^{-\Phi(x)} - Se^{-\Phi(x)} \left(\int_{0}^{x} \frac{e^{\Phi(x')}}{D^{(2)}(x')} dx' + \frac{N}{S} \right) \tag{S.2.19}$$

$$W_{st}(x) = -S \int_{0}^{x} \frac{e^{\Phi(x') - \Phi(x)}}{D^{(2)}(x')} dx' \tag{S.2.20}$$

We could solve for the probability current S by invoking the normalization condition to eliminate $W_{st}(x)$, but instead we can immediately obtain the particle velocity v by rearrangement:

$$v(x) = \frac{S}{W_{st}(x)} = -\left(\int_0^x \frac{e^{\Phi(x')-\Phi(x)}}{D^{(2)}(x')} dx'\right)^{-1} \tag{S.2.21}$$

Evaluating this at $x = X$ gives us the velocity at the sub-surface boundary, or the adsorption rate constant, which we can multiply by the boundary concentration to obtain the steady-state flux of adsorbing molecules. Assuming $X > 0$, we also flip the sign of the velocity to get a positive adsorption coefficient.

$$k_{\text{ads}} = \left(\int_0^X \frac{e^{\Phi(x')-\Phi(X)}}{D^{(2)}(x')} dx'\right)^{-1} \tag{S.2.22}$$

B.3 k_{ads} from steady-state probability current and k_{des} from mean first passage time calculation combine to give correct adsorption equilibrium

To verify our derivation of k_{ads}, we confirmed that it gave the correct equilibrium adsorption when combined with k_{des} calculated as the reciprocal mean first passage time for surfactant to escape from the interfacial energy well.

We calculated k_{ads} according to Equations 2 and 3, and we calculated k_{des} using the mean first passage time integral,[3]

$$k_{\text{des}} = \int_{x=a}^{x=X} \left(\int_{x\prime=a}^{x\prime=x} e^{-\Phi(x\prime)} dx'\right) \frac{e^{\Phi(x)}}{D^{(2)}(x)} \, dx \tag{S.3.1}$$

The net rate of adsorption is given by

$$r = k_{\text{ads}} c_s - k_{\text{des}} \Gamma \tag{S.3.2}$$

At equilibrium, the net adsorption rate is zero, giving the equality

$$\left(\frac{\Gamma}{c_s}\right)_{\text{eq}} = \frac{k_{\text{ads}}}{k_{\text{des}}} \tag{S.3.2}$$

Assuming the surfactant is insoluble at x <0, the equilibrium adsorption Γ/c_s is

$$\left(\frac{\Gamma}{c_s}\right)_{\mathrm{eq}} = \int_0^X \exp\big(-\Phi(x)\big)\, dx \tag{S.3.4}$$

where $\Phi(x)$ is the free energy landscape in kT units shifted to equal zero in the bulk fluid, X is a position on the plateau adjacent to the energy barrier and $x = 0$ is the position of the reflective boundary in Figure 3-4, essentially a hard wall restricting the surfactant to $x \geq 0$. The numerical error between Γ/c_s and $k_{\mathrm{ads}}/k_{\mathrm{des}}$ was less than 1% for all barrier heights tested from 0 to 1000 $k_B T$ using the *NIntegrate* function in Mathematica. Above 90 $k_B T$, our implementation of the k_{ads} calculation using trapezoidal integration began to have large discrepancies. It is worth noting this numerical challenge can arise when making the k_{ads} calculation with very large barriers.

B.4 Derivation of adsorptivity equation

We do not make use of the Gibbs adsorption equation, so it is not necessary to start from the Gibbs-invariant surface excess, which is the relevant thermodynamic surface excess for the Gibbs adsorption equation. However, it can be reassuring to know how the Gibbs-invariant surface excess is related to the surface density used in this paper. This derivation has essentially the same assumptions as we stated in the text and SI of our previous publication, but we carry the simplifications farther.[4] We start from the Gibbs-invariant surface excess of a component $i \neq 1$ at a planar interface as given in Equation 28 of Radke's review.[5]

$$\Gamma_{iE} = \Gamma_{ij} - \Gamma_{1j}\left(\frac{\rho_i^{\alpha} - \rho_i^{\beta}}{\rho_1^{\alpha} - \rho_1^{\beta}}\right) \tag{S.4.1}$$

where Γ_{iE} is the surface excess of component i which is invariant to the choice of Gibbs dividing surface j. Γ_{ij} is the surface excess of component i based on Gibbs dividing surface j, and

ρ_i^α is the volumetric concentration of component i in a bulk phase α. We begin by dividing the all three terms by ρ_i^α and dividing the numerator and denominator of the rightmost factor by ρ_1^α.

$$\frac{\Gamma_{iE}}{\rho_i^\alpha} = \frac{\Gamma_{ij}}{\rho_i^\alpha} - \frac{\Gamma_{1j}}{\rho_1^\alpha}\left(\frac{1-\frac{\rho_i^\beta}{\rho_i^\alpha}}{1-\frac{\rho_1^\beta}{\rho_1^\alpha}}\right) \tag{S.4.2}$$

If we choose β to be the phase in which i is less soluble, then the numerator $1-\frac{\rho_i^\beta}{\rho_i^\alpha}$ is between 0 and 1. If we choose component 1 so that phase α is rich in component 1, and phase β is poor in component 1, then the denominator $1-\frac{\rho_1^\beta}{\rho_1^\alpha}$ is nearly 1. For a surfactant i which adsorbs many orders of magnitude more strongly than component 1, any reasonable choice of dividing surface j would lead to $\frac{\Gamma_{ij}}{\rho_i^\alpha} \gg \frac{\Gamma_{1j}}{\rho_1^\alpha}$. Under these conditions, we can safely assume that $\Gamma_{iE} = \Gamma_{ij}$. Let us set $i = s$ to indicate that component i is the surfactant. Then we can calculate Γ_{ij} using its definition from Rowlinson and Widom.[6] Let x be the position along an axis normal to the planar interface, and let $x = x_j$ be the position of the Gibbs dividing surface j.

$$\Gamma_{sj} = \int_{-\infty}^{x_j}\left[\rho_s(x) - \rho_s^\beta\right]dz + \int_{x_j}^{\infty}\left[\rho_s(x) - \rho_s^\alpha\right]dx \tag{S.4.3}$$

Note that we have made α the phase for $x > x_j$ and β the phase for $x < x_j$. The symbol ∞ in this case does not represent a bound at infinity, but a bound that extends "as far as there is any want of perfect homogeneity in the fluid masses".[7] In the case of a nonionic surfactant, this would be a few molecular widths. We divide by ρ_s^α to obtain an adsorption coefficient

$$\frac{\Gamma_{sj}}{\rho_s^\alpha} = \int_{-\infty}^{x_j}\left[\frac{\rho_s(x)}{\rho_s^\alpha} - \frac{\rho_s^\beta}{\rho_s^\alpha}\right]dz + \int_{x_j}^{\infty}\left[\frac{\rho_s(x)}{\rho_s^\alpha} - 1\right]dx \tag{S.4.4}$$

The dominant contribution to the integral comes from positions at which $\frac{\rho_s(x)}{\rho_s^\alpha}$ is greatest. For a nonionic surfactant which forms a dense monolayer adjacent to a dilute solution, and which has interfacial concentration many orders of magnitude greater than either bulk concentration, $\frac{\rho_s(x)}{\rho_s^\alpha} \gg 1 > \frac{\rho_s^\beta}{\rho_s^\alpha}$, and we can simplify the above. We also replace the $-\infty$ and ∞ with bounds x_β and x_α which, again, are just far enough from the interface on either side to be in homogeneous solution. In fact, as long as x_β and x_α are positioned to include the peak of $\frac{\rho_s(x)}{\rho_s^\alpha}$, their precise position has a negligible effect on the integral:

$$\frac{\Gamma_{sj}}{\rho_s^\alpha} = \int_{x_\beta}^{x_\alpha} \frac{\rho_s(x)}{\rho_s^\alpha} dz \tag{S.4.5}$$

We define $\Phi(x)$ to be the potential of mean force of surfactant which is zeroed in the bulk phase α, and so that

$$\frac{\Gamma_{sj}}{\rho_s^\alpha} = \int_{x_\beta}^{x_\alpha} \exp\big(-\Phi(x)\big)\ dx \tag{S.4.6}$$

And finally, to arrive at Equation S.3.4 we set $x_\beta = 0, x_\alpha = X$, we swap the symbols Γ_{sj} and ρ_s^α for the more concise and familiar Γ and c_s, and we decorate the left-hand side with a reminder that the equation holds at thermodynamic equilibrium.

B.5 Probability of first passage to one of two boundaries from integration of the Smoluchowski equation using the simulation-derived potential of mean force

We modeled the spontaneous adsorption process described in the Methods section by integrating the Smoluchowski equation (S.2.1). The test surfactant molecule started from a harmonic restraint potential centered at 8.3 nm. Rather than use a delta function initial condition, it is slightly more accurate to use the position distribution given by the biased potential as the initial condition. Since the test surfactant molecule was starting at a location where the mean force was zero, this distribution is proportional to $\exp\left(-\frac{1}{k_B T}\frac{k_{\mathrm{umb}}}{2}(z-z_0)^2\right)$ where z_0 is 8.3 nm and k_{umb} is the umbrella spring constant (1500 kJ/mole nm^2). The mass of the distribution is unimportant to the subsequent calculation, so the front factor can be left as unity. At each time step, the flux into each absorbing boundary 1 or 2 is calculated and added to a variable *j_total1* or *j_total2*. The fluxes at each time step are also multiplied by the current time and added to variables *jt_total1* and *jt_total2*. If the integration used a variable time step, one would also have to include a factor of *dt* in the weight, but we used a constant time step and so left it out. The mean first passage time afterward is calculated as (*jt_total1* + *jt_total2*)/(*j_total1* + *j_total2*). The probability of the particle being absorbed by boundary 1 is *j_total1*/(*j_total1* + *j_total2*). The Smoluchowski equation should be integrated for sufficient time that the mean first passage time ceases changing to a few significant figures.

After these predictions were made, we ran molecular simulations of the process represented by the above partial differential equation and conditions. The setup of these simulations is described in the Methods section of the paper, but we include below in Figure B-1 a series of snapshots illustrating a spontaneous adsorption run. In this particular case, the surfactant adsorbed to the interface instead of colliding with the absorbing boundary (not pictured) positioned 1 nm from its starting position.

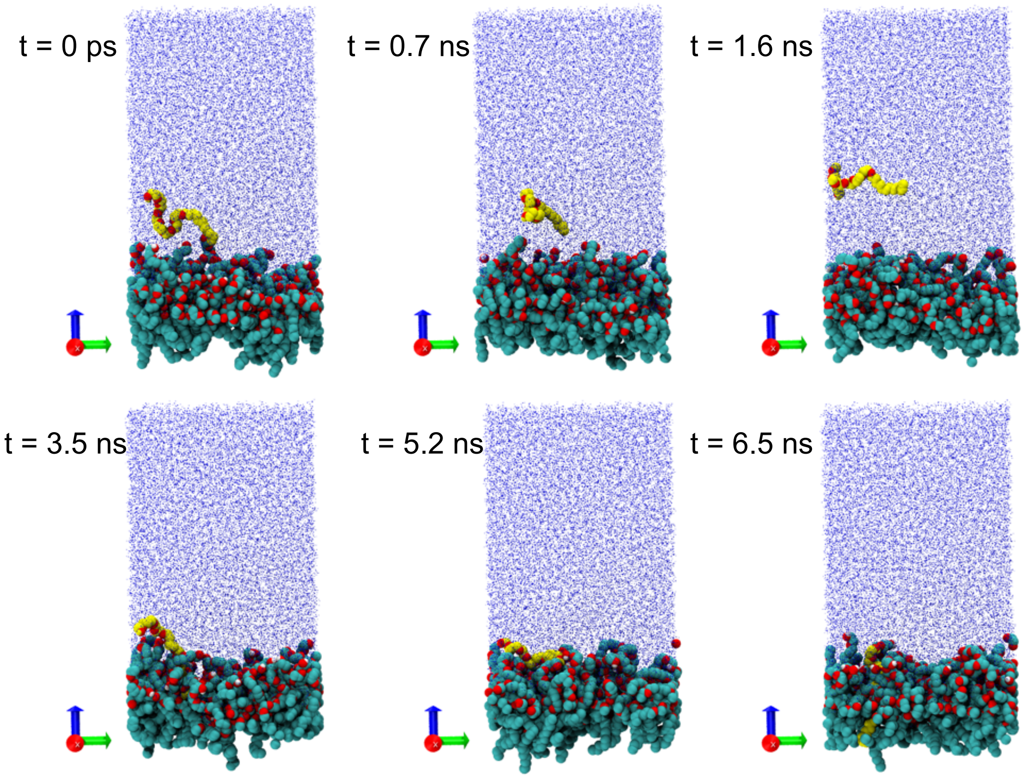

Figure B-1. Snapshots from one of the spontaneous adsorption runs. The water atoms are shrunk by a factor of 10x and colored blue for visibility. The dodecane is removed from view. The test $C_{12}E_8$ molecule is colored yellow (carbon, polar hydrogen) and red (oxygen), and the other $C_{12}E_8$ molecules are colored cyan (carbon), white (polar hydrogen), and red (oxygen). From t=3.5 ns to t=5.2 ns, the hydrophobic tail of the test molecule adsorbs weakly to the headgroups of the monolayer. By t=6.5 ns, the hydrophobic tail is fully inserted.

B.6 Analysis of transient concentration non-uniformity near the interface

B.6.1 Diamant and Andelman

We start with a slightly generalized form of Equation 2.1 from Diamant and Andelman (1996),[8] which gives the deviation from neat interfacial tension due to surfactants, $\Delta\gamma$. We will show that Diamant and Andelman implicitly assumed that the surface-excess free energy density was independent of area, and that this assumption is invalid for nonequilibrium analysis.

$$\Delta\gamma = \left.\frac{\partial F}{\partial A}\right|_{T,p} = \frac{\partial}{\partial A}\int_0^\infty A\,\Delta f[\phi(x,A)]dx + f_0(\phi_0) \tag{S.6.1}$$

where F is free energy, A is interfacial area, Δf is the surface-excess free energy density from that of the bulk fluid, ϕ is the volume fraction of surfactant, ϕ_0 is the volume fraction of surfactant in an interfacial monolayer, and f_0 is the contribution to $\Delta\gamma$ from that monolayer.

Diamant and Andelman give the free energy density Δf as

$$\Delta f[\phi(x)] = \frac{1}{a^3}\{kT[\phi\ln\phi - \phi - (\phi_b\ln\phi_b - \phi_b)] - \mu_b(\phi - \phi_b)\} \tag{S.6.2}$$

where a is the “molecular dimension” (i.e. reciprocal cube root of molecule number density)

Given a large bulk reservoir providing a fixed surfactant chemical potential μ_b, at equilibrium Δf is independent of A because $\phi(x)$ is independent of A. The following simplification results.

$$\Delta\gamma = \left.\frac{\partial F}{\partial A}\right|_{T,p}^{\text{eqbm}} = \int_0^\infty \Delta f[\phi(x)]dx + f_0(\phi_0) \tag{S.6.3}$$

This simplified equation is the starting point for Diamant and Andelman (see Eqn. 2.1 from their paper) despite the assumption that Δf is independent of A. In fact, Δf *does* depend on A, because for a dynamic, non-equilibrium case, ϕ and ϕ_b depend on A kinematically. As A increases, the interface dilates in the tangential direction and the field ϕ is compressed in the normal direction. As A decreases, the interface contracts in the tangential direction, and ϕ is stretched in the normal direction. We emphasize that ϕ is the concentration field for an incompressible solution; the solution itself is not expanding and contracting – it is undergoing an incompressible deformation that transforms its concentration field.

Instead of the simplified Diamant and Andelman version (S.4.3), we revert to the more general form of $\Delta\gamma$ (S.6.1) and substitute the expression for $\Delta f[\phi(x)]$ (S.6.2)

$$\Delta\gamma = \frac{\partial}{\partial A}\int_0^\infty A\ \Big(\frac{1}{a^3}\{kT[\phi\ln\phi - \phi - (\phi_b\ln\phi_b - \phi_b)] - \mu_b(\phi - \phi_b)\}\Big)\,dx + f_0(\phi_0) \tag{S.6.4}$$

Rather than evaluate $\partial/\partial A$ directly, we show that the integral is independent of A when ϕ has the proper dependence on A, i.e. it obeys the kinematics of an affine transformation. The integral of interest is:

$$\int_0^\infty A\ \Big(\frac{1}{a^3}\{kT[\phi\ln\phi - \phi - (\phi_b\ln\phi_b - \phi_b)] - \mu_b(\phi - \phi_b)\}\Big)\,dx \tag{S.6.5}$$

Given an affine transformation that maps position x to position x', the concentration field after transformation ϕ' relates to the original as

$$\phi'(\boldsymbol{x}') = \phi(\boldsymbol{x}) \tag{S.6.6}$$

Consider a planar interface where a parcel of fluid with distance to the interface x is transformed by interfacial dilation to x' such that

$$x' = \left(\frac{dx'}{dx}\right)x \tag{S.6.7}$$

Because the fluid is incompressible, volume must be conserved:

$$xA = x'A' \tag{S.6.8}$$

Given the three preceding equations and a change of integration variable between x and x', the following two integrals are readily shown to be equal.

Integral for interface with area A:

$$\int_0^\infty A\ \Big(\frac{1}{a^3}\{kT[\phi\ln\phi - \phi - (\phi_b\ln\phi_b - \phi_b)] - \mu_b(\phi - \phi_b)\}\Big)\,dx \tag{S.6.9}$$

Integral for interface with area A':

$$\int_0^\infty A' \left(\frac{1}{a^3}\{kT[\phi' \ln \phi' - \phi' - (\phi_b \ln \phi_b - \phi_b)] - \mu_b(\phi' - \phi_b)\}\right) dx' \tag{S.6.10}$$

In this example, we see the value of the integral is independent of the area if the area change is achieved by dilation of a planar interface. Instantaneous, non-equilibrium interfacial area changes are constrained in this way so that ϕ has an area-dependence that results in a constant total surface-excess free energy (except in the monolayer represented by f_0 in equations above). Intuitively, what is happening is that nonequilibrium surface-excess fields are dilating and contracting with the interface, but the total integrated quantity is unchanged, at least for small non-ionic surfactants. Ionic surfactants with long-range interactions may have more complex dynamic surface tension.

As an aside, non-ionic surfactants at equilibrium will generally have $\phi(x) = \phi_b$, so all that remains is the contribution from the interfacial monolayer via f_0.

$$\Delta\gamma = \left.\frac{\partial F}{\partial A}\right|_{T,p} = f_0(\phi_0) \tag{S.6.11}$$

Ionic surfactants can have additional contributions due to the nonuniform free energy field Δf arising from the electric double-layer at equilibrium.

B.6.2 Rusanov and Prokhorov

Equation 14.7 in the first chapter of Rusanov and Prokhorov's Interfacial Tensiometry is[9]

$$\sigma = \gamma + \sum_{i,k} \left(\mu_i^k - \mu_i^{\alpha,\beta}\right) N_i^k / A \tag{S.6.12}$$

where σ is the equilibrium interfacial tension, γ is the instantaneous interfacial tension, N_i^k is the number of moles of component i in layer k with cross-sectional area A, and $\left(\mu_i^k - \mu_i^{\alpha,\beta}\right)$ is the difference between the local chemical potential of species *i* in layer *k* and the chemical potential of species i in either phase α or β depending on which side of a Gibbs dividing surface the layer falls. The authors state "that the difference between σ and γ is caused by the nonuniformity of chemical potentials," for example, "related to the absence of diffusion equilibrium."

It would be surprising if the mere presence of transient concentration gradients near an interface contributed to the dynamic interfacial tension. The above equation S.4.12 comes from Equations 14.5 and 14.6 in Rusanov and Prokhorov:

$$\bar{u} = T\bar{s} + \gamma + \sum_i \left(\mu_i^\alpha \Gamma_i^\alpha + \mu_i^\beta \Gamma_i^\beta\right) + \sum_{i,k} \left(\mu_i^k - \mu_i^{\alpha,\beta}\right) N_i^k / A \tag{S.6.13}$$

$$\sigma = \bar{u} - T\bar{s} - \sum_i \left(\mu_i^\alpha \Gamma_i^\alpha + \mu_i^\beta \Gamma_i^\beta\right) \tag{S.6.14}$$

where T is temperature, $\bar{u}$ is surface energy per unit area and $\bar{s}$ is surface entropy per unit area.

The major flaw is that the authors neglect the contribution of nonuniformity to surface entropy $\bar{s}$. The quantity $\bar{s}$ should include, for example, entropy-of-mixing contributions from the transient concentration gradients. These would exactly negate mixing in the local chemical potential, which we show with an example using ideal components. First we write surface entropy that includes both the equilibrium value $\bar{s}_{\text{eq}}$and the deviation from equilibrium.

$$\bar{s} = -R \sum_{i,k} \left(\ln x_i^k - \ln x_i^{\alpha,\beta}\right) N_i^k / A + \bar{s}_{\text{eq}} \tag{S.6.15}$$

We also write the component chemical potentials for ideal species.

$$\mu_i^k = \mu_i^{\alpha,\beta} + RT\left(\ln x_i^k - \ln x_i^{\alpha,\beta}\right) \tag{S.6.16}$$

With these equations and the corrected σ which only includes the equilibrium surface entropy,

$$\sigma = \bar{u} - T\bar{s}_{\mathrm{eq}} - \sum_i \left(\mu_i^\alpha \Gamma_i^\alpha + \mu_i^\beta \Gamma_i^\beta\right) \tag{S.6.17}$$

We can substitute into S.4.13 and obtain terms that cancel each other.

$$\begin{aligned}\sigma = -RT\left[\sum_{i,k}\left(\ln x_i^k - \ln x_i^{\alpha,\beta}\right)N_i^k/A\right] + \gamma \\ + RT\left[\sum_{i,k}\left(\ln x_i^k - \ln x_i^{\alpha,\beta}\right)N_i^k/A\right]\end{aligned} \tag{S.6.18}$$

$$\sigma = \gamma \tag{S.6.19}$$

The mixing contributions to surface entropy and surface chemical potential negate each other, so there is no effect on dynamic surface tension due merely to concentration gradients and diffusion near a surface.

B.7 References

(1) Yuan, F.; Larson, R. G. Multiscale Molecular Dynamics Simulations of Model Hydrophobically Modified Ethylene Oxide Urethane Micelles. *J. Phys. Chem. B* **2015**, *119* (38), 12540–12551.

(2) Risken, H. *The Fokker-Planck Equation: Methods of Solution and Applications*; Springer Series in Synergetics; Springer Berlin Heidelberg, 1996; Vol. 18.

(3) Yuan, F.; Wang, S.; Larson, R. G. Potentials of Mean Force and Escape Times of Surfactants from Micelles and Hydrophobic Surfaces Using Molecular Dynamics Simulations. *Langmuir* **2015**, *31* (4), 1336–1343.

(4) Huston, K. J.; Larson, R. G. Reversible and Irreversible Adsorption Energetics of Poly(Ethylene Glycol) and Sorbitan Poly(Ethoxylate) at a Water/Alkane Interface. *Langmuir* **2015**.

(5) Radke, C. J. Gibbs Adsorption Equation for Planar Fluid–fluid Interfaces: Invariant Formalism. *Adv. Colloid Interface Sci.* **2015**, *222*, 600–614.

(6) Rowlinson, J. S.; Widom, B. *Molecular Theory of Capillarity*; Courier Corporation, 2013.

(7) Gibbs, J. W. On the Equilibrium of Heterogeneous Substances. *Trans. Conn. Acad. Arts Sci.* **1877**, 380–520.

(8) Diamant, H.; Andelman, D. Kinetics of Surfactant Adsorption at Fluid−Fluid Interfaces. *J. Phys. Chem.* **1996**, *100* (32), 13732–13742.

(9) Chapter 1 Theory of Surface Tension. In *Studies in Interface Science*; Prokhorov, A. I. R. and V. A., Ed.; Interfacial Tensiometry; Elsevier, 1996; Vol. 3, pp 1–47.

APPENDIX C

Supplementary information for Chapter 4

C.1 Verification of non-inertial dynamics with insensitivity to m and k_b

We verified that dynamics were non-inertial and insensitive to the bead mass m (given a constant friction coefficient ζ) and also insensitive to the bond spring constant k_b by testing a monomer, dimer, and trimer under varying m and k_b. In Figures C-1 and C-2, we make two tests of non-inertial dynamics for t_{damp} = 0.064 ps, 0.25 ps, and 4 ps. We plot the brute-force (i.e. direct Langevin simulation, averaged over many runs) desorption times (black circles) versus $\varepsilon_{\mathrm{PW}}$ for monomers, dimers, and trimers at each t_{damp}. In Figure C-1, in each sub-figure we use two bond spring constants, differing by a factor of 2, which does not have a systematic discrepancy on any of the three damping times tested. (The smaller markers are the results for the simulations with $k_b/2$.) For the monomers in each figure (squares), we compared the brute force desorption times with the predictions based on a simple 1D mean first passage time calculation (red X's). The brute force simulation times and the mean first passage time calculations are in good agreement for the monomers with t_{damp} = 0.064 ps and 0.25 ps but not with t_{damp} = 4 ps (the third sub-figure). This indicates the simulations with t_{damp} = 4 ps have inertial dynamics and are not in the overdamped limit. In Figure C-2, we reduce the bead mass by a factor of 3, which does not have a systematic effect for t_{damp} = 0.064 ps and 0.25 ps, but it does have a systematic effect for t_{damp} = 4 ps, further confirming its inertial dynamics. Finally, we checked that the desorption times generated with forward flux sampling had overdamped friction scaling with τdamp. The expected scaling is plotted as a dashed red line in Figure 4-4 for an N = 50 chain. It is evident that $t_{\text{damp}} = 0.25$ ps lies in the strong friction regime. For all subsequent simulations, we used $t_{\text{damp}} = 0.25$ ps.

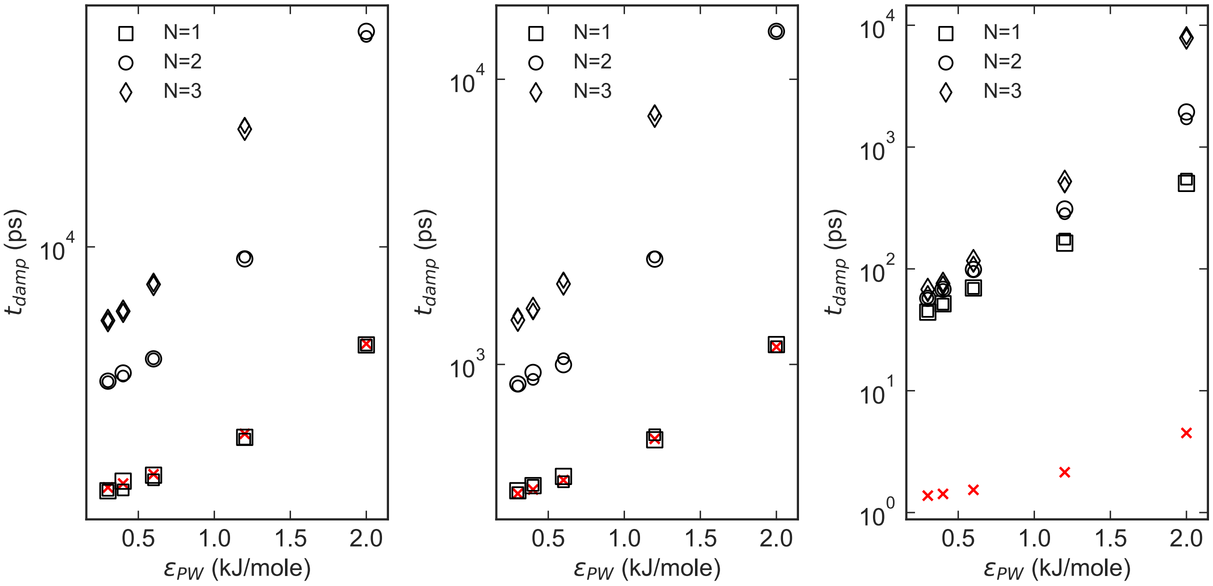

Figure C-1. Desorption times measured by direct Langevin simulation for monomers (squares), dimers (circles) and trimers (diamonds). From left to right, tdamp = 0.064 ps, 0.25 ps, and 4 ps. Mean first passage times for monomers calculated with the Smoluchowski equation are plotted with red X's. Larger symbols indicate simulations with bond spring constant 16000 kJ/mol nm2, and smaller symbols indicate simulations with 8000 kJ/mol nm2. In none of the cases does changing the spring constant by a factor of two lead to systematic discrepancy.

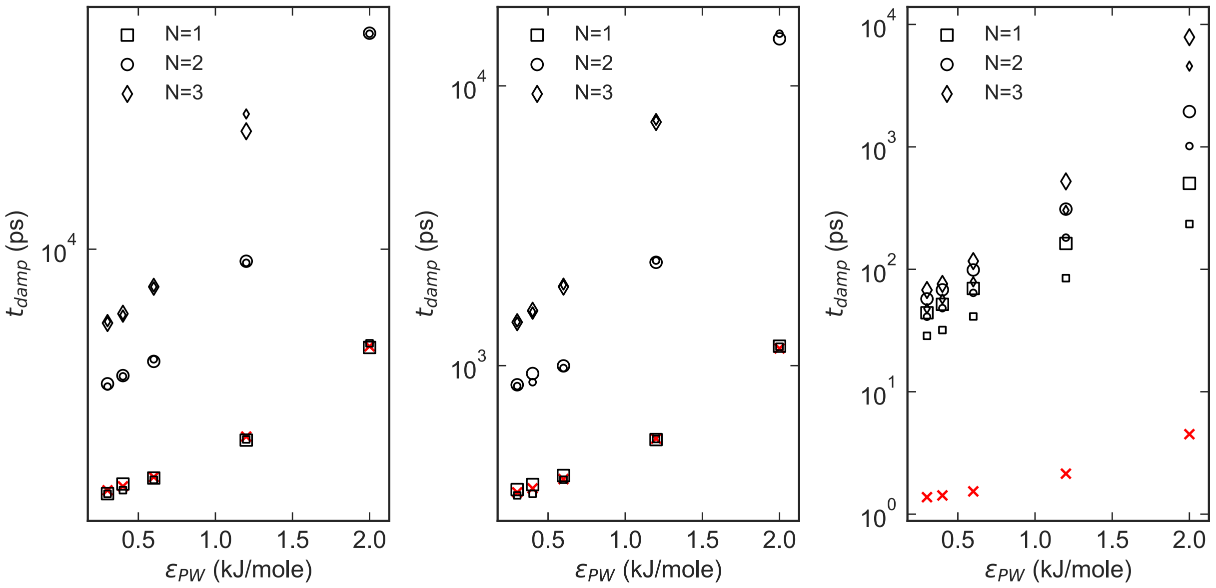

Figure C-2. Similar plotting scheme to Figure C-1, but in this case large markers are for bead mass of 45 amu, and small markers are for bead mass of 15 amu. For the simulations with tdamp = 0.064 ps and 0.25 ps, decreasing the mass by a factor of 3 does not yield a discrepancy, whereas a discrepancy appears for τdamp = 4 ps.

C.2 Adsorption rate coefficient from parameters of Chechkin et al.

Equation 15 from Chechkin et al. establishes the equilibrium relation between the adsorbed surface concentration and the desorbed bulk concentration.

$$c(x,y,z,t)\mid_{z=0} = \mu\Gamma(x,y,t) \tag{S-1}$$

where c is the bulk concentration, Γ is the surface concentration, and μ is the "coupling parameter" which governs the equilibrium ratio c/Γ. The kinetic equilibrium between surface and bulk allows us to write μ in terms of an adsorption rate coefficient and a desorption rate coefficient, due to

$$\frac{\partial\Gamma}{\partial t} = k_{\mathrm{ads}}c(x,y,z,t)\mid_{z=0} - k_{\mathrm{des}}\Gamma(x,y,t) \tag{S-2}$$

where k_{ads} is the adsorption rate coefficient and k_{des} is the desorption rate coefficient. By setting $\frac{\partial \Gamma}{\partial t} = 0$ for equilibrium, we can see that

$$\mu = \frac{k_{\text{des}}}{k_{\text{ads}}} = \frac{1}{k_{\text{ads}} t_{\text{des}}} \tag{S-3}$$

Skaug et al., in expressing Equation A8 from Chechkin et al. create an additional parameter $r^* = \frac{D}{Q_{\text{ads}} b}$ where Q_{ads} is the "adsorption rate constant" with dimensions of reciprocal time and b is the radius of gyration of the polymer. By comparing Skaug et al. Equation 1 with Checkin et al. Equation A8, we can see that

$$\frac{Q_{\text{ads}} b}{D} = \frac{1}{\mu t_{\text{des}} D} \tag{S-4}$$

Using Eqn. S-3 to substitute for μ in the above, we can rearrange to see that

$$k_{\text{ads}} = Q_{\text{ads}} b \tag{S-5}$$

From here, it is easy to see how Skaug et al. determine that the slope of the adsorption isotherm is independent of N. Skaug et al. show that $Q_{\text{ads}} \propto N^{-1.2}$ and $b \propto N^{0.6}$ for PEO in water (good solvent), and this implies that $k_{\text{ads}} \propto N^{-0.6}$. Skaug et al. also show that $t_{\text{des}} \propto N^{0.6}$, and since at equilibrium, $\frac{\Gamma}{c} = k_{\text{ads}} t_{\text{des}}$, we have at equilibrium $\frac{\Gamma}{c} = \mu^{-1} \propto N^0$.

C.3 Attempts to linearize strong-adsorbing polymer desorption times

Somewhat unsatisfied with Figure 5-6, we attempted to linearize the data to show the more universal behavior in the limit of strong adsorption. For this purpose, rather than plot NV_{MF} on the x-axis, we plotted $N\left(\frac{a}{l}\right)^{\frac{1}{\nu}} + \frac{NV_{MF}}{k_B T}$ on the x-axis, which is the right-hand side of Equation 4. The value *v* was 0.6 for the excluded-volume chain, and for the Kuhn length *a* we used 0.33 nm which was the bond length of the freely-jointed chain. The parameter *l* is the size of the zone to which the polymer is confined. We tried to determine *l* by adjusting it to make the data from Figure 5-6 fall onto the line with slope 1, indicating that Equation 4 was satisfied.

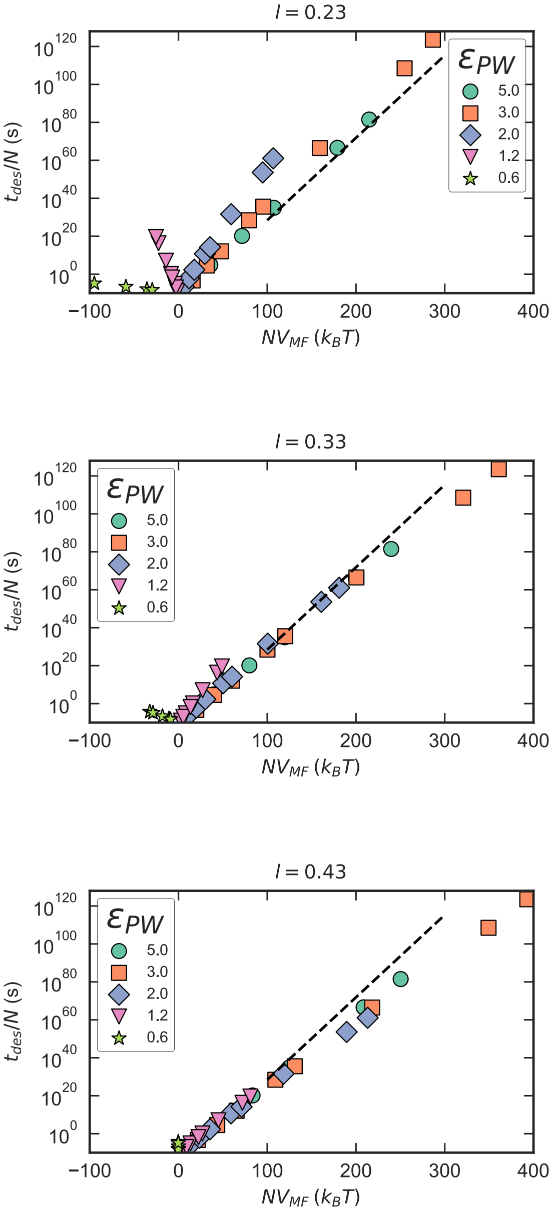

Figure C-3. Attempts to linearize the data from Figure 4-6 by plotting the right-hand side of Equation 4 on the x-axis. We used a = 0.33 nm, ν = 0.6, and the value of l used to generate each plot is printed above it.

For the strongest-adsorbing chains we studied with $\epsilon_{\mathrm{PW}} = 3.0$ and 5.0 kJ/mole appeared to match the expected slope for $\mathrm{l} = 0.23$ (see Figure C-3), although the data was best forced onto a universal-like line for somewhat larger values of l. This indicates that including the entropic repulsion term in free energy for prediction of desorption time scaling can provide desorption times that are measureable in a reasonable experimental time.

C.4 Comment on suitability of the Rosenbluth-like FFS variant

If advancing probabilities for microstates at a level *i* are distributed as, for example, $p_{i,j} \sim \mathrm{Beta}(\alpha_i, \beta_i)$, we find that the Rosenbluth-like FFS variant described by Allen et al.[19] can have severe problems. These problems occur when $p_{i,j}$ has large fluctuations from one microstate to another at each level. In the Rosenbluth-like variant, rather than assign a large number of attempts $M \approx 5000$ among all the observed microstates at a level at once, a smaller number of attempts $M \approx 100$ is assigned to just one microstate at each level, and one of the successful attempts is used to continue the path from $\boldsymbol{A}$ to $\boldsymbol{B}$. After $\boldsymbol{B}$ is reached, the process is started over from $\boldsymbol{A}$ and iterated many times to generate many paths from $\boldsymbol{A}$ to $\boldsymbol{B}$. If every microstate has similar advancing probability $p_{i,j} \approx p_i$, and the gates are chosen so that p_i is not very small, for example, $p_i \approx 0.1$, then typically $Mp_i \approx 10$ and it would be very rare to see zero successful attempts at a given level (about 5 in 100,000), meaning that many of the Rosenbluth paths are able to arrive at $\boldsymbol{B}$ from $\boldsymbol{A}$. Yet although p_i is the average of the $p_{i,j}$ at level i, an individual microstate *j* might have an advancing probability $p_{i,j} \ll p_i$. Given many levels, the Rosenbluth algorithm can routinely select a “bad” microstate j at some level i with $p_{i,j} \ll p_i$. This can make it very difficult for the Rosenbluth algorithm to arrive at $\boldsymbol{B}$ from $\boldsymbol{A}$, which it must do many times to obtain good sampling.